INVESTIGATION OF THE WORK HARDENING CHARACTERISTICS AND FRACTURE TOUGHNESS OF LOW ALLOY STEELS.

by P. NEUMANN B.Sc.

THESIS PRESENTED IN FULFILMENT OF THE REQUIREMENTS
FOR THE DEGREE OF DOCTOR OF PHILOSOPHY TO THE
DEPARTMENT OF METALLURGY IN THE UNIVERSITY OF
STRATHCLYDE, GLASGOW.

JANUARY 1976

SUMMARY

The mechanical and toughness properties of six structural steels have been investigated in detail over a range of temperatures between 20°C and -196°C.

The true stress - true strain characteristics have been analysed using several different approaches. Strain hardening exponent and transition strain valves were determined from Hollomon's equation

$$\sigma_T = K \ \varepsilon_T^{\ n}$$

using the simple log σ_T - log ε_T plot and the more complex Crussard analysis. The crussard analysis was found to be unreliable in prediction of both transition strain and strain hardening exponent. As deformation temperature was reduced below ambient, the strain hardening exponent values tended to a maximum at some critical temperature below which the strain hardening exponent values decreased. Transition strain tended to increase with decreasing deformation temperature, until at some critical temperature two stage hardening was replaced by single stage hardening. The variation of true work hardening rate $\left(d\,\sigma_T / d\,\varepsilon_T \right)$ with strain and temperature was determined. At high strains, the true work hardening rate increased linearly with decreasing deformation temperature whilst at low strains the same behaviour occurred until a critical deformation temperature was attained, when the true work hardening rate decreased. This behaviour might be explained by a change in deformation mechanism at low temperature.

Critical crack opening displacement (C.O.D.) values were determined for all the alloys over the temperature range 20°C to -196°C. The critical event was defined as the onset of slow crack growth, or fast fracture, whichever occurred first. Onset of slow crack growth was detected by a potential drop technique, which was found to give good reproducibility in critical C.O.D. values. The normal transition behaviour was observed in these tests and the effect of increasing grain size on reducing toughness was investigated.

No direct correlation between work hardening behaviour and toughness could be deduced and the relationship previously derived by Hahn and Rosenfield, and by Thomason, relating material mechanical properties t plane strain fracture toughness were found to be unacceptable in the light of the data obtained.

It has been assumed in the past that the plastic instability strain, as measured in a tensile test, is the relevant strain when considering slow crack growth as the failure mechanism. It is proposed in the present study that a more realistic approach is to consider the critical strain as being that strain at which void linkage occurs.

CONTENTS

CHAPTER 1

INTRODUCTION

Fracture mechanics has evolved over the past twenty years to become one of the most important tools of modern technology. Through its application to brittle materials, realistic assessments of the critical flaw size to cause brittle fracture, under a given stress regime, can be made.

Probably the area of widest interest in the toughness assessment field, however, is that involving semi-brittle and ductile materials. By far the most widely used class of alloys today are steels, and a lot of attention has been focussed on the measurement of their defect susceptibility. No great problems arose in the application of linear elastic fracture mechanics to inherently brittle steels, exhibiting minimal plastic deformation in cracked sections prior to fracture, but the same convenient analysis was found to be inapplicable to the semi-brittle and ductile classes of steels, where unacceptable levels of plasticity were encountered.

In recent years, however, General Yielding Fracture Mechanics has been developed, which permits toughness assessments on the semi-brittle and ductile classes of materials to be made in terms of the crack opening displacement (C.O.D.) at failure. The C.O.D. analysis however takes no account of the work hardening characteristics of materials.

Much effort has been made in the metallurgical field, to define parameters which describe the work hardening characteristics of metals and alloys. The most popular approach is to determine a mathematical relationship descriptive of the true stress - true strain tensile deformation behaviour of the material in question, and to use a parameter derived from this mathematical description as a definitive work hardening parameter. The most popular parameter chosen to describe true stress - true strain behaviour has been the strain hardening exponent.

There has been much debate over the interpretation of strain hardening exponents, and indeed over the methods used to obtain the values, while various physical processes have been proposed to describe the observed variation in the strain hardening exponent with test conditions.

Recently attempts have been made to assess material toughness with the aid of these mathematical descriptions of tensile deformation behaviour. Success has been claimed by several workers in relating the plane strain fracture toughness (K_{IC}) to strain hardening exponent values derived from tensile tests.

The present investigation was undertaken to study the variation in toughness and work hardening characteristics, in materials where the general yielding fracture mechanics technique was required to define a toughness parameter, since the existence of a unifying relationship between toughness and simple tensile test data in this area would greatly simplify the measurement of critical toughness values under given conditions.

Six alloys were studied in detail, and their toughness and work hardening characteristics were studied over a range of temperatures between 20°C and - 196°C

CHAPTER 2

LITERATURE REVIEW

2.1. Tensile Stress-Strain Behaviour of Metals

The behaviour of metals and alloys under tension has long been of interest to metallurgists. A primary object in analysing this behaviour is to produce relationships which will adequately describe behavioural patterns, and also give some insight into the physical processes occurring during tensile deformation. Unfortunately, although several mathematical equations have been devised describing the stress strain behaviour of metals, none too clear a physical significance can be attached to the parameters arising from these analyses.

Stress strain behaviour of metals is always analysed on the basis of true stress, true strain data, and the simplest description of the stress-strain curve for ferritic steels is that due to Hollomon He analysed data from various steels, and found that an adequate description of the behaviour in most cases was given by an equation of the form

$$\sigma_T = K \varepsilon_T^n \qquad (1)$$

where:

σ_T = True Stress

ε_T = True Plastic Strain

n = Strain hardening exponent

K = Strength coefficient

A similar relationship to this was proposed by Ludwik [2]

$$\sigma_T = \sigma_o + k\varepsilon_T^{n'} \qquad (2)$$

where: σ_o = Yield stress

Obviously in the case were $\sigma_o = 0$, Ludwik's equation and Hollomon's equation are identical. Neither equation is universally applicable, but most tensile data will fit either one or the other curve.

Of these two expressions, that due to Ludwik does seem more logical, in that it includes a term to take into account the yield stress whereas Hollomon's equation implies that true stress is zero when the true plastic strain equals zero. In spite of this fact, Hollomon's relationship has been applied frequently to many metals and alloys.

Morrison[3] carried out the first comprehensive investigation of the Hollomon equation, using steels of varying carbon content and grain size. From the data obtained in these tests, Morrison found that the equation adequately described the true stress - true strain behaviour observed in tensile tests performed at constant temperature and strain rate. He determined log σ_T - log ε_T plots for all the tests performed, and two distinct types of behaviour were noted:

(a) Single n behaviour, when the log σ_T -log ε_T plot yields one straight line of slope n_A

(b) Double n behaviour, when the log σ_T -log ε_T can be approximated to two straight lines of slope n_B and n_C. The strain at which the transition from n_B to n_C occurs is denoted by ε_I.

The transition strain ε_i has been shown to be affected by both temperature and strain rate [4, 5]. At constant temperature, an increase in strain rate increases the transition strain ε_i, whilst at constant strain rate an increase in temperature decreases the transition strain.

Several investigations [4, 5] have been carried out into the effect of temperature on strain hardening exponent n in Hollomon's relationship. Bergström and Aronsson[4] analysed data from a 0.038%C 0.33% Mn steel tested at various temperatures between 25°C and 500°C. In this temperature range they found that n was decreasing with increasing temperature. Morrison[5] carried out tensile tests on a 0.09%C 0.33% Mn steel at temperatures in the range 26°C to -70°C, and found that n decreased with decreasing temperature. From these results n would appear to have a maximum value at about ambient temperature.

Monteiro and Reed-Hill[6] suggest the use of the technique introduced by Crussard[7] for analysis of true stress-true strain data. Considering both Ludwik's and Hollomon's equations (equations (1) and (2)) and differentiating them with respect to strain, the same resultant expression is obtained.

$$\frac{d\sigma_T}{d\varepsilon_T} = nK\varepsilon_T^{\,n-1} \qquad (3)$$

Plotting $d\sigma_T/d\varepsilon_T$ v ε_T on a log-log scale should then yield a straight line of slope (n-1). In cases where uncertainty as to whether Hollomon's or Ludwik's expression best describes the data, then the Crussard analys would seem to be the most suitable approach to adopt. Monteiro and Reed-Hill further suggest, that by use of this method, better estimates of n are obtained, together with more accurate assessments of the transition strain, particularly in cases where materials exhibit a strong dependance of flow stress on temperature.

Attempts have also been made to correlate work hardening behaviour with the structural changes occurring during deformation. To this end, electron microscope studies on deformed tensile specimens have been carried out by various workers[3, 5, 8, 9]. Initial investigation[3] indicated that single 'n' and double 'n' behaviour could be related to different dislocation sub-structures. The dislocation cell structure in material exhibiting double 'n' behaviour was far more pronounced and developed than in a single 'n' material at a true strain of 5%, whilst at 15% strain many of the cells in the double 'n' materials are elongated in shape compared with very few in single 'n' materials.

Christ and Smith[9] have shown that for iron at room temperature, deformation up to about 9% strain is characterised by a rapid increase in dislocation density, with the formation of a clearly defined cellular structure composed of dislocation tangles. This strain of 9% corresponds approximately to the transition strain observed for various iron alloys[3, 5] tested at room temperature and Li[10] has suggested that entire dislocation tangles may move at larger strains.

Further evidence of a correlation between transition strain and dislocation cell structure has been presented by Morrison[5]. He plotted values of transition strain obtained in his study, against temperature and obtained a straight line relationship. The slope of this line is similar to that found by Keh and Weissmann[8] when they determined the strain at which cell formation occurred in iron at various temperatures. This tentative relationship between transition strain and cell formation strain would seem to provide evidence for the suggestion that the formation of cells leads to a change in the work hardening mechanism.

The occurrence of double 'n' behaviour may be related initially to the movement of individual dislocations to form cellular structures, and subsequently to the combined movement of dislocations and dislocation tangles. It has been suggested[9] that single 'n' behaviour is due to the primary stage being disguised within a fairly large region of Lüders strain in materials exhibiting discontinuous yielding.

2.2. Fracture Mechanics Development

Great impetus has been given to the development of fracture susceptibility assessment over the last twenty years, mainly because of the requirements of military and space agencies for ever higher strength materials[11]. High strength metallic materials however display an alarming tendency to fracture in a catastrophic brittle fashion, when subjected to stresses well within their rated yield stresses. The basic reason for failure in this fashion is of course the presence of pre-existing or induced crack like defects in the material, which act as stress concentrators.

2.2.1. Theoretical strength of materials

Before considering the effects on a material of the presence of a crack, it would be instructive to examine the theoretical cleavage stress, and compare its magnitude with that found in practice.

By considering the stress required to separate adjacent rows of atoms in a crystal, and assuming that elastic conditions prevail one obtains a simple expression for the theoretical cleavage stress,

$$\sigma_c = \sqrt{\frac{E\gamma_s}{a_o}} \qquad (4)$$

where:

γ_s = true surface energy

a_o = equilibrium atom spacing

E = Youngs Modulus

Typical values of E, γ_s and a_o, give a theoretical cleavage stress of ~ E/7, and using more precise force separation laws, values of σ_c ranging from E/4 to E/3 have been obtained. For most metals. the theoretical cleavage stress is greater by a factor of 10^2, or higher, than those found in practice.

One of the main contributory factors to this discrepancy is the presence in most materials of cracks and notches of varying sizes, and these discontinuities act as stress concentrators, which raise the applied stress to the same order as the theoretical cleavage stress in the vicinity of the crack tip. The theoretical cleavage stress will not however be realised if some other fracture process, which is accompanied by plastic deformation operates at a lower level of applied stress.

2.2.2. Advancement of sharp crack fracture mechanics

After Inglis[12], in 1913, had analysed the stress concentration in the vicinity of an elliptical hole, in an infinite place subjected to tension, the first major contribution in the fracture assessment field was made by Griffith[13], in 1920, He argued that when a material is subjected to stress, the fracture process will not occur, unless the energy required to form the new crack surfaces is less than the elastic strain energy released by crack propagation.

Griffiths equation for the critical cleavage stress in a material containing a crack of length 2C, under purely elastic conditions, is

$$\sigma_{Cr}^{G} = \sqrt{\frac{2E\gamma}{\pi C}} \qquad (5)$$

Where: γ = surface energy/unit area of crack face

C = half crack length

Comparing equations (4) and (5), one sees that Griffith's approach to fracture, affords an equation which predicts the correct functional relationship between failure stress and crack length i.e. $\sigma_{Cr} \propto C^{-\frac{1}{2}}$.

Although Griffith's success indicated the validity of an energy approach, his analysis was difficult to apply, because of the problems involved in the measurement of the surface energy parameter γ_s. Also the Griffith's approach can only be considered valid if fracture is accompanied by no plastic deformation.

The most significant contribution so far made to fracture assessment has been that of Irwin[14]. In the 1950's Irwin used Westergaards[15] crack stress field analysis to calculate equations representing the distribution of stress in the vicinity of an elastically loaded sharp crack. The results obtained by Irwin are summarised in Figure A and equations 6a, 6b and 6c below.

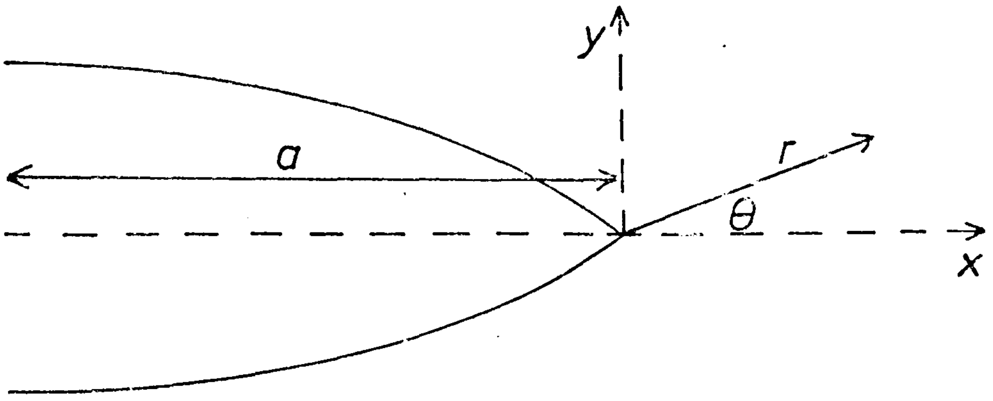

FIGURE A

where: x and y define the orthogonal axes at the crack tip;

θ and r are the polar co-ordinates of a point in the plane of the crack.

$$\sigma_x = \frac{K}{(2\pi r)^{\frac{1}{2}}} \cos\frac{\theta}{2} \left(1 - \mathrm{Sin}\,\theta \sin\frac{3\theta}{2}\right) \qquad (6a)$$

$$\sigma_y = \frac{K}{(2\pi r)^{\frac{1}{2}}} \cos\frac{\theta}{2} \left(1 + \sin\theta \sin\frac{3\theta}{2}\right) \qquad (6b)$$

$$\sigma_{xy} = \frac{K}{(2\pi r)^{\frac{1}{2}}} \cos\frac{\theta}{2} \sin\frac{\theta}{2} \cos\frac{3\theta}{2} \qquad (6c)$$

The stress state in the region of the crack tip is then characterised by the value of K, which is termed the stress intensity factor. As the load or stress on a cracked component increases, then K increases accordingly until a limiting value of K is attained in the region of the crack tip. If, up until this point, yielding has been suppressed, and a state of plane strain exists in the cracked body, then discontinuous catastrophic crack propagation will occur.

Under conditions of plane strain, which implies a state of traxiality of stress at the crack tip, the critical value of the parameter K is called the plane strain stress intensity, and is commonly represented as K_{IC}.

K_{IC} can be regarded as a material property in the same way that yield stress is, and the value of K_{IC} is sometimes referred to as the toughness of the material. Analytical solutions for K exist for many crack containing geometries[16], in terms of stress, crack length and various geometrical parameters. The simplest case to consider however is that of a transverse elliptical crack in an infinite plate subjected to tension, where stress analysis yields the following relationship:

$$K = (\pi a)^{\frac{1}{2}} \sigma_A \tag{7}$$

where:

$2a$ = crack length

σ_A = applied stress

If the critical value of K for the material concerned is known, then from equation (7) one can see that crack length - stress relationships become rigidly defined for the crack geometry under consideration.

The critical stress intensity factor K_C varies with both thickness of material under consideration, and with temperature. As the thickness of the component under consideration increases, then the value of K at which fracture or crack propagation occurs, descreases until the limiting value K_{IC} is obtained. This thickness effect illustrates the effect of the transition from plane stress conditions in relatively thin sections to plane strain conditions in thicker sections.

K_{IC} varies with temperature[17] as one might expect, its value in general decreasing with decreasing testing temperature.

Both A.S.T.M.[18] and B.S.I.[19] have produced draft proposals for plane strain fracture toughness testing, and many authoratative reviews of fracture toughness principles have been published in the last ten years[20, 21].

2.2.3, General yielding fracture mechanics

A major problem still existed in the field of fracture toughness analysis. Linear Elastic Fracture Mechanics (LEFM), as the branch of fracture mechanics devised by Griffith[13] and Irwin[14] is known applies solely to the elastic regime. Small degrees of plasticity can be tolerated, and crack tip plasticity correction factors have been devised, but when general yielding occurs, L.E.F.M. becomes inapplicable.

This problem was recognised almost simultaneously by Cottrell[22] and Wells[23], who independently suggested that crack opening displacement (C.O.D.) might be used as a parameter characterising the toughness of materials exhibiting large amounts of plastic deformation prior to fracture.

The results of those suggestions was the emergence of General Yielding Fracture Mechanics (G.Y.F.M.) which deals with the analysis of crack tip plastic zones, and their associated displacements.

C.O.D. is the characterising parameter of G.Y.F.M., and describes the amount by which the faces of a crack separate, when subjected to an external force, before any propagation of the crack occurs. Several studies[24,25] have verified that this process of separation without propagation takes place.

An early attempt to analyse the crack tip plastic zone and its associated displacements was due to Wells[26]. He employed expressions derived for the purely elastic case by Irwin[14], to describe the stress acting transverse to the crack plane, and also the displacement which the applied stress produced within the slit.

Wells model[26] was based on an infinite plate containing a transverse sharp slit of length 2a, subjected to a uniform tensile stress . Assuming non-work hardening behaviour, and simplifying the expression of Irwin slightly, Wells applied plasticity corrections to these expressions and arrived at the following equation relating C.O.D(δ) and L.E.F.M. parameters.

$$\frac{K^2}{E} = \frac{\pi}{4}\,\sigma_y\,\delta \qquad (8)$$

Where: σ_y is the Yield Stress

An alternative approach was adopted for calculation of plastic zone sizes and displacement by Bilby, Cottrell and Swinden[27]. The yield zone and crack are presented as arrays of dislocations as shown in Figure B.

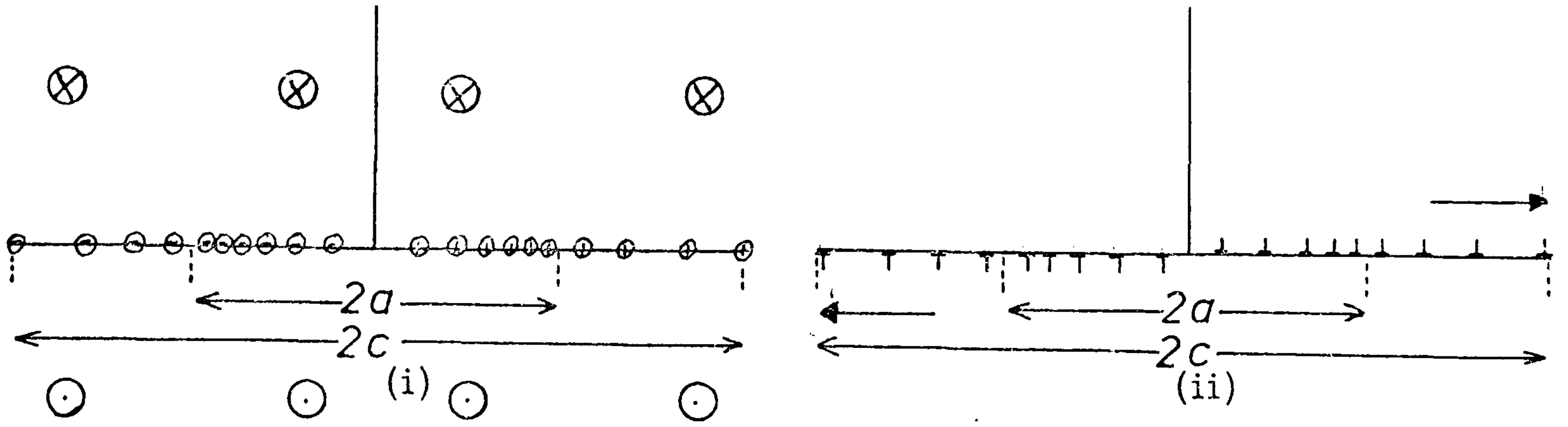

FIGURE B

Mode II shear may be represented by a distribution of collinear edge dislocation as shown in Figure B(ii) whilst Mode III shear may be represented by a distribution of collinear screw dislocation as shown in Figure B(i).

A displacement gradient exists from the crack tip, where the displacement is a maximum to the edge of the plastic zone, where the displacement falls to zero. This gradient is accounted for by setting up an inverse pile up of dislocations closely spaced near the crack tip and widely spaced at the edge of the plastic zone.

In this treatment the dislocations are not treated as discrete, but described by the theory of continuous distribution of dislocations. The mathematical analysis when applied to the situation depicted in Figure B(i) for mode III deformation, yields the following results:

$$\frac{a}{C} = \cos \frac{\pi \tau}{2\sigma_{EF}} \qquad \delta = \frac{8\sigma C}{\pi G} \log_e \sec \frac{\pi \tau}{2\sigma_{EF}} \tag{8}$$

where: c = half crack length plus plastic zone at crack tip.

τ = external applied shear stress.

σ = inherent resistance to movement of dislocations in the region $C > x > a$, $-a > x > -C$

G = Shear modulus.

An alternative approach to crack tip analysis in the presence of widespread plasticity is that adopted by Burdekin and Stone[28]. They employed a model which had earlier been developed by Dugdale[29], to describe the yielding of steel sheets containing slits when loaded in tension.

Dugdale's model[29] is based on an infinite sheet subjected to a uniform tensile stress T, applied at its edges in a direction perpendicular to a slit of total length 2a, as shown in Figure C.

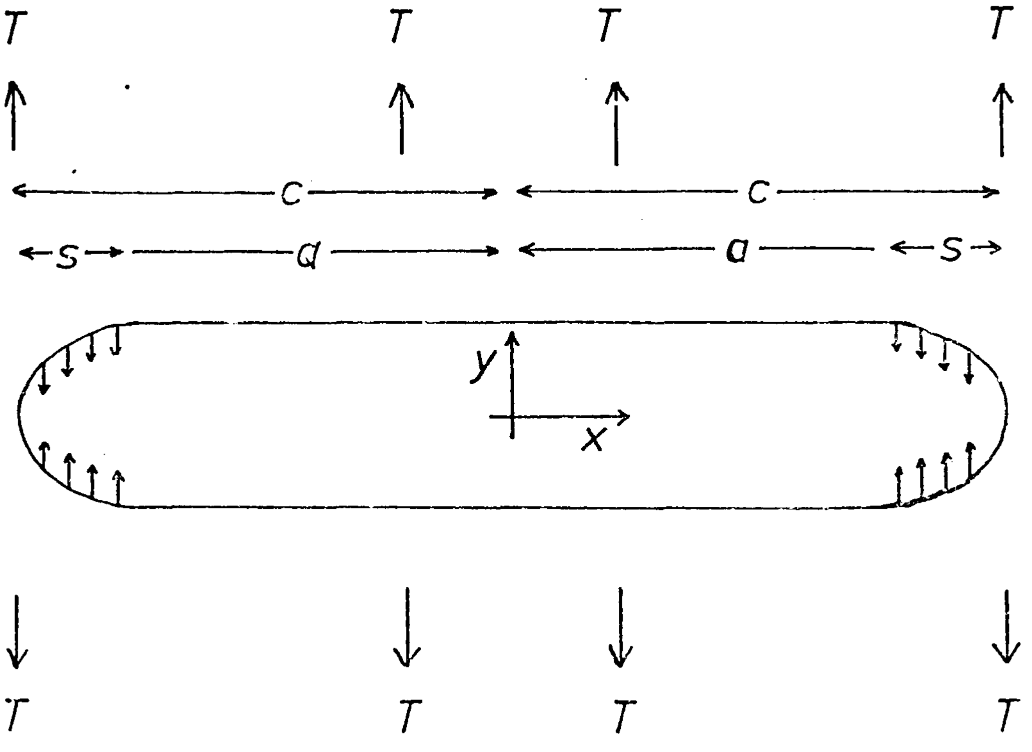

FIGURE C

Under the applied stress T, plastic zones are developed at the crack tip, extending a distance S from the crack tip. This situation is represented for the purpose of analysis by a crack of length $2C = 2a + 2S$, surrounded by an entirely elastic stress field. This hypothetical crack is considered to be subjected not only to the externally applied stress T, but also to an internal tensile stress Y, distributed over that part of the hypothetical crack described by $C > x > a$, $-a > x > -C$.

Burdekin and Stone[28] equated this internal tensile stress within the plastic zone, to the material's uniaxial yield strength. The analysis of the crack tip plasticity situation has now been made relatively simple, since only elastic stresses and displacements need be considered.

The C.O.D. at the tip of the real crack, using this model is represented by the displacement at $\pm a$, within the elasticially stressed crack of length 2c, and is given by:

$$\delta = \frac{8\sigma_y a}{\pi E} \log_e \sec \frac{\pi\sigma}{2\sigma_y} \qquad (9)$$

This expression is in agreement with that derived by Bilby, Cottrell and Swiden[27] (Equation (8)). Whilst Burdekin and Stone's analysis cannot be considered to provide a rigorously plastic solution, it has been demonstrated that for real materials, Equation (9) can give reasonable estimates of failure stresses[30, 31].

If Equation (9) is expanded in series form, the following result is obtained:

$$\delta = \frac{8\sigma_y a}{\pi E} \Big[\frac{1}{2} \left(\frac{\pi\sigma}{2\sigma_y}\right)^2 + \frac{1}{12} \left(\frac{\pi\sigma}{2\sigma_y}\right)^4 + \frac{1}{45} \left(\frac{\pi\sigma}{2\sigma_y}\right)^6 + \cdots \qquad (10)$$

Considering only the first term in the expansion as being significant, which is valid for $\sigma/\sigma y \ll 1$, then one arrives at the same result as that proposed by Wells.

$$\frac{K^2}{E} = \sigma_y \delta \qquad (11)$$

Taking into account the first two terms in the expansion. crack C.O.D. can be described by the following expression

$$\delta = \frac{\pi\sigma^2 a}{E\sigma y}\left[1 + \frac{\pi^2}{24}\left(\frac{\sigma}{\sigma y}\right)^2\right] \qquad (12)$$

The L.E.F.M. approach gives the following expression when the first stage plastic zone size correction factor is applied:

$$\frac{K^2}{E\sigma_y} = \frac{\pi\sigma^2 a}{E\,\sigma_y}\left[1 + \frac{1}{2}\left(\frac{\sigma}{\sigma_y}\right)^2\right] \qquad (13)$$

Equations (12) and (13) are very similar, indicating once again the relationship of Equation (11).

As has been discussed, crack opening displacement has been proposed as a fracture criterion on a theoretical basis, but it is of course, necessary to back up this theoretical prediction with practical example.

The most impressive method of verifying crack opening displacement as a fracture criterion would be to test a standard fracture mechanics specimen, determining some critical value of crack opening displacement, and comparing the critical stress computed from this value with that required to cause failure in a precracked service structure. Several studies of this nature have been cited in the literature [25, 30, 31].

Parry and Mills[31] compared the relationship between hoop stress and crack opening displacement in zirconium alloy pressure tubes from the theoretical and experimental standpoint.

As can be seen in Figure D, the best description of the experimental results is given by line 2, which is Burdekin and Stone's relationship modified by the Folias[32] correction factor, which has been shown to give a very good estimate of the increase in stress intensity when one moves from a flat plate to a cylindrical situation.

Fearnehough and Watkins[25] also carried out a test programme to assess the viability of the C.O.D. approach to assessment of zirconium alloy tube failure. Pressure tests were carried out on these tubes, and C.O.D measurements were obtained from a calibration curve of hoop stress v C.O.D. which had previously been established. Failure stresses and the corresponding crack opening displacements were noted. Bend tests were carried out on identical material, and C.O.D. measurements were obtained. Failure stresses were estimated from these bend C.O.D. values, and good agreement was obtained between measured and calculated C.O.D.

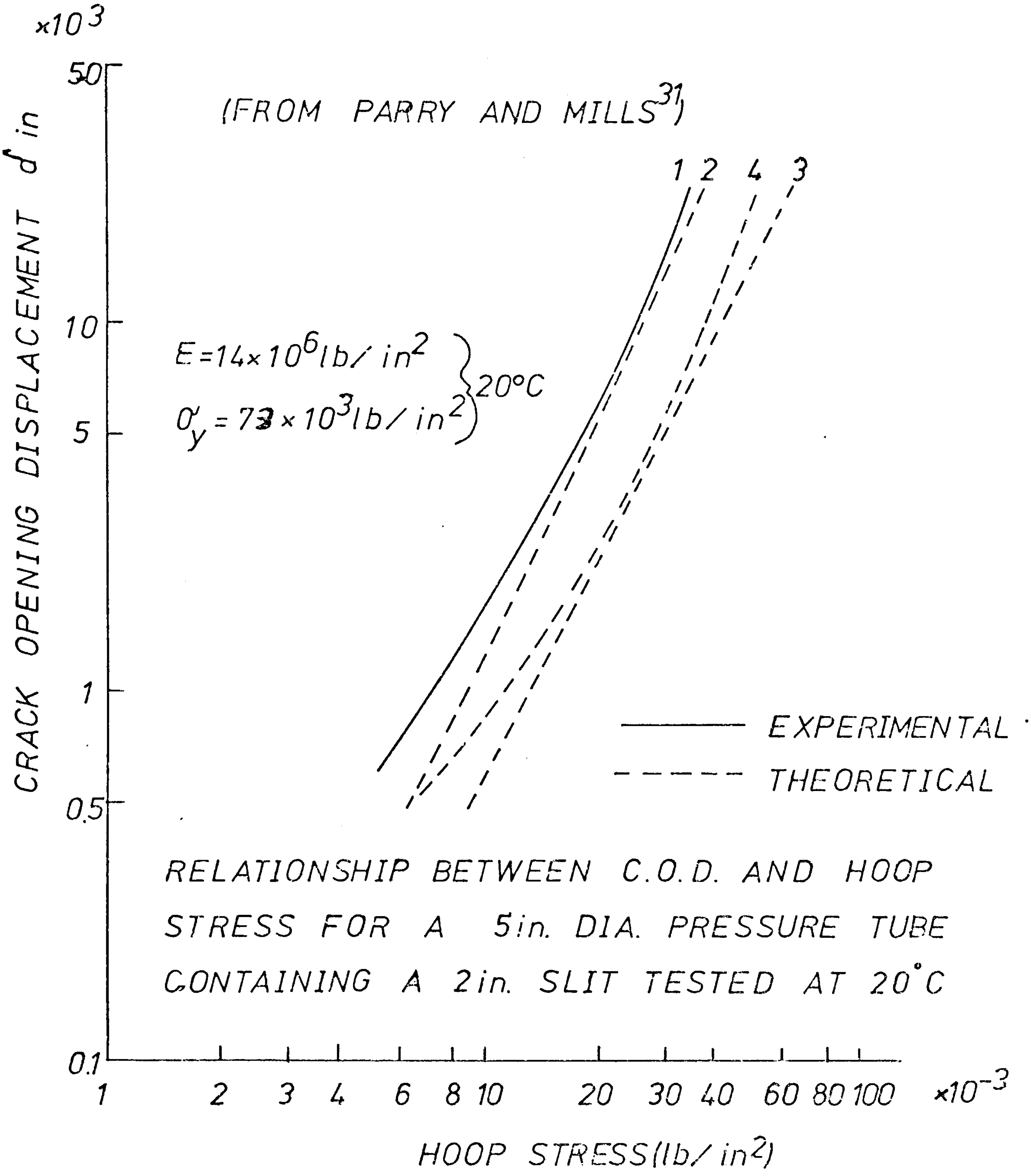

RELATIONSHIP BETWEEN C.O.D. AND HOOP STRESS FOR A 5in. DIA. PRESSURE TUBE CONTAINING A 2in. SLIT TESTED AT 20°C

(2) $$\delta = \frac{8\sigma_y a}{\pi E}\left(\ln\sec\frac{\pi\sigma_H}{2\sigma_y}\right)\left(1 + 1.6\frac{a^2}{rt}\right)$$

(3) $$\delta = \frac{\pi\sigma_H^2 a^2}{2E\sigma_y}$$

(4) $$\delta = \frac{8\sigma_y a}{\pi E}\ln\sec\frac{\pi\sigma_H}{2\sigma_y} \simeq \frac{\pi\sigma_H^2 a}{E\sigma_y}$$

FIGURE D

2.2.4. The J-contour integral

The most recent attempt to characterise toughness, in situations where L.E.F.M. analyses are not valid, is the concept of the J-integral proposed by Rice[33].

Essentially J may be defined as the rate of change of potential energy with crack length.

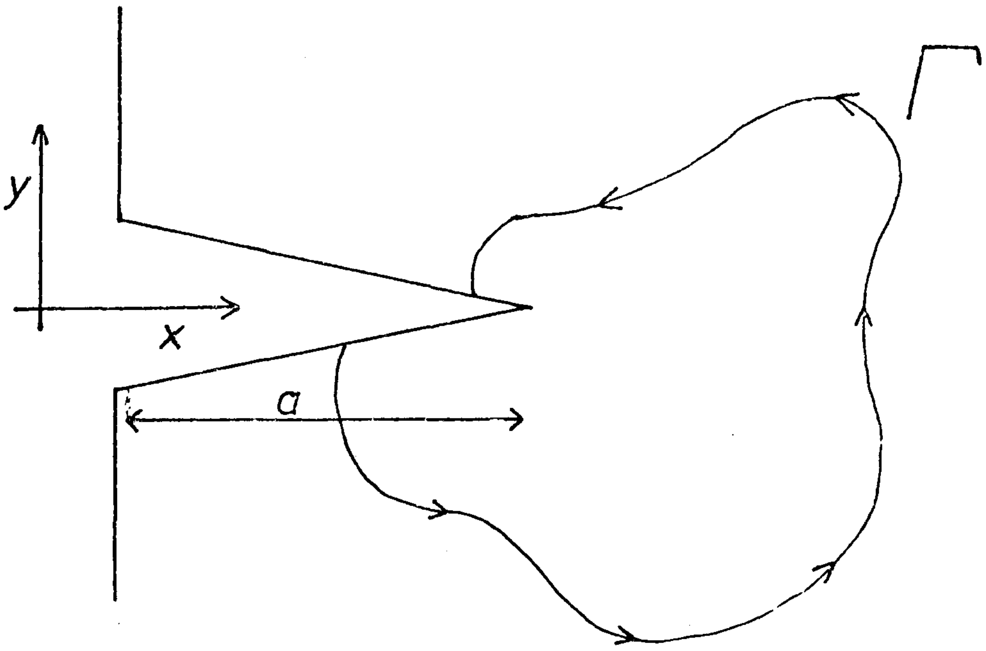

FIGURE E

Considering Figure E, it is possible to define a line integral, J, on any curve Γ surrounding the crack tip, starting from the lower surface, and ending on the upper surface of the notch, such that J is given by:

$$J = \int_{\Gamma} \left[W dy - T \frac{\partial u}{\partial x} ds \right] \qquad (14)$$

where the curve is traversed in the anti-clockwise direction. W is the strain energy density ($W = \int_0 \sigma d\varepsilon$), s is the arc length, U is the displacement, and T is the traction vector normal to the curve Γ. A detailed description of its derivation may be found elsewhere[34].

It may be shown that for two different curves Γ_1 and Γ_2 around the same crack, the difference in computed J values is zero, and the conclusion is that J integral is path independent, and is equivalent to the change in potential energy when the crack front moves by an amount da.

The simplest experimental method of determining J arises from its definition as the rate of change of potential energy with crack length.

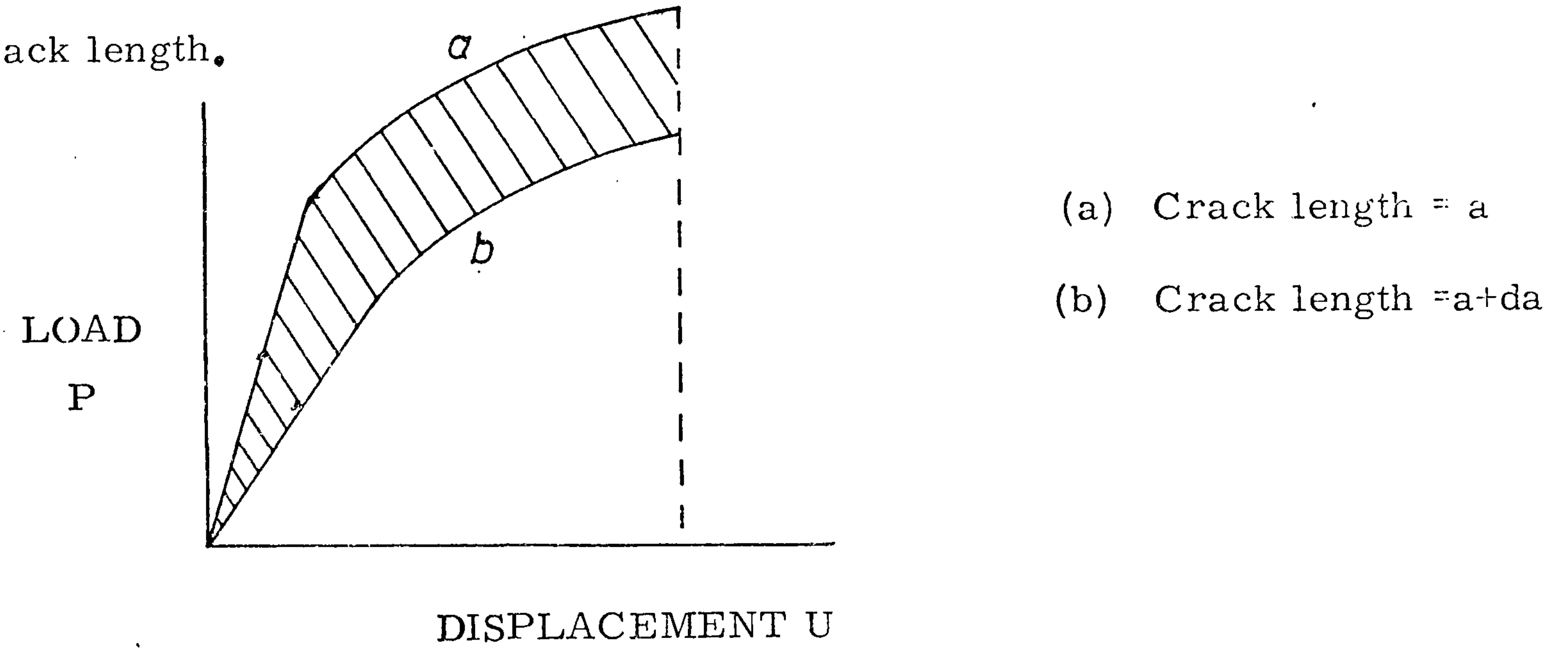

FIGURE F

Figure F shows 2 typical loading curves for specimens containing cracks of length a, and a+da. The shaded area in the above figure represents an energy change JBda.

From a family of curves, for various crack lengths, similar to Figure F experimental values of J are readily obtainable. At a given displacement, the areas under the curves of P versus U, for the various crack lengths, are measured, these areas being equivalent to the potential energy. If this procedure is carried out at various displacement values, then a curve of potential energy versus crack length may be drawn for various displacements. J is simply obtained by measuring the tangents to these curves at a given crack length a_J and hence a curve may be obtained showing the variation of J with displacement.

There is evidence to suggest[35] that a constant J_{IC} criterion, characterises fracture in situations where different stress states are operative in the crack tip region in different test pieces of the same material.

The J contour integral is a relatively new concept in the fracture toughness field, and much work has still to be done to determine the suitability of its application as a quality control parameter, and the effect of strain rate and temperature on the critical values of J.

2.3. Relationships between Mechanical Properties of Metals and their Fracture Toughness

The fracture mechanics philosophy discussed earlier, whereby certain parameters, K and δ, could be used to compare the notch sensitivity or fracture toughness of materials on a quantitative basis, took no account of the manner in which metals work harden after yielding has occurred.

Thus general yielding fracture mechanics (G.Y.F.M.), assigns a stress equivalent to the yield stress, in the plastic zone ahead of the crack. This assumes perfectly plastic behaviour, with no increase in stress occurring with increasing strain i.e. zero work hardening. All common structural steels exhibit a marked degree of work hardening behaviour, and this can be represented, at least qualitatively, by the strain hardening exponent term arising from

Hollomon's equation (Equation 1).

Hahn and Rosenfield[36] deal with both plane strain and plane stress situations. Under conditions of plane strain, one has triaxiality of stress conditions, and the stress can rise to values much greater than the yield stress, due to the elastic constraint of the surrounding material.

Irwin[38] has postulated that the ductility transition, and the fracture appearance transition, which occur at the same temperature arise as a result of a transition from plane stress conditions, existing above the transition temperature, to plane strain conditions existing below the transition temperature. Irwin also suggested that the transition occurred when the plastic zone size in the ductile material became equal to the plate thickness.

Hahn and Rosenfield[36] however, on the basis of their experimental measurements, choose the upper bound for plane strain conditions as being a plastic zone size equal to half the plate thickness and the lower bound for plane stress as being a plastic zone equal to twice the plate thickness.

Hahn and Rosenfield introduced the idea of critical fracture strain into their theorem. They used a concept developed by McClintock[39] for calculating the true strain required to expand a series of cylindrical voids to the point where the voids link up.

Assuming that

$$\overline{\varepsilon}^*_{\text{ahead of crack}} \propto \overline{\varepsilon}^*_{\text{tensile test}}$$

where

$\overline{\varepsilon}^*$ is the critical fracture strain

Hahn and Rosenfield relate the critical true strain in plane stress and plane strain zones to the strain to fracture in a tensile test thus,

$$\overline{\varepsilon}^*_{\text{plane strain zone}} = \frac{1}{3}\,\overline{\varepsilon}^*_{\text{tensile test}}$$

$$\overline{\varepsilon}^*_{\text{plane stress zone}} \doteq \frac{1}{2}\,\overline{\varepsilon}^*_{\text{tensile test}}$$

Perhaps the most crucial assumption made in this analysis, is that whereby the strain hardening exponent is introduced into the analysis. The strain in both plane strain and plane stress regions is described in terms of displacements and plastic zone sizes. Hahn and Rosenfield propose a relationship between strain hardening exponent and plastic zone size which they corroborate with experimental proof. The proposed relationship is l (in inches) $= n^2$, where l is the plastic zone size and n is the strain hardening exponent.

Relationships can now be obtained relating plane strain fracture toughness, and plane stress fracture toughness parameters to the strain hardening exponent on the basis of these assumptions, giving:

$$K_{IC} = \sqrt{\frac{2}{3} E \sigma_y \overline{\varepsilon}^* n^2} \qquad (15)$$

$$K_C \doteqdot \sqrt{\frac{1}{4} E \sigma_y \overline{\varepsilon}^* n^2} \qquad (16)$$

Equation (15) relates to situations where fracture occurs under plane strain conditions, whilst equation (16) refers to plane stress conditions.

This relationship was used to calculate K_{IC} values from tensile date obtained in other testing programmes on a steel tempered to various strength levels. The results obtained from calculation showed good agreement with K_{IC} values obtained from toughness tests.

Krafft [37] adopted a rather different approach in his attempt to set up a correlation between plane strain toughness and strain hardening characteristics.

The last true strain value which can be determined accurately from a tensile test is the strain to plastic instability, and because of this Krafft adopts this strain as his strain controlling parameter. This is of course a most convenient assumption to make, in that the plastic instability strain is theoretically equivalent to the strain hardening exponent in materials where deformation behaviour can be described by a Hollomon type relationship (Equation 1).

A further simplification of the true situation is made by assuming that the strain distribution within the plastic zone at a crack tip is given by the elastic solution, and Krafft considers this solution to be applicable right up to the region in which fracture is occurring at the crack tip:

$$\varepsilon_y = \frac{K}{E} \quad \frac{1}{\sqrt{2\pi r}} \tag{17}$$

Having chosen the strain to plastic instability, ε_I as the controlling strain parameter, it is possible now to determine a distance r_I from the crack tip, where the strain for plastic instability is attained ($\varepsilon_I = n$). Thus at the point of incipient fracture, when $K = K_{IC}$, the strain at this distance r_I is given by

$$\varepsilon_I = \frac{K_{IC}}{E} \quad \frac{1}{\sqrt{2\pi r_I}} \tag{18}$$

This strain ε_I should correlate with the strain hardening exponent n , measured from true stress-true strain curves, if the strain hardening exponent is measured under the same conditions of temperature and strain rate as apply at the distance r_I from the crack tip.

From this information, and the relevant true stress-true strain and toughness data, estimates can be made of the "process zone" size r_I.

The correlation which Krafft arrives at between K_{IC} and strain hardening exponent n , can be written as

$$K_{IC} = E\sqrt{2\pi r_I} \quad n \tag{19}$$

By different routes therefore, Krafft[37], and Hahn and Rosenfield[36] find that $K_{IC} \propto n$.

Another attempt to relate plane strain fracture toughness, K_{IC}, and strain hardening exponent in metals was that due to Thomason[40]. This approach was based on a previous model[41] which described ductile fracture in terms of the coalescence of uniformly distributed cavities, subjected to transverse stresses, and related the post instability strain to fracture (ε_{I-F}), and the volume fraction of second phase void nucleating particles at different transverse stress levels.

The model describing the plane strain fracture toughness relationship with strain hardening exponent employs several simplifications and assumptions.

The form of the stress-strain curve for real metals is altered to give a non work-hardening curve. To take account of the real influence of work hardening, Thomason sets the yield point equal to the plastic instability stress. To overcome the difficulty this poses with respect to the immediate onset of instability after yield, he also proposes that the material undergoes a ficticious amount of strain ε_I prior to the onset of plastic instability. This strain ε_I can be set equal to the strain hardening exponent, n, for materials which deform according to the power law $\sigma = K\varepsilon^n$.

The crack tip model adopted by Thomason is that of a wedge shaped plastic zone similar to the model proposed by Dugdale[29], and is shown in Figure G.

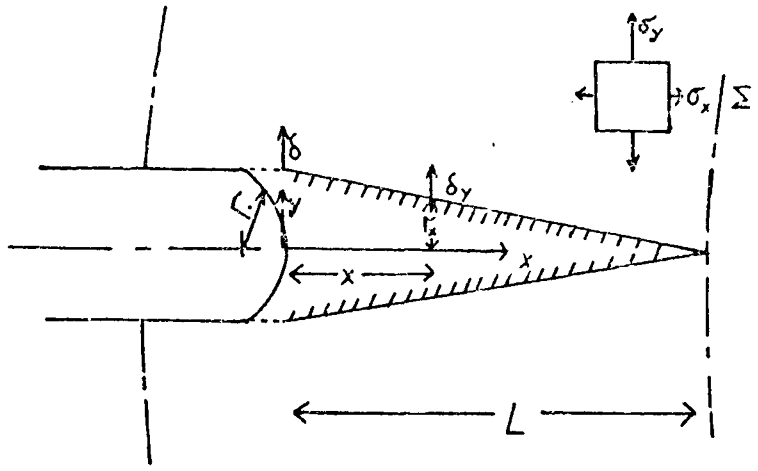

FIGURE G

The expressions used for crack opening displacement and plastic zone size are those derived by Dugdale, suitably altered to take account of plane strain conditions.

The stress distribution within the wedge zone was obtained using Hill's[42] rigid plastic slip-line field solution for plane strain deformation at the tip of a crack of finite radius, and parallel sides. Hills' solution, however, does not adequately describe the strain distribution which falls from a maximum at the crack tip to zero as $x \rightarrow L$ at the elastic-plastic boundary. This is overcome by assuming a linear decrease in the plastic displacement on the wedge boundary from the crack tip to $x = L$ i.e.

$$\delta_y = \frac{\delta r_x}{r}\left(1 - \frac{x}{L}\right)$$

From this relationship, the strain distribution is easily determined

$$\ln(\varepsilon_y)_x = \ln\left(1 + \frac{\delta_y}{r_x}\right) = \ln\left[1 + \frac{\delta}{r}\left(1 - \frac{x}{L}\right)\right] \qquad (20)$$

The final relationship obtained, relating the critical stress intensity factor, K_{IC}, and strain hardening exponent, n, is

$$\frac{K_{IC}}{Y} = \left\{ \rho \left[4.62 \left(\frac{E}{Y}\right) \frac{(e^{n}-1)}{(1-\nu^{2})} + 8.81 \tan \left(\frac{\pi}{2} \left(1 - \frac{V_f}{0.09} \right) \right) \right] \right\}^{\frac{1}{2}} \qquad (21)$$

where Y is the material yield strength

and V_f is the volume fraction of void nucleating particles.

The resultant equation agrees with the two previous models discussed[36, 37], in indicating a considerable dependence of fracture toughness on strain hardening exponent, but differs from the other two in that it does not indicate a linear dependence of K_{IC} on n. For small values of n, Thomason's equation approximates to a parabolic relationship between K_{IC} and n.

Using true stress-true strain and toughness data assembled by other workers the theoretical predictions of equation (21) were compared with experimental results. Because of the dependence of his equation on crack tip radius , he chose typical values of 0.0005 inches and 0.001 inches and plotted K_{IC}/Y versus n. The experimental points could be seen to correlate quite closely with the theoretical line for ρ = 0.0005 inches whilst there was some scatter to the upper line for ρ = 0.001 inches.

CHAPTER 3

EXPERIMENTAL PROCEDURES AND APPARATUS

3.1. Materials

At the outset, the intention was to test materials with varying carbon and manganese contents, and to determine the variations in strain hardening behaviour and toughness with composition over a range of temperatures at and below ambient.

3.1.1. Laboratory produced materials

A vacuum induction furnace with a capacity of 30 Kg was used in an attempt to produce the required materials. A number of casts were made using high purity electrolytic iron as a base material, and carbon as a deoxidising agent. Any alloy additions were made with high quality ferro-alloys, immediately before pouring into a round cast iron mould.

The ingot thus produced, was forged to 60 mm square bar, and the first two casts were then hot rolled to 35 mm square bar, ready for heat treatment and machining. Metallographic examination of these first two casts after heat treatment revealed however, that the material was inhomogeneous with respect to grain size. To try to remedy this situation, future casts were cold rolled, rather than hot rolled, with the hope of producing a more homogeneous recrystallised structure after heat treatment.

Although some success was achieved by this latter route, the grain sizes produced still tended to be somewhat variable, and as will be seen later, this structural inhomogeneity was very well reflected in the mechanical test data. Details of these laboratory produced materials, and their heat treatments are given in Table 1.

In addition to the problem of obtaining a homogeneous material in the laboratory casts, difficulty was encountered in obtaining sufficient material from a single cast to allow the tensile and toughness properties to be determined over a reasonable temperature range. In view of these two factors, it was decided to abandon further attempts to produce laboratory casts, and the alternative of employing commercially produced steel plate was adopted.

3.1.2. Commercial materials

The commercial plates were obtained from various sources, and were generally classed for use as "structural steels". Since a far larger volume of a given material was available, this permitted both toughness and tensile testing to be carried out over a wide range of temperatures for each individual composition. Details of these commercial alloys, and any heat treatments carried out are given in Table 2.

3.2. Test Temperature Control

The commercial range of alloys were tested at temperatures in the range $20^{o}C$-$196^{o}C$. Temperatures below ambient were attained in both tensile testing and toughness testing by equilibrating the test specimens with a liquid at the required temperature. The temperature of the liquid medium was continuously monitored by means of an accurately calibrated thermometer.

Temperatures in the range 0°C to -110°C were obtained using absolute alcohol in conjunction with solid carbon dioxide or liquid nitrogen. Solid carbon dioxide-alcohol mixtures attain a stable temperature equilibrium at -77°C, but any temperature in the interval between ambient and -77°C could be maintained with an accuracy of $\pm\frac{1}{2}$°C. Below -77°C, alcohol can be further cooled, by addition of liquid nitrogen, down to its freezing point at -115°C. However to avoid excessive solid alcohol formation, the mixture was used only down to -110°C. Again temperature control could be maintained to $\pm\frac{1}{2}$°C.

Freon 12, which has a boiling point of -32°C, was also used as a cooling medium. In a similar manner to that described above for alcohol, stable temperatures in the range -32°C to -77°C could be obtained using Freon 12- solid carbon dioxide mixtures. Once again temperature control could be maintained at $\pm\frac{1}{2}$°C, although Freon 12 mixtures seemed to give more stability than alcohol mixtures. Further cooling of Freon 12 with liquid nitrogen results in a stable equilibrium mixture at the freezing point of Freon 12, -153°C. Temperatures of this mixture could be maintained to an accuracy of ± 1°C, but it was found impossible to use the equilibrium freezing mixture, because excessive Freon 12 "ice" formation became prevalent, and the lowest temperature successfully maintained with Freon 12- liquid nitrogen was -133°C.

The lowest test temperature used, -196°C, was obtained by equilibration with liquid nitrogen.

It was found that all the mixtures described above could be successfully contained within an expanded polystyrene container for extensive periods, without any apparent degeneration of the container occurring. The tensile test rig (Figure 1) and the toughness test rig (Figure 2) were both enclosed in polystyrene containers for sub-ambient testing.

3.3. Mechanical Test Facility

All tensile and toughness tests were carried out on an Instron Universal Testing Machine of 10,000 Kg capacity. This machine operates on the screw principle with one stationary and one moving cross-head.

Load is measured by the normal load cell arrangement, and the load cell signal can be easily calibrated before commencement of the test.

The standard recording facility consists of a moving chart pen recorder, which operates at a constant pre-determined chart speed. Thus, during normal tensile testing, knowing the velocity of the moving cross-head, one can obtain an exact measure of elongation at any given point.

The load signal is transmitted to the pen assembly which travels perpendicular to the direction of travel of the chart, and thus a load elongation record is obtained directly from the test record.

The test facility also incorporated a servo chart drive system, whereby chart movement was governed by an input signal from a strain gauge extensometer. This system was easily calibrated so that any movement of the extensometer could be related to chart movement.

3.4. Tensile Testing

Two types of tensile test piece were used during this investigation:

(a) The standard number 14 Hounsfield specimen, the dimensions of which are shown in Figure 3.

(b) From several of the materials investigated, much larger tensile specimens were manufactured, having a gauge length of 50 mm, and a diameter of 9.1 mm. This larger specimen size facilitated the use of a strain gauge extensometer to measure extension. Details of the specimen design are given in Figure 3.

The use of the larger specimen in conjunction with the strain gauge extensometer permitted a comparison to be made between the simpler recording system, using a constant chart speed which must be used with the standard No. 14 Hounsfield, and the more sophisticated record obtained from the extensometer.

3.4.1. Tensile Test Procedure

Tensile tests were performed on twelve alloys, over a range of temperatures between 20°C and -196°C. The tensile test assemblies are shown in Figure 1.

As can be seen in Figure 1, different gripping arrangements were employed for the two types of tensile test piece used in this investigation. Standard split chuck grips were utilised for the No. 14 Hounsfield specimens, whilst friction grips had to be employed for the testing of the larger specimens.

All tensile tests were carried out at an intial strain rate of 1.5 x 10^{-4} sec^{-1}. Strain rate could not be maintained constant during a test, because the available test facility offers only a constant rate of elongation, but a typical figure for strain rate at the ultimate tensile strength was 1.2 x 10^{-4} sec^{-1}.

A chart speed of 2cm. min^{-1} was employed for all tensile tests performed with No. 14 Hounsfield specimens. It was found that this chart speed used in conjunction with the rate of elongation of the specimen provided a satisfactory magnification of specimen elongation (100 times magnification). This enabled accurate analyses of chart records to be carried out.

The highest magnification of extensometer movement to chart movement was utilised during testing of the larger specimens, this method again yielding chart records amendable to accurate analysis.

Various load ranges could be selected, whereby full scale pen deflections of 200 Kg, 500 Kg, 1000 Kg, 2000 Kg, 5000 Kg, and 10, 000 Kg could be obtained. Testing of alloys P9 and P10 was carried out using a refinement of this load indication system, whereby any full scale deflection could be divided into ten full scale deflections, each new deflection being equivalent to a tenth of the original full scale deflection load. This technique permits more accurate measurements of test data to be made, particularly in the area of the ultimate tensile strength, where large increases in strain may occur with relatively small increase in load. Comparative tests were carried out to ensure that no significant variation in results was obtained when this more sensitive load monitoring technique was utilised.

To ensure that the test piece and test assembly were at equilibrium with the surrounding cooling medium during sub-ambient testing, the temperature of the whole assembly was maintained at the test temperature for thirty minutes prior to the commencement of the test. It is most important, particularly at lower test temperatures to ensure that the submerged portion of the loading bars have reached equilibrium, as any contraction of these bars during testing will obviously lead to an erroneous test record. When using Freon 12 and liquid nitrogen as the cooling medium, especially near the freezing point of Freon 12, even small additions of liquid nitrogen to the bath, led to the formation of Freon 12 "ice" round the upper loading bar. The "ice" formation was seem to coincide with an irregularity in the test record, this being an instantaneous increase in load, and obviously local contraction of the upper loading bar was occurring, This problem was overcome by placing a glass tube in position round the submerged portion of the loading bar, thus preventing "ice" formation on the loading bar itself.

3.4.2. Analysis of Tensile Test Records

The test record is a plot of load versus elongation. It is required to convert the load axis to true stress σ_T, and the elongation axis to true plastic strain ε_T. Definitions of both of these parameters are given in Appendix A.

All test records, with the exception of those obtained from test pieces of alloys P9 and P10, have been analysed "manually". Measurements of elongation at known loads were taken from each test record and the sets of co-ordinates were then processed using a programmable calculator, to give true stress-true strain values.

An alternative approach to test analysis was employed with test results obtained from alloy P9. The x-y co-ordinates of each test record were punched out on paper tape using a "D-Mac' table plotter. This instrument operates on the "magic-eye" principle in that one follows the curve with a pointer the co-ordinates of any desired point being punched out at will.

An Algol computer programme was written, to analyse the test data thus obtained. The programme was devised to calculate true stress-true strain values for each set of co-ordinates, and then to perform a linear regression analysis on the log true stress-log true strain data. The regression analysis was carried out simultaneously from opposite ends of the curve. The reason for this is discussed in Chapter 4.1.3.

From the true stress-true strain curves obtained, the true work hardening rate per unit strain was calculated for alloys P6-P11. To facilitate this determination, large scale true stress-true strain curves were drawn, and using an accurate drawing board protractor with vernier scale, the angles of tangents to these curves could be measured at any desired strain, to an accuracy of ±5 minutes. In view of the inaccuracies involved in constructing true stress-true strain curves, this accuracy of angle measurement was considered to be satisfactory. The work hardening rate per unit strain could now be calculated simply by determining the tangent of this angle.

The final piece of information extracted from the tensile test records was the Lüders strain at each test temperature for alloys P6-P11. Alloy P7 deformed homogeneously and therefore exhibited no Lüders strain.

3.5. Crack Opening Displacement Testing

Crack Opening Displacement (C.O.D.) tests were performed, to determine the critical C.O.D., initially at room temperature (alloys P1 - P5) and ultimately over a range of temperatures, between 20°C and -196°C (alloys P6-P11).

All C.O.D. tests were carried out using three point bend specimens, and a suitably constructed test jig.

The occurrence[30, 43] of slow crack growth prior to fracture, or the attainment of maximum load during fracture toughness testing of low strength steels, has been reported in the literature, and it was considered necessary to determine the point at which stable slow crack growth commenced. The potential drop technique was employed[44, 45] to determine the onset of this critical event.

The C.O.D. values thus obtained were then considered to be the critical parameters for that material, at the temperature and displacement rate of the test.

All procedures were carried out in accordance with the Draft for Development for Crack Opening Displacement Testing [46] DD19 : 197 issued by the British Standards Institution.

3.5.1. C.O.D. specimens

Three point bend specimens of cross section 25 mm x 25 mm and 120 mm long, were machined from the materials to be tested. V-notches were milled, in the appropriate orientation, to a depth of 4 mm, and were found to be sharp enough to act as fatigue crack starters. The pre-cracking of these specimens by fatigue will be discussed in Section 3.5.2.

Test pieces manufactured from alloys P8-P11 were in the longitudinal mode, with the notch placed in the transverse direction, whilst test pieces of alloys P6 and P7, were in the transverse mode with the notch in the longitudinal direction.

A schematic representation of the standard three point bend test piece used in this study is shown in Figure 4.

3.5.2. Specimen pre-cracking

Pre-cracking was carried out on an Amsler Vibrophore fatigue machine in the three point bend mode. The total final fatigue crack length was 4.5 mm, giving a total crack length of 8.5 mm (Figure 4).

The maximum permissible fatigue stress intensity value (K_f) permitted by DD19[46] is that which ensures only very small amounts of plastic deformation at the crack tip, i.e. K_f should be less than the ideal plane strain limit during any stage of the fatigue cracking process.

This requirement is fulfilled when $K_f < 0.63\ \sigma_y B^{\frac{1}{2}}$. Values of fatigue force (P_f) are calculated using the equation:

$$K_f = \frac{P_f Y_f}{BW^{\frac{1}{2}}}$$

where Y is a function of (a/W).

The maximum permissible fatigue stress intensity values, together with the fatigue stress intensity values during the final stages of fatigue are listed in Table 3 for the alloys tested.

The pre-cracking period was always greater than 1.5×10^5 cycles, and the average operating frequency was 60Hz.

Recent work[47] has suggested that maintaining the fatigue stress intensity within the limits prescribed above is not entirely necessary, and indeed the indications are that the use of fatigue stress intensities above the plane strain limit, lessens the amount of scatter obtained in the measurement of C.O.D.

Trouble was encountered initially, at the pre-cracking stage, in that fatigue cracks seemed to propagate preferentially on one side of the specimen surface, sometimes to the exclusion of any growth on the opposite face. Investigation of this problem indicated that fatigue crack growth was inhibited on the specimen surface from which the

V-notch cutter exited. Close examination of this region revealed an area of heavy deformation around the root of the V-notch. This difficulty was overcome by grinding 0.15 mm off the affected surface after notching.

3.5.3. C.O.D. test rig: A schematic representation of the test rig is shown in Figure 2. The specimens were tested in three point bending over a span of 100 mm, using 20 mm diameter rollers.

The standard Instron load cell was used in compression in order to record load.

The test piece holding assembly was separated from the loadcell by a 20 cm long, 8 cm diameter bar. The bar was wound with copper tubing, and during testing at sub-ambient temperatures, a constant flow of cold water was maintained through the tubing. This precaution was taken to prevent the load cell temperature falling below 270°K which may cause the load cell to perform in an electrically unstable manner.

3.5.4. Measurement of C.O.D.

One of the problems associated with the acceptance of C.O.D. as a valid toughness parameter has been the great difficulty involved in its measurement. There is no means available at present, whereby the C.O.D. at the tip of an infinitely sharp crack, e.g. a fatigue crack, can be autographically monitored.

The intial approach[28] was to use specimens containing slots of finite width, into which was placed a "paddle codmeter." This instrument consisted basically of a rod with a very fine paddle shaped tip, which was positioned at the base of the notch, and the paddle was held against opposite faces of the notch by a torsional force applied to the rod. As the crack opened the torsional force impelled the paddle to rotate, and this rotational movement was translated to a horizontal movement in a transducer, which thus permitted the autographic recording of the event. The movement of the paddle could be calibrated to yield a linear relationship between paddle movement, and change in potential measured through the transducer.

Unfortunately no great success was achieved in reproducibility using this technique, and it is no longer in general use.

Angle of bend[24] has been suggested as a possible method for measuring C.O.D., and photographic techniques have also received some attention.

Notch root contraction [48], because of its proposed equivalence with C.O.D., has been proposed as a more informative fracture criterion, in that it is also believed to indicate the plane strain-plane stress transition. Results presently available[49] suggest a very wide scatter is obtained by this method, and at the moment notch root contraction is not being widely used.

The method currently most favoured for the measurement of C.O.D. is the double beam cantilever clip gauge shown in Figure 5. C.O.D. is not measured directly at the crack tip, but the gauge is affixed to knife edges, attached across the mouth of the specimen notch as shown in Figure 2.

The success of this technique depends to a large extent upon knowledge of the relationship which exists between C.O.D., and the specimen surface displacement.

Initially it was assumed that surface and crack tip measurements could be related assuming a fixed centre of rotation in the ligament below the crack tip[50]. However evidence obtained since suggests that during the intial stages of deformation, the centre of rotation moves, from a point close to the crack tip, to a point 0.454 of the ligament below the crack tip, and then remains essentially constant.[51, 52]. Fortunately this constant rotational centre is achieved fairly quickly at small C.O.D. values. Experimental verification of this in the present study is reported in Section 4.2.1.

A schematic representation of the notch profile during bending is shown in Figure 6, and the relationship between surface displacement and crack tip displacement is:

$$\frac{V_g}{\delta} = \frac{a + Z}{1/r\,(W-a)} + 1 \qquad (23)$$

(This is derived in Appendix B).

The assessment of the critical event during toughness testing of low strength ductile materials is another major problem. Most low strength materials at ambient temperatures do not exhibit fast fracture. Typical curves of C.O.D. versus load for a high, medium and low strength material are shown in Figure 7.

Curve (a) could be analysed using linear elastic fracture mechanics, whilst curves (b) and (c) are clearly outwith the elastic regime, and must be treated using general yielding fracture mechanics.

It is possible in the cases of curves (b) and (c) that slow crack growth may precede the fracture event,[43, 53] and it has been suggested that for material behaviour similar to that depicted by curve (c), the C.O.D. at maximum load should be assessed as the critical parameter. There is considerable evidence however to indicate that slow crack growth occurs before the attainment of maximum load[43, 53].

Several techniques have been proposed for the detection of slow crack growth[44, 45, 54, 55]. The method which has attracted most attention is that of potential drop. This was the technique adopted in the present study for testing of alloys P6-P11.

A diagrammatic representation of the circuit employed is shown in Figure 8.

A constant current of 40 amperes was fed into the specimen, and the potential developed across the crack was measured on a time based chart recorder. The potential measuring probes were placed diagonally opposite one another on opposite sides of the notch mouth as shown in Figure 8(a). Steel wire probes were used, and each probe was positioned 2 mm from the notch. The exact positioning[56] of the probes however has been shown not to significantly affect the accuracy of the measurement.

Use of this technique requires that the test piece be entirely insulated from the testing machine. This was achieved using Tufnol sheet as a base for the rollers, and PTFE sleeves for any bolts which connected the testing machine to the test piece area.

3. 5. 5. C.O.D. test procedure

Specimen dimensions W and B (See Figure 4) were measured with a micrometer before testing. Three point bend testing was carried out over a span of 4W i.e. 100 mm and therefore the two lower rollers were placed parallel to, and 50 mm on either side of the top roller (Figure 2).

Clip gauge calibration was carried out, at least, after every third test, and before each test the gauge was closely scrutinised to determine whether any repairs need be carried out. It was ascertained, by calibrating the clip gauge at room temperature and at -196°C that no discernible variation in clip gauge calibration occurred within the temperature range of interest, and therefore no matter what the test temperature, it was considered valid to calibrate the clip gauge at room temperature.

Knife edges were attached to the specimen, and the clip gauge safely seated in position between them. The specimen was now placed astride the two lower rollers, with the notch mouth parallel to and halfway between them. The supply leads from the constant current supply source were then bolted to the specimen through two mild steel sheet lugs which had previously been spot welded to the specimen ends (Figure 2). The two potential probes were then connected through the potential measuring circuit.

Temperature control was obtained as described in Section 3.2. The specimen and test assembly were maintained at the test temperature for thirty minutes prior to testing. All tests were carried out at a constant X-head speed of 0.02 $cm.min^{-1}$. Two test records were obtained from each test carried out:

(a) A record of load against clip gauge opening.

(b) A reocrd of change in potential against time.

3.5.5.1. Post C.O.D. test measurements

In the cases where slow crack growth was the critical event, and no fast fracture occurred during testing, the following procedure was adopted to facilitate examination of the fracture surface and measurement of the exact crack length.

The specimen was immersed in liquid nitrogen and left for ten minutes to equilibrate. Brittle fracture of the remaining ligament could now be achieved simply by delivering a blow, with a heavy metal instrument, to the centre portion of the underside of the specimen which was supported at its extremities by two metal blocks. Degeneration of the fracture surfaces with time was avoided by application of an acetone soluble lacquer.

Crack length measurements could now be made on one of the specimen halves, using a Nikon projection microscope at a magnification of x 50. These measurements were carried out in accordance with B.S. DD19:1972[46], and where crack lengths measured were within the required scatter band, the maximum crack length measured was used in the calculation of C.O.D.

3.5.5.2. Analysis of C.O.D. test records

The recommended recording procedure with the potential drop technique, is simultaneous autographic recording of load versus clip gauge opening, and change in potential versus clip gauge opening. However only one X-Y recorder was available, and load versus C.O.D. was recorded on this, whilst potential change versus time was recorded on a constant chart speed recorder.

In order that the two records might be compared, location marks were placed at fifteen second intervals on the load clip gauge opening displacement chart during testing, and in this way accurate records of clip gauge opening displacement against change in potential could be drawn after completion of the test. Typical results are discussed later in Section 4.2.2.

During the initial stages of the testing programme, fractographic techniques were used to confirm that the experimental technique being employed did accurately predict the point of initiation of slow crack growth.

3.5.5.3. Fracture surface examination

A scanning electron microscope was employed in the examination of fracture surfaces. The region of slow crack growth could be easily distinguished from those of brittle fracture and fatigue crack growth.

Optical macro-examination techniques were also employed in the study of fracture surfaces, but were found to supply little useful information.

CHAPTER 4

RESULTS

In all, eleven alloys were investigated, and details of each of these alloys are given in Tables 1 and 2. The alloys were chosen to represent a range of carbon-manganese contents and various strength levels. The effect of grain size on strain hardening exponent and critical C.O.D was investigated in alloy P11.

4.1. Tensile Test Results

4.1.1. Flow curves

Tensile tests were carried out on each alloy investigated, over a range of temperatures between 20°C and -196°C. In each case, the load elongation information obtained was converted to true stress-true strain data. Flow curves for each test temperature could now be constructed, and a typical family of flow curves is shown in Figure 9 (alloy P6).

This Figure illustrates the effect of a decrease in deformation temperature on flow stress. This effect is however more ably described in Figure 11, which shows a plot of true stress, measured at 6% true strain, against deformation temperature for alloys P6-P11. It is well known that low alloy steels exhibit a marked temperature dependence of flow stress, as the deformation temperature is reduced below ambient and Figure 11 amply illustrates this point.

As was mentioned earlier in Chapter 3 (Section 3.1.1) great difficulty was experienced in obtained reproducible flow curves from alloys which had been laboratory produced in a vacuum induction furnace. An example of this variable behaviour can be seen in Figure 12 which compares the results of two tensile tests carried out on alloy P4 at -30°C. An unacceptable variation in mechanical properties obviously exists within this alloy, and since this type of behaviour is similar to that obtained for alloys P1, P2, P3 and P5, no further analysis of the flow curves for these alloys was carried out.

The probable reason for this behaviour can be deduced from Figure 13 which shows a photo-micrograph of an etched section of alloy P4. Large variations in grain size, typical of all the laboratory produced materials, can be seen to occur within this alloy. It was found impossible to homogenise the grain structure, probably because large amounts of deformation could not be imparted to the material since the final size of the forged and rolled bar was controlled by the cross-section of the C.O.D. specimens required (25.4 mm x 25.4 mm).

In view of this, the results obtained with Alloys P1-P5 will be discussed no further, and attention will be focused on alloys P6-P11.

The room temperature tensile properties of alloys P6-P11 are summarised in Table 4.

4.1.2. Lüders strain

Of the alloys of interest (P6-P11) only alloy P7 exhibited homogeneous yielding, the rest yielding discontinuously. Since it has been suggested that the Lüders strain may affect the analysis of flow curves using Ludwik's or Hollomon's equations[9], the Lüders strain was measured in each test performed, and the variation of this parameter with temperature is shown in Figure 14. As can be seen decreasing the deformation temperature has a marked effect on increasing the extent of Lüders strain. For example, for alloy P6, a reduction in deformation temperature from 20°C to -196°C, increases the extent of Lüders strain from 1.44% true strain to 3.80% true strain.

4.1.3. Strain Hardening Exponent Values

Strain hardening exponent (n) values were calculated for each tensile test carried out. These n values are obtained by plotting log σ_T against log ε_T for each flow curve, and if deformation can be described by Hollomon's equation (Equation (1)) then a straight line plot will result.

Assuming a straight line plot is obtained, then the strain hardening exponent is simply derived by measuring the slope of the line since,

$$\sigma_T = K\varepsilon_T^n$$

$$\log \sigma_T = n \log \varepsilon_T + \log K$$

Initially these plots were constructed as shown in Figures 15a and 15b, but because of the volume of tests performed, it was decided to use log-log graph paper for this purpose. No reduction in accuracy of measurement of n values resulted from the use of log-log graph paper.

In the latter part of the study, a further simplification of the process for determining the strain hardening exponent was devised, in that a computer programme was written, which could produce 'n ' values from an input of load-displacement co-ordinates. Strain hardening exponent values were produced for alloy P9 by this method, by carrying out a linear regression analysis on the log σ_T, log ε_T points. As will be seen later, in most instances, two distinct ' n ' values were required to described the flow curves obtained. To estimate as accurately as possible these two 'n ' values, a double linear regression analysis was carried out simultaneously from the high and low strain ends of the flow curve. The division of experimental points which gave maximum values for the two co-efficients of linear correlation was accepted as an indication of the transitional strain, and the corresponding values of the strain hardening exponents, n_B and n_C, were noted.

To check the accuracy of the automated technique, ten sets of strain hardening exponent values were calculated manually, using a log σ_T v log ε_T plot, and compared with those obtained by computer analysis. The results in all cases were seen to agree to the second decimal place, and in many instances to the third decimal place.

A manual plot of log σ_T v log ε_T for alloy P9 tested at 20^{o}C is shown in Figure 16 and the results for strain hardening exponent values obtained by both methods are compared.

Use of the stepped zero suppression facility described earlier in Chapter 3.4.2 led to no reduction in accuracy or reproducibility of the strain hardening exponent values obtained, but enabled much more accurate evaluation of true-stress-true strain data in the region immediately preceeding the onset of plastic instability.

Strain hardening exponent values obtained for alloys P6-P11 for the various test temperatures between 20^{o}C and -196^{o}C are listed in Appendix C. Tests were normally carried out in triplicate, and the results listed in Appendix C indicate the extent of scatter in 'n'. The corresponding values of K, the strength co-efficient are also given in Appendix C.

Where two stage hardening has occurred, the initial value of n (low strain region) is denoted by n_B, whilst the final value of n (high strain region) is denoted by n_C. In the case of single stage hardening, the strain hardening exponent is denoted by n_A.

The variation of strain hardening exponent with temperature is depicted in Figures 17-21. These curves are drawn through the average value for strain hardening exponent obtained at each temperature, whilst the barred lines indicate the scatter obtained around these average values.

Results obtained using a strain gauge extensometer are denoted in Appendix C by the suffix 'e'. All these tests were of necessity carried out at ambient temperature, and as can be seen from the tabulated results, no significant difference in results was obtained using the extensometer to record elongation. This indicates that no variation in deformation characteristics occurs with change in specimen size since specimens of a larger cross section were used in conjunction with the extensometer (Chapter 3.4.1.).

Also as a result of this finding, the recording system used for determination of load-extension data for the smaller specimens can be considered to be sufficiently accurate (Chapter 3.4.2).

4.1.3.1 Transition strain

In all cases where two stage hardening has occurred, the strain at which the transition $n_B \longrightarrow n_C$ was noted. The variation of transition strain with temperature is shown in Figures 22(a-d).

4.2. Crack Opening Displacement Test Results

Crack opening displacement tests were carried out on all the alloys, to determine the variation of critical C.O.D. with test temperature. The critical parameter chosen was crack opening displacement at the point of crack initiation, the potential drop technique being employed to determine this critical event.

4.2.1. Rotational factor

Before assessments of crack tip opening displacements (C.O.D.) can be made from displacement measurements obtained at the surface of a toughness specimen, knowledge of the relevant rotational factor in Elliot and May's relationship (Appendix B), in the C.O.D. range of interest must be obtained.

In the present investigation, the photographic technique was employed, whereby photographs were taken of the crack tip region at known points in time during the toughness test. A zoom lens was used, giving an instantaneous magnification of x 2, and measurements of the actual C.O.D. were made from the photographic film on a projection microscope at a magnification of x 50. The C.O.D. values obtained could now be related to the surface displacements as indicated on the autographic chart record of load v displacement.

Substitution of these values for C.O.D. and surface displacement V_g into Elliot and May's formula yield a value for the rotational factor thus,

$$r = \frac{(Vg/\delta - 1)(W-a)}{(a + Z)} \tag{24}$$

Figure 23(a-d) shows 4 photographs from a series, indicating the gradual opening of the crack with increasing load. Figure 24 shows the plot obtained for Vg v r for alloy P8 tested at 20°C. As values of V_g decrease below 0.2mm, the curve appears to become asymptotic to the r axis, indicating rapid changes in r values occurring with only small changes in displacement. As displacement increases above $\sim$ 0.2mm, the value of the rotational constant r becomes invariant at a value of $\sim$ 2.5.

This constant value of r is attained very rapidly, and because of this, in all measurements made during this investigation, a value of 2.5 has been assumed for the rotational constant in Elliot and May's relationship. This value of r is very similar to that obtained by other workers [41, 57] ($r = 2.2$).

As can be seen from Figures 23(c) and (d), a small amount of crack extension has occurred at the tip of the crack, but measurement of the opening at the original crack tip still yields a value of $r \sim 2.5$ as shown in Figure 24.

4.2.2. Potential drop technique

The potential drop technique was found to give adequate indication of the onset of slow crack growth, and evidence of this from scanning electron micrographs will be presented in Section 4.4. Figure 25 shows a typical result obtained for potential change versus

C.O.D. As can be seen the resultant plot displays several distinct regions or sectors. The initial flat region at very low C.O.D. values corresponds to the occurrence of elastic deformation, followed by a curved region which corresponds to the commencement and propagation of yield through the specimen. The following two sectors are essentially linear, the first indicating the continuence of homogeneous deformation, whilst the second sector, of greater slope than the first occurs as a result of the forward movement of the crack front.

Although very stable measurements of change of potential were obtained from tests conducted at 20°C, -77°C and -196°C, great care had to be exercised when temperatures intermediate to these were used. The three above mentioned temperatures are equilibrium temperatures for various conditions and mixtures (atmosphere, solid carbon dioxide plus alcohol, and liquid nitrogen respectively) and rigid temperature stability could be relied upon. Itermediate temperatures, in the range 20°C to -77°C, were maintained by measured addition of solid carbon dioxide to alcohol. It was found that small local changes in temperature at the specimen-potential measuring probe interface, led to unacceptable instability in the potential measuring system. This potential instability was ascribed to the occurrence of a "thermocouple effect'. The problem was overcome by maintaining the specimen and test rig at the required temperature for one hour prior to testing, and then carrying out the test with no further addition of coolant. Much greater stability of potential measurement was then obtained, and in most cases the temperature of the system remained virtually constant during testing. In instances where large instabilities were seen to occur in the potential measuring system, the result was discarded.

4.2.3. Critical crack opening displacement values

The results of the crack opening displacement tests carried out are listed in Appendix D. The values of crack-length used in calculation of the critical C.O.D.'s are also listed in Appendix D. An indication is given as to which tests resulted in slow crack growth occurring as the critical event. All other tests produced fast fracture failure without any prior slow crack growth.

The variations of critical C.O.D. values with temperature for alloys P6-P11 are presented in graphical form in Figures 26-28.

4.2.4. Charpy test results

Charpy impact tests were carried out on alloys P6-P11 over the temperature range -196°C to 100°C. The energy-temperature results are presented in Figures 29a-c.

It will be noted that the upper shelf energy levels vary from 170 ft.lb (P10) to 25 ft. lb. (P6). The 15 ft.lb. energy temperatures vary from 98°C (P6) to 5°C (P9). Transition temperatures for the alloys lay in the range, -100°C (P6) to 40°C (P9). The maximum temperature employed in the Charpy tests namely 100°C, was not sufficiently high to determine the upper shelf energy level for alloy P7.

The effect of grain size on impact test results can be seen from Figure 29c. Increasing the grain size increased the transition temperature and led to a higher upper shelf energy level.

4.3. Optical Microscopy

The microstructures of the alloys investigated are shown in Figures 30(a)-(g). All alloys were found to be ferritic-pearlitic in nature, with the exception of alloy P7, which consisted of ferrite grains in a bainitic matrix.

The pearlite content of each alloy, where applicable, is listed adjacent to its photomicrograph (Figures 30(a)-(g)).

The grain sizes for all the materials used, were obtained by the linear intercept method, and are listed in Table 2. The grain sizes of the alloys varied from 4.5 μ for alloy P6, to 42 μ for alloy P11 in it coarsest condition.

Table 5 lists information on sulphide and oxide inclusion contents obtained from use of a Quantinet IIB. Projected lengths and percentage area values are listed for sulphide and oxide inclusions. Inclusion sizes in alloys P6 and P11 were too small to obtain any information other than the total projected inclusion length. Alloys P6, P7, P9, P10 and P11 have total projected inclusion lengths in the range 0.47 - 0.67 mm.mm^{-2}, whilst alloy P8 has a total projected inclusion length of 1.5 mm.mm^{-2}.

4.4. Scanning Electron Microscopy

A Scanning Electron Microscope was used to examine fracture surface morphologyps after testing, and in particular was used as a means of checking the validity of the potential drop technique as an indication of the commencement of slow crack growth.

Various scanning electron micrographs are shown in Figures 31(a)- (g). The fracture surface of alloy P8 tested at 20°C (Specimen number 22) is depicted in Figure 31(a). This shows the

the boundary between the region of slow crack growth, characterised by the presence of voids, and the region of cleavage fracture induced by fracture of the test specimen ligament at -196°C after testing. Figure 24 shows the corresponding potential change v C.O.D. plot for this specimen, and the onset of slow crack growth suggested by this plot has been confirmed by scanning electron microscope examination.

Figures 31(b)-(g) show the fracture surfaces of alloys P8(-32°C), P8(-77°C), P9(-60°C), P9(-77°C), P10(20°C) and P10 (-77°C) respectively. These scanning electron micrographs will be discussed in detail in Section 5.2.1.

CHAPTER 5

DISCUSSION

Work Hardening Behaviour

Analysis of the tensile test data in terms of Holloman's equation indicated that the behaviour of all the alloys could be described well by this relationship. Alloy P7 was characterised by single stage hardening while the work hardening of the other alloys was best described by double n behaviour.

5.1 Strain Hardening Exponent

The variation of strain hardening exponent, n, with temperature for all the alloys shows the same general trend, as is illustrated in Figure 17-21. As temperature of deformation is lowered below ambient the strain hardening exponent values increase, and attain a maximum value before further reduction in deformation temperature leads to a reduction in the value of strain hardening exponent. The maximum values of n for the various alloys occurred over a range of temperatures from -30°C to -120°C. Earlier reports[4, 5] on the variation of strain hardening exponent with temperature, suggested that as test temperature was reduced from 600°C to ambient, an increase[4] in strain hardening exponent was observed, whilst a further reduction in deformation temperature to -70°C led to a decrease[5] in n, in agreement with the trends observed in the present work. The reasons underlying this type of variation in n with temperature are discussed later.

5.2 Transition Strain

In all cases where duplex strain hardening behaviour occurs, a strain value may be identified at which the transition from primary (n_B) to secondary (n_C) hardening takes place. This is illustrated in Fig. 16 where the transition strain for alloy P9 tested at 20°C can be identified as $\mathcal{E}_i = .066$.

As indicated in the literature review, previous workers have suggested that the transition strain corresponds to a change in dislocation substructure and is temperature dependent. Morrison[5] found that, in a .09%C, the transition strain increased with decreasing temperature. The slope of his $\mathcal{E}_i$ VT plot was -9×10^{-4} $^oC^{-1}$ and this was stated to be the same as that for the variation in dislocation cell formation strain with temperature in pure iron reported by Keh and Weissmann[8].

From Figs. 22 (a - d) it is apparent that considerable scatter was obtained in transition strain values in the present work, indeed it is doubtful if the existence of a definite transition strain is established. However the regression lines drawn from the data confirm the general trend for $\mathcal{E}_i$ values to increase as temperature is lowered. The slope ($d\mathcal{E}_i/dT$) is much lower than suggested by Morrison being -2×10^{-4} $^oC^{-1}$ for alloys P8, P9 and P10 while for alloy P6 the slope is almost zero, the scatter being particularly high in this case. It would appear therefore that the temperature dependence of $\mathcal{E}_i$ varies in different materials and may perhaps be affected by carbon content since P6 has the highest carbon content of the alloys tested while the others are of intermediate carbon level compared to the steel studied by Morrison.

If transition strain increases with decreasing temperature it follows that secondary hardening contributes less to the overall behaviour and below a certain deformation temperature the behaviour can be represented as single n, n_B becoming n_A. This was observed at the lowest test temperatures for all the alloys studied and evidence of the gradual transition $n_B \rightarrow n_A$ is best illustrated by the behaviour of alloy P9 in Figure 19.

All of the alloys displaying two stage hardening exhibited considerable extents of Lüders strain which increased with decreasing temperature. Thus the extent of primary hardening and Lüders strain increase simultaneously contradicting the suggestion by Christ and Smith[9] that single n behaviour is due to the "masking" effect of Lüders extension at lower strain values.

5. 3. Alternative approach to flow curve analysis

It has been suggested[6] that use of the analytical technique devised by Crussard[7] might lead to more accurate estimates of both the strain hardening exponent and the transition strain.

The basis of this approach is that, if either the Holloman or Ludwik equations (Equations (1) and (2)) adequately describe the material flow characteristics then a plot of log $d\sigma_T / d\varepsilon_T$ v log ε_T should be linear with a slope of $(n - 1)$. Since Ludwik's equation contains a term, σ_0, which should take account of the temperature dependence of flow stress, it was considered that this revised analysis could be fruitful.

Initially true work hardening rates ($d\sigma_T/d\varepsilon_T$) were measured from large scale σ_T v ε_T graphs as described earlier, and these rates were utilised to calculate strain hardening exponent values. It was immediately apparent, however, that there were large discrepancies between the n^1 values obtained from the log $d\sigma_T/d\varepsilon_T$ v log ε_T plots, and n values obtained previously from a direct log σ_T v log ε_T plot of the original data. (For convenience n^1 will be used to signify strain hardening exponent values obtained by the Crussard method). This discrepancy between n and n^1 was investigated further and to illustrate the problem, the analysis of one stress strain curve is considered in detail below.

Table 6 gives the experimental true stress - true strain values obtained in a test on alloy P6 at -10°C. A log σ_T v log ε_T plot of this data is shown in Figure 34. Computer analysis showed that the two best straight lines which could be fitted to the data were of slopes n_B = 0.237 and n_C = 0.202, the transition strain being between 4 and 5.5%. These two lines are shown on Figure 34 and it will be noted that an excellent fit is obtained. In fact when calculated values of stress from the two regression equations are compared with the experimental values, the agreement is within $\pm$ 0.1 Kg mm^{-2} in all cases, and averages 0.1% which is close to the experimental error in reading the recorder chart. It should also be noted that the slopes obtained are not altered appreciably by the omission of individual points. The stress strain curve would therefore appear to be well represented by the two regression equations :

$$\sigma_T = 42.09\,\mathcal{E}_t^{\,0.237} \quad \text{up to 5.0\% strain}$$

$$\sigma_T = 44.59\,\mathcal{E}_T^{\,0.202} \quad \text{between 5\% and 10\% strain}$$

The slopes, $d\sigma_T/d\mathcal{E}_T$, measured from the σ_T, $\mathcal{E}_T$ graph are shown in Figure 35, and the corresponding $\ln\, d\sigma_T/d\mathcal{E}_T$ v $\ln\mathcal{E}_T$ plot is given in Figure 36. It is obvious that although a reasonable linear relationship exists, and there is again an indication of double n behaviour, there is more scatter in this plot. When the slopes of the best straight lines are calculated, however, they give $n^1_B = 0.345$ and $n^1_c = 0$. This indication of zero work hardening at higher strains is of course completely unacceptable. It was considered that the difficulty might arise from errors in measuring the slope of the σ_T vs $\mathcal{E}_T$ graph and a more accurate method of determining the work hardening rate was sought.

To achieve this, the experimental true stress-true strain values were fitted to a sixth order polynomial by use of a computer curve fitting routine, and the slope of the curve was then estimated by differentiation of the polynomial. The closeness of the polynomial fit to the stress strain curve was extremely good, the maximum deviation in fit being 0.04 kg. mm^{-2}. The slope values obtained are included in Figure 35, from which it will be seen that agreement with the measured values is reasonably good except at low strains where the slope is changing rapidly. Figure 36 shows the $\ln\, d\sigma_T/d\mathcal{E}_T$ v $\ln\mathcal{E}_T$ plot obtained from these calculated slopes. Since the polynomial is fitted to the range of experimental points, the slope values at the extremities of the stress-strain curve are unreliable and were therefore neglected in calculation of n^1 values. For the best fit, shown in Figure 36, these are $n^1B = 0.381$ and $n^1C = -0.051$, which actually predicts a negative hardening rate above a transition strain of only 3.5%. The transition strain is not well defined in this plot, and the value of n^1B is found to depend critically on the transition strain selected. Thus attempts to describe the stress strain curve slope more accurately did not resolve the discrepancy between n and n^1.

The reason for the discrepancy is simply that very small changes in stress can lead to appreciable changes in slope and lead to large variations in n^1. The theoretical slope for any strain can of course be calculated from the two regression equations developed above i.e. from

$$\ln {}^{d\sigma_T}/{}_{d\varepsilon_T} = \ln n_B + \ln K_B + (n_B - 1) \ln \varepsilon_T$$

and

$$\ln {}^{d\sigma_T}/{}_{d\varepsilon_T} = \ln n_C + \ln K_C + (n_C - 1) \ln \varepsilon_T$$

These two calculated lines are shown for comparison by dotted lines in Figure 37, and the actual $d\sigma_T / d\varepsilon_T$ values are compared with those from the polynomial in Table 7, which shows the % change in slope from the two methods of approach.

It will be noted that although the average difference between the slopes above 5% strain is only 4%, this leads to the dramatic change in n_C from 0.202 to an n^1_C of -0.05.

The above is not an isolated example of disagreement between n and n^1 values. Analysis of data for the other alloys in the present work frequently produced negative n^1_C values, and also gave an apparently random variation in n^1 with temperature for a given material. Other workers[58] have also reported negative n^1 values obtained by similar analysis, but were unable to suggest an interpretation of these results.

From the present work, it is clear that no significance can be attached to these values. The stress strain curve has a continuously changing slope, and while it can be well represented by two regression lines of the form $\sigma_T = K \varepsilon_T^n$, the fit is not good enough to allow accurate prediction of the rate of change of the logarithm of the work hardening rate. The conclusion from the present investigation is therefore that the Crussard analysis offers no advantages in the prediction of transition strain and in fact is normally incapable of predicting strain hardening exponents with any degree of accuracy.

5.4. Significance of Strain Hardening Exponent

Before any significance is attached to the values of strain hardening exponent it would be useful to consider what relationship, if any, they bear to the actual work hardening characteristics of the alloys considered. The most exact method of assessing a materials work hardening characteristic is to determine the variation of the parameter $d\sigma_T/d\varepsilon_T$ with true strain, since values of $d\sigma_T/d\varepsilon_T$ measured from flow curves, unambiguously define the true work hardening rate at a given temperature and strain. Figure 38 shows the variation of the parameter $d\sigma_T/d\varepsilon_T$ with temperature for alloy P10 whilst Figure 20 indicates the variation of strain hardening exponent with temperature for the same alloy.

The work hardening rate, for alloy P10, increases in a rather orderly fashion with decreasing deformation temperature, no deviation in work hardening rate being noted till deformation behaviour at -196°C is considered. The effect is best illustrated by reference to Figure 39(e) which presents the information as true work hardening rate variation with temperature for various strains. At strains below $\varepsilon_T = 0.10$ the work hardening rate at -196°C drops from that at -110°C and this will be discussed later. However for $\varepsilon_T \geqslant 0.10$ the work hardening rate increases approximately linearly with decreasing deformation temperature.

Comparison with the relevant strain hardening exponent (n_C or n_A) in Figure 20 shows that this increases from 0.196 at 20°C to a maximum of 0.233 at -90°C and then falls to 0.163 at -196°C. Thus the strain hardening exponent does not give even a qualitative description of the variation of work hardening characteristics with deformation temperature. This is a direct consequence of the fact that reduction in deformation temperature affects not only true work hardening rates, as discussed above, but also has a marked effect on the materials flow stress as indicated in Figure 11.

An analysis of the lack of agreement between variation of strain hardening exponent and true work hardening rate with temperature may be deduced as follows. Consider an alloy which obeys the Holloman equation and whose work hardening behaviour at temperature T1 is as shown in the σ_T v ε_T and log σ_T v log ε_T plots A and D in Figure.32.

If the deformation temperature is reduced to T2 producing an increase in flow stress $\Delta\sigma_T$ but no change in work hardening rate then the stress strain curve is raised as shown in curve B. From the Holloman equation $\frac{\sigma_{T1}}{\sigma_{T2}} = \frac{\varepsilon_{T1}}{\varepsilon_{T2}}^{n}$ at each temperature and it can be deduced readily that n_{T1} and n_{T2} are not equal, the actual values being $n_{T1} = 0.369$ and $n_{T2} = 0.203$ as illustrated by the lower slope of graph E, Figure 32. Thus, increasing the flow stress whilst maintaining a constant work hardening rate has reduced the value of the strain hardening exponent.

Alternatively if at the lower temperature T3 the strain hardening exponent is unaltered from that at T1, the log σ_T v log ε_T plot will be as shown in curve F and the stress strain curve C derived from this obviously displays a higher true work hardening rate than before. It can be simply deduced that, since $\sigma_T = K\,\varepsilon_T^n$, the work hardening rate at T3 is greater by a factor K_{T3}/K_{T1} than that at T1 for any given strain.

Thus when temperature is decreased, with a resulting increase in flow stress and true work hardening rate, two opposing factors influence n and the variation of strain hardening exponent with temperature is a function of the relative change in work hardening rate and flow stress with temperature. Three different variation patterns with temperature might be predicted, the strain hardening exponent increasing, remaining constant or decreasing depending on whether the increase in work hardening rate with reducing deformation temperature outweighs, balances or is insufficient to overcome the effect of increasing flow stress.

The effect of variation of work hardening rate and flow stress with varying deformation temperature, for alloys obeying the Holloman relationship can be simply illustrated as follows.

$$\sigma_T = K\varepsilon_T^n, \quad d\sigma_T/d\varepsilon_T = nK\varepsilon_T^{(n-1)}$$

$$\therefore \frac{d\sigma_T/d\varepsilon_T}{\sigma_T} = \frac{n}{\varepsilon_T} \quad ---- \quad (25)$$

Thus again we see that n is dependent on the ratio of true work hardening rate, and flow stress at a given strain.

The effects of the relative variations of $d\sigma_T/d\varepsilon_T$ and σ_T with temperature on the value of n in the present study are illustrated in Figures 33(a) and 33(b) which show the variation of true work hardening rate and flow stress for alloy P9 over a range of deformation temperatures together with the variation of strain hardening exponent as measured from the log σ_T - log ε_T plots. The work hardening rates and flow stresses are those measured at $\varepsilon_T = 0.06$ and $\varepsilon_T = 0.15$. Also shown on these figures are computed values of n from the relationship $\frac{d\sigma_T/d\varepsilon_T}{\sigma_T} = \frac{n}{\varepsilon_T}$. It is immediately apparent that both methods of predicting strain hardening exponent, result in a maximum in the value of n at the same deformation temperature, namely that at which $\frac{d\sigma_T/d\varepsilon_T}{\sigma_T}$ decreases.

The maxima observed in the strain hardening exponent values with decreasing deformation temperature for alloys P6-P11 (Figs. 17-21) arise from the fact that, as indicated previously, the work hardening rate tends to increase linearly with decreasing temperature whereas the flow stress increases exponentially. Thus below a certain temperature the flow stress effect upon n becomes the dominant factor. It must be assumed that all BCC alloys displaying this flow stress/temperature dependence will behave in a similar fashion.

Therefore, although analysis of flow curves on the basis of Holloman's equation may provide adequate mathematical descriptions of flow curve shapes over a wide range of deformation temperatures as illustrated in this study (Figures 15a, 15b and 16) and others[3, 4, 5], the strain hardening exponent derived from the equation does not describe the variation of work hardening characteristics with temperature.

For a material which obeys the Holloman equation $\sigma_T = K\varepsilon_T^n$, it can be shown from theory (Appendix A) that the strain hardening exponent, n, can be equated to the plastic instability strain ε_{PI}, at which necking commences and this equivalence has been frequently quoted and utilised in the literature. This conclusion, however, cannot be applied directly to a material which displays double n behaviour.

This is illustrated in Figure 40, which shows the observed relationship between the plastic instability strain and the strain hardening exponent measured at various test temperatures on alloy P10. The values of $\mathcal{E}_{PI}$ and n are not identical, although they show the same trend with decreasing test temperature down to -105°C. The plastic instability strain is always less than the strain hardening exponent because double n behaviour is essentially an indication that the value of n is decreasing with increasing strain. As can be seen from Figure 40, it is only in the case of single n behaviour (at -196°C) that the n value is close to the observed $\mathcal{E}_{PI}$ in accordance with the Holloman equation.

5.5 The use of the Strain Hardening Exponent in Assessing Fracture Toughness.

In view of the above comments on the significance of n values it is appropriate to consider the results of previous investigations[36, 37, 40] which have suggested the use of the strain hardening exponent parameter as a means of assessing a materials fracture toughness.

Krafft[37] and Thomason[40] introduce n into their theories on the basis of its equivalence with the plastic instability strain, since it is proposed that crack extension will occur when this strain is attained at a small distance in advance of the crack tip. From the present results it would appear that the use of an n value here must lead to an overestimate of plastic instability strain and hence of K_{IC} if the material displays double n behaviour, particularly if an n value at a low strain (e.g. 3% in Krafft's work) is adopted.

Thomason's model discussed earlier (Chapter 2.3) results in equation (21) which can be rearranged thus

$$\frac{0.9\,K_{IC}^{\,2}}{4.62\,rE} = Y\,(\exp \mathcal{E}_{PI} - 1) \qquad (25)$$

for a material containing a volume fraction of cavity nucleating particles greater than .09, when Y is the yield stress. Neglecting variation in E with temperature, the data obtained in the present work suggest that both Y and $\mathcal{E}_{PI}$ increase with decreasing temperature below ambient and this would lead to an increasing K_{IC} value as temperature falls. This is of course contrary to experience and suggests that the effective crack tip radius in Thomason's model must decrease with temperature to explain experimental K_{IC} values.

Hahn and Rosenfield introduce the strain hardening exponent into their theory by postulating that increasing work hardening rate leads to an increase in plastic zone size (ℓ) at the crack tip and propose an empirical relationship, under plane strain conditions between n and plastic zone size $\ell = n^2$ where ℓ is measured in inches. In view of the comments above on the significance of n it would appear that some measure of true work hardening rate would be more appropriate than an n value to represent the effect of strain hardening on ℓ. Hahn and Rosenfield's relationship $K_{IC} = (\frac{2}{3}\,EY\,n^2\,\bar{\mathcal{E}}^*)^{\frac{1}{2}}$ again predicts an increasing K_{IC} value with decreasing temperature over appreciable temperature ranges for the alloys examined in the present work, which would be surprising.

Thus while the arguments presented regarding the effect of strain hardening on both plastic instability strain and plastic zone size are well founded the detailed models presented do not appear to explain the variation of fracture toughness over appreciable ranges of temperature.

5.6 True Work Hardening Rates

As indicated earlier, values of $d\sigma_T/d\varepsilon_T$ were determined for each alloy over the temperature range investigated, and a typical family of curves for alloy P 10 is shown in Figure 38. This shows a steady increase in true work hardening rate with decreasing deformation temperature down to -105°C. However at -196°C, for $\varepsilon_T = 0.10$ the work hardening rate is less than that at -105°C, and indeed for $\varepsilon_T = 0.06$, the work hardening rate is less than that at -60°C.

A much better indication of the behaviour of absolute work hardening rate as a function of temperature can be obtained from Figures 39(a - e) which show how work hardening rates vary with temperature for various values of true strain.

All the alloys analysed by this technique exhibited the same general behaviour. At each strain, the initial portion of the $d\sigma_T/d\varepsilon_T$ v T°C curve indicates a linear increase in work hardening rate with decreasing temperature. As the magnitude of the strain value is increased, within an alloy, the rate of increase of $d\sigma_T/d\varepsilon_T$ with increasing deformation temperature decreases. Alloys P6, P8, P9 and P10 exhibit deviations from this linear behaviour for tests carried out at -196°C, in that decreases in work hardening rate for a given strain occur below some critical strain value. For example, alloy P6 (Figure 39(a)) exhibits a linear dependence of work hardening rate on temperature from ambient to -196°C at a strain of 0.10 whilst for $\mathcal{E}_T = 0.06$, $d\sigma_T/d\varepsilon_T$ at -196°C is equivalent to that at -77°C.

Alloy P7 however, which yields continuously displaying no Lüders deformation yields an approximately linear increase in $d\sigma_T/d\varepsilon_T$ with decreasing deformation temperature at all strains considered (Figure 39(b)).

The Lüders strain region which occurs when materials yield discontinuously, is the region where yield is spread inhomogeneously through a material during deformation. During the present investigation, for alloys exhibiting discontinuous yielding, the extent of the Lüders strain region was found to increase markedly with decreasing deformation temperature. This effect for alloys P6, P8, P9 and P10 is illustrated in Figure 14. It is thought that the increase in Lüders strain with decreasing deformation temperature, may account for the work hardening behaviour of alloys P6, P8 and P10 at -196°C described earlier. This postulate is to some extent confirmed by the regular behaviour of alloy P7 which deforms homogeneously.

5.7. Comparison between Charpy Impact Data and Critical C.O D. Values

The toughness classification of alloys P6, P7, P8, P9, P10 and P11, on the basis of the C.O.D. tests performed during the present study can be empirically determined by examination of

Figures 26, 27 and 28. From these Figures one could say that at $20^{o}C$ the alloys could be ordered as P10, P9, P8, P11 (8μ), P11 (42μ), P6 and P7, in decreasing order of toughness.

Investigations have been made into the relationship between impact test temperatures, and those obtained from quasi-static toughness tests. As one might expect, the transition temperature obtained from Charpy impact tests is much ligher than that obtained from toughness tests, one of the main contributory factors being the strain rate differential.

Since no transition to a cleavage fracture mode was observed in the C. O. D. tests no direct comparison on a transition temperature basis is possible from the present results.

Comparisons have been made between C. O. D. and Charpy upper shelf energy. However, for a comparison to be realistic on an energy basis, C. O. D. values should be expressed in terms of an effective fracture energy. Since an empirical measure of energy to fracture can be obtained from the expression $\sigma_y \delta$, values of this parameter were calculated and compared with the appropriate upper shelf energy.

Considering only the alloys tested in the longitudinal mode, the ranking on a $\sigma_y \delta$ basis is unchanged from that given above, namely P10, P9, P8, P11 (8μ), P11(42μ), whereas the upper shelf energy ranking is P11 (42μ), P10, P9, P8 and P11 (8μ) in decreasing order of toughness. It would appear that the toughness ranking is similar with the notable exception of the coarse grained alloy P11, which for its low yield strength and small C. O. D. displayed an anomolously high upper shelf energy. Further investigation of the relationship between $\sigma_y\delta$ and upper shelf energy would appear to be fruitful.

5. 8. Crack Opening Displacement

The reproducibility of C. O. D. values has always been one of the major problems associated with General Yielding Fracture Mechanics. A good illustration of this difficulty can be obtained by reference to the First Report of the Crack Opening Displacement Application (CODA) Panel. Several laboratories carried out independent C. O. D. tests on specimens machined from the same material and selected at random. A very high degree of scatter in measured C. O. D. values was observed both between and within individual laboratories.

For example, tests carried out during the above mentioned programme, on Admiralty 'S' steel at -50°C, -80°C, -110°C and -140°C gave percentage scatter values of $^{+13}_{-8}$, $^{+75}_{-56}$, $^{+91}_{-75}$ and $^{+150}_{-56}$ respectively. These values of percentage scatter increase with decreasing test temperature, the reason being that the absolute value of C. O. D. decreased markedly with temperature, in this case from an average of 0.875 mm at -50°C down to 0.075 mm at -140°C, whilst the scatter obtained in measurement remained relatively constant at about ± 0.150 mm. These results were obtained using a clip gauge similar to that employed in the present study, and although their scatter values were rather high, the results were more consistent than those obtained in a parallel investigation using the paddle codmeter as the measuring device.

The results obtained in this investigation for average, critical C. O. D. values, and the absolute scatter about these average values, are presented in Table 8. As can be seen from this table, the measurement accuracy appears to be much greater in the present study than in that discussed above. A possible reason for this improvement in measurement accuracy is that the present values have been determined for the onset of slow stable crack propagation, or for fast fracture, whichever occurs first, whereas in the previous investigation maximum C. O. D. values were taken as the critical points where no previous fast fracture had occurred. The significance of maximum load C. O. D. is not at all clear, and there is a great deal of doubt about its practical value.

A primary conclusion of the present work is therefore that reproducible C. O. D. results can be obtained if initial crack extension is taken as the critical event.

A wide range of behaviour was observed during C. O. D. testing of the various alloys. Alloy P10 exhibited extensive slow crack growth even at test temperatures as low as -77°C, whereas alloy P7 showed no signs of slow crack growth at -30°C. Alloys P6, P8, P9 and P11 show behaviour in an intermediate range.

The lowest toughness was observed in alloys P6 and P7 which were tested in the transverse direction. The bainitic microstructure of alloy P7 will of course be a major factor in producing the low observed toughness, but investigations indicate that transverse toughness is, in general, lower than toughnesses obtained by testing the same material in the longitudinal mode. This lowering effect can be attributed to the difference in orientation of any inclusion, in the form of stringers, to the applied stress, when the transverse and longitudinal orientation are compared. Inclusion content and morphology, have been found to be a major controlling factor in the toughness of metals and alloys.

The effect of grain size was briefly investigated in tests carried out on alloy P11. As can be seen from Figure 28, the specimens having a grain size of 8.5μ exhibit a markedly better toughness than specimens with a grain size of 42μ. This is of course, the expected behaviour.

5.9. Scanning electron micrographs

Figures 31 (a-g) show some of the fracture characteristics of the materials investigated reflected in their scanning electron micrographs. Figures 31(a), (b), (d), (f) and (g) illustrate the fracture surfaces of alloys P8 (20°C, -32°C), P9(-60°C) and P10 (20°C, -77°C) respectively. In all these cases, a region typical of slow crack growth can be observed in the area between the tip of the fatigue crack and the flat cleavage area. These three regions are best illustrated in Figure 31(b)(Alloy P8, tested at -32 °C).

Figure 31(d) illustrates the occurrence of a very small region of slow crack growth at the tip of the fatigue crack in alloy P9 tested at -60°C. According to the 'change in potential' -displacement curve obtained for this test, slow crack growth initiated immediately prior to fracture. Measurement of the slow crack growth region in Figure 31(d) indicates that crack extension of 0.025 mm has occurred prior to fracture. It can be concluded therefore that crack extensions of the order of 0.025 mm may be detected with certainty by use of the potential drop technique.

Figures 31(c) and (e) illustrate two cases where no slow crack growth preceded fracture. Figure 31(e) shows the fracture surface of alloy P9 tested at -77°C, and clearly indicates the absence of any signs of dimple fracture. Figure 31(c), however, showing the fracture surface of alloy P8 tested at -77°C, indicates the occurrence of slightly different fracture behaviour. The fracture surface consists of two distinct regions, one being flat, and the other showing dimple features pointing to the occurrence of a mixed fracture. The cleavage regions in this micrograph are typified by the presence of parallel striations, which may well be an indication that the cleavage areas are centred around pearlitic areas, whilst the regions of ductile fracture might be associated with ferrite.

5.10 Effect of Tensile Properties on Toughness

Figures 26, 27 and 28 illustrate that material toughness, as measured by critical C. O. D., decreases with decreasing temperature. As has already been demonstrated, reducing test temperature has a marked effect on both material flow stress and work hardening characteristics. Flow stress increases with decreasing deformation temperature, whilst the true work hardening rate also increases with decreasing deformation temperature. The flow stress and work hardening characteristics of materials will both have an influence on critical C. O. D., and it would seem pertinent at this stage to postulate the effect of variation of flow stress and work hardening characteristics on C. O. D.

An assessment of the effect of differing work hardening rates on C. O. D. is very difficult to obtain experimentally. Any change in work hardening rate automatically invokes a change in flow stress, and any relationship between work hardening rate and C. O. D. would be clouded by the change in flow stress. It is possible however to postulate the effect that differences in work hardening characteristics might tend to invoke in the plastic zone at a crack tip.

Consider two different materials with equivalent yield stresses, but with different work hardening characteristics. When yielding occurs at the crack tip the material within the plastic zone work hardens and therefore yielding spreads to the adjacent regions which have not work hardened. Hence one would expect a larger plastic zone size in the material exhibiting the higher work hardening rate. Since a larger plastic zone size leads to an increase in C. O. D. one would also expect a higher C. O. D. in the material which work hardened more rapidly.

The effect of flow stress variation should be more easily analysed experimentally than variation of work hardening rate. The effect can be considered by comparing materials which exhibit similar work hardening characteristics, but whose flow stresses are different. The effect is best described in terms of crack tip plastic envelope size. At constant work hardening rate, one would predict a larger plastic zone envelope in material of low flow stress than in a higher flow stress material, and hence a smaller critical C. O. D. in the higher flow stress material.

A further consideration is that changes in both flow stress and work hardening rate will lead to alteration of the instability strain. Increasing work hardening rate increases the instability strain whilst it would be predicted that increasing flow stress would reduce the strain at instability. Since C. O. D. should increase with instability strain, two opposing effects are operative when work hardening rate and flow stress increase simultaneously.

If an attempt is made to apply the above considerations to the results obtained in the present study, it is immediately apparent that it is impossible to compare materials of the same flow stress over a range of strain, but with different work hardening characteristics, since the first requirement implies that the work hardening characteristics are similar. A comparison can, however, be made between materials with similar work hardening rates but different flow stresses. Unfortunately other variables will affect the fracture toughness so that the comparison may not be direct as indicated in the case considered below.

Figure 41 shows the variation of true work hardening rate with strain for alloys P10 and P8 at temperatures of +20^{o}C and

-10°C respectively. The work hardening characteristics of alloy P10 (at 20°C) and alloy P8 (at-10°C) can be considered as identical. Figure 42 shows the flow curves for alloys P10 and P8 at 20°C and -10°C respectively, and it can be seen that alloy P10 has a higher flow stress at all strains than alloy P8, the difference in flow stress being constant at 9 Kg. mm^{-2}.

From the preceding argument one would expect alloy P10 to have a lower critical C. O. D. than alloy P8, but comparison of the critical C. O. D. values reveals that; δ_i (P8, -10°C) = 0. 280mm. δ_i (P10, 20°C) = 0. 510mm. This result may well be attributed to the fact that alloys P8 and P10 are different in two significant respects which affect fracture behaviour.

The non metallic inclusion content has a marked effect on fracture susceptibility. Non metallic inclusions act as sites for void nucleation which results from the debonding of the non metallic inclusion - matrix interface. Increasing the non metallic inclusion level in a steel produces more potential sites for void nucleation and hence results in a decrease in toughness. Table 5 presents a breakdown of the non metallic inclusion contents of each of the alloys tested, and comparison of alloys P8 and P10 reveals that P8 has a non metallic inclusion content three times as large as that in alloy P10.

Grain size also has a marked effect on toughness properties, increasing grain size promoting failure at lower C. O. D. values, as illustrated by the behaviour of alloy P11 (Figure 28), and consideration of the grain sizes of alloys P8 and P10 (Table 2) indicates that P8 has a grain size of 25μ whilst P10 has a grain size of 8μ .

Thus two factors which have a major influence on fracture behaviour are acting to reduce the toughness of alloy P8 compared to alloy P10. Before any realistic assessment of the effects of varying flow stress and work hardening rates on toughness can be made, it is imperative that the important factors controlling fracture behaviour do not exhibit significant variation between the alloys considered.

Consideration of tables 2 and 5 indicates that alloy P11 (8μ) has a grain size very similar to that of alloy P10 (8.5μ cf 8μ) and that the non metallic inclusion contents of the two alloys are similar.

Although insufficient tensile tests were carried out on alloy P11 (8μ) (Appendix C) to permit as accurate determinations of $d\sigma_T/d\varepsilon_T$ values to be made as for the other alloys considered, the $d\sigma_T/d\varepsilon_T$ values were measured as described previously. These results are shown in Figure 43 which is a plot of $d\sigma_T/d\varepsilon_T$ v ε_T for the test temperatures considered. The $d\sigma_T/d\varepsilon_T$ v ε_T curves for alloy P10 over a range of temperatures are also shown in Figure 43 for comparison. It can be seen that work hardening rates for the two alloys are closest for deformation temperatures $-77^{\circ}C$ (P11, 8μ) and $20^{\circ}C$ (P10).

Comparison of the flow curves of alloys P10 and P11 at $20^{\circ}C$ and $-77^{\circ}C$ respectively (Figure 44) indicates that at all strains, the flow stress for alloy P11 is significantly higher than that for alloy P10.

On the basis of the previous argument, since the work hardening rates are considered to be equal, then one would expect the higher flow stress material to have a lower critical C. O. D. Comparison of the critical C. O. D. values for alloy P10 (+20°C) and alloy P11, 8μ (-77°C) indicates that the critical C. O. D. values are 0.510mm and 0.180mm respectively, confirming the above prediction.

This is the only instance, in the present study, where direct comparison of results is possible, because of the restrictions already mentioned with respect to grain size and non metallic inclusion content.

Figure 45 shows a plot of critical crack opening displacement against flow stress (at 6% $\mathcal{E}_T$) for alloys P6, P7, P8, P9 and P10 at temperatures of 20°C, -30°C and -77°C. The curve in Figure 45 is drawn through the lower limit of observed crack growth as a failure mechanism, where the slow crack growth region can be identified as being wholly ductile.

In the lower flow stress region it will be noted that two points lie obviously below this line, one each for alloy P8 and P9 tested at -77°C. The upper of these two points (P8) as discussed earlier in Section 5.7 exhibited a fracture surface of mixed morphology, showing signs of both ductile and cleavage fracture. The lower point however (P9) corresponds to fracture occurring in a pure cleavage mode. In neither of these cases was any sign of slow crack growth prior to failure detected.

It would seem likely that a second boundary line could be drawn, which might indicate the limit of mixed node failure. The dotted line drawn in Figure 45 indicates the possible form of the final diagram. In region (1) failure occurs as a result of extensive slow crack growth, whereas in region (3) failure occurs in a cleavage mode. Region (2) corresponds to the area where mixed mode fracture would occur.

The main conclusion to be drawn from examination of Figure 45 is that the C. O. D. for initiation of slow crack growth decreases with increasing flow stress. When slow crack growth is the operative failure mechanism, the actual value of C. O. D. depends on the complex relationships already outlined between flow stress, work hardening rate and structural variables which affect the fracture process.

CHAPTER 6

CONCLUSIONS

1. The stress-strain characteristics of the alloys investigated obeyed the Holloman relationship but mainly displayed "double n" behaviour. As deformation temperature is reduced there is a tendency to single n behaviour. This illustrates the tendency of transition strain to increase with decreasing temperature, although the scatter in this parameter makes the concept of a definite transition strain questionable. The Crussard analysis offers no advantages in the measurement of transition strain, and is in fact incapable of predicting n values accurately.

Variation of n with temperature in all cases showed a maximum in n at some temperature below ambient.

2. Investigation of true work hardening rates indicates that at high strains, as deformation temperature decreases, a linear increase in true work hardening rate occurs from 20°C to -196°C.

At lower strains, alloys which yield discontinuously show an anomalously low work hardening rate at low deformation temperatures. It is suggested that the increase in Lüders strain which occurs with decreasing deformation temperature has a major influence in producing the lowering in true work hardening rates at low strains in these alloys.

3. The variation of n with temperature does not reflect the change in true work hardening rate, since n depends on the relative change in flow stress and $d\sigma_T/d\mathcal{E}_T$. Thus in B. C. C. alloys which show an exponential increase in flow stress with decreasing temperature,

n must decrease below a certain temperature, despite a continued increase in $d\sigma_T/d\varepsilon_T$.

4. The use of n in fracture toughness relationships as a measure of either plastic instability strain or work hardening rate and hence plastic zone size is of doubtful validity.

5. Reproducible values of critical crack opening displacement over a range of test temperatures can be obtained, using the crack opening displacement to crack initiation as the critical parameter.

6. A qualitative correlation may exist between Charpy upper-shelf energy and a fracture energy derived from C. O. D. measurement.

7. The effect of increasing flow stress at constant work hardening rate is to reduce the value of critical C. O. D. , provided that other parameters affecting the fracture process and comparable. The effect of varying work hardening rate at a given flow stress is difficult to analyse experimentally, but increasing $d\sigma_T/d\varepsilon_T$ should lead to an increase in material toughness.

REFERENCES

1. Hollomon, J.H., Trans.A.I.M.E., 1945, 162, p.268.
2. Ludwik, P., Elemente Der Technologischen Mechanik, p.32, Julius Springer, Berlin, 1909.
3. Morrison, W.B., Trans.A.S.M., 1966, 59, p.824.
4. Bergström, Y., Aronsson, B., Met.Trans., 1970, 1, p.1029.
5. Morrison, W.B., Met.Trans., 1971, 2, p.331.
6. Monteiro, S.N., Reed-Hill R.E., Met.Trans., 1971, 2, p.2947.
7. Crussard, C., Rev.De Met., 1953, 50, p.589.
8. Keh, A.S., Weissmann, S., "Electron Microscopy and Strength of Crystals": Editors: G. Thomas, J. Washburn p.231
9. Christ, B.W., Smith, G.V., ACTA Met., 1967, 15, p.809.
10. Li, J.C. "Direct Observation of Imperfections in Crystals" Editors: J.B. Newkirk, J.H. Wernick. Interscience-Wiley (New York), 1962, p.234.
11. Langstone, P.F., I.S.I. Publication 120, 1970, p.155.
12. Inglis, C.E., Trans. Inst. Naval Architects, 1913, 60, p.219
13. Griffith, A.A. Philosophical Trans. Royal Society (London), Series A, 1920, 221, p.163.
14. Irwin G.R., Journal Applied Mechanics, 1957, 24, p.361
15. Westergaard, H.M. Journal of Applied Mechanics, 1939, 61, p. A-49.
16. Paris, P.C., SIH, G.C. A.S.T.M. Special Technical Publication No. 381, 1964.
17. Knott, J.F. Fundamentals of Fracture Mechanics, Publisher Butterworth, p.227.
18. British Standards Institution: Draft for Development, Methods for Plane Strain Fracture Toughness Testing Document No. 70/28665.
19. A.S.T.M. Special Technical Publication No. 410, 1969.
20. A.S.T.M. Special Technical Publication No. 381, 1964.
21. Iron and Steel Institute Report No. 121, 1963.
22. Cottrell, A.H. Iron and Steel Institute Special Report No. 69, 1961, p.281
23. Wells, A.A. Crack Propagation Symposium Proceedings, Cranfield College of Aeronautics, 1961, 1, p.210

24. Nichols, R.W., Burdekin, F.M., Cowan, A., Elliot, D., Ingham, T., Paper F, Proceedings of the Symposium on Fracture Toughness Concepts for Weldable Structural Steel. Risley, 1969, Editor: M.O. Dobson.

25. Fearnehough, G.D., Watkins, B. The International Journal of Fracture Mechanics, 1968, 4, p.233.

26. Wells A.A. British Welding Journal, 1963, 10, p.855.

27. Bilby, B.A., Cottrell, A.H., Swinden, K.H. Proc. Royal Soc., 1963, A272, p.304.

28. Burdekin, F.M., Stone, D.E.W., Journal Strain Analysis, 1966, 1, p.145.

29. Dugdale, D.S., Journal of Mechanics and Physics of Solids, 1960, 8 , p.100.

30. Cowan, A., Kirby, N., Paper D, Proceedings of the Symposium on Fracture Toughness Concepts for Weldable Structural Steels, Risley, 1969, Editor M.O. Dobson.

31. Parry, G.W. and Mills, R.G., Journal Strain Analysis, 1968, 3, p.159.

32. Folias, E.S.; International Journal Fracture Mechanics, 1965, 1, p.104.

33. Rice, J.R., Journal of Applied Mechanics, 1968, 90, p.379.

34. Rice J.R., Fracture, Edited by H. Liebonitz Academic Press N.Y. 1968, p.191

35. Begley J.A., Landes, J.D. A.S.T.M. Special Technical Publication No. 514 (1972).

36. Hahn, G., Rosenfield, A., Applications Related Phenomena in Titanium Alloys A.S.T.M. Special Technical Publication No. 432, 1968, p.5.

37. Krafft, J., Applied Materials Research, 1964, 3, p.1964.

38. Irwin, G.R. Journal of Basic Engineering, 1960, 82 , p.417

39. McClintock, F.A., Journal of Applied Mechanics, 1968, 90, p.363

40. Thomason, P.F., Int. Journal of Fracture Mechanics, 1971, 7 , p.409.

41. Thomason, P.F., Journal of the Institute of Metals, 1968, 96, p.360.

42. Hill, R., Selected Government Research Reports, No.L6, Strength and Testing of Materials - Part 1., H.M.S.O., 1952.

43. Smith, R.F., Knott, J.F. Practical Application of Fracture Mechanics to Pressure Vessel Technology. Institute of Mechanical Engineers 1971, p.65.

44. Johnson, H.H., Materials Research and Standards, 1965, 5, p.442.

45. Lowes, J.M., Fearnehough G.D., Engineering Fracture Mechanics, 1971, 3, p.103.

46. British Standard Institution: D.D.19, 1972. Draft for Development of Crack Opening Displacement Testing.

47. Egan, G.R., Metal Construction and British Welding Journal. 1973, 5, p.214.

48. Gray, T.G.F., International Journal of Fracture Mechanics, 1972, 8, p.277.

49. Ingham T., Rao, S. Jerkontorets Annaler, 1969, 153, p.327.

50. Alexander, J.M. Komoloy, T.J. Mechanics and Physics of Solids, 1962, 10, p.265.

51. Ingham, T., Egan, G.R., Elliot, D., Harriston, T.C., Practical Application of Fracture Mechanics to Pressure Vessel Technology, Institute of Mechanical Engineers, 1971, p.200.

52. Frederick, G., Salkin, R.V., Practical Application of Fracture Mechanics to Pressure Vessel Technology. Institute of Mechanical Engineers, 1971, p.136.

53. Knott, J.F. Cottrell, A.H., J.I.S.I. 1963, 201, p.249

54. Ostensson, B. Engineering Fracture Mechanics, 1972, 4, p.443.

55. Fearnehough G.D., Lees, G.M., Lowes, J.M., Weiner, R.T., Practical Application of Fracture Mechanics to Pressure Vessel Technology. Institution of Mechanical Engineers, 1971, p.119.

56. Ritchie, R.O., Garrett, G.G., Knott, J.F., International Journal of Fracture Mechanics, 1971, 7, p.462-467.

57. Elliot, D., Walker, E.F., May, M.J., Practical Application of Fracture Mechanics to Pressure Vessel Technology. Institution of Mechanical Engineers, 1971, p.217.

58. Ramani, S.V., Rodrigues, P.: Scripta Metallurgica, 1970, 4, p.755.

APPENDIX A

DEFINITIONS OF TRUE STRESS AND TRUE STRAIN

SYMBOLS

P = FORCE

A_o = ORIGINAL CROSS SECTIONAL AREA

A_1 = INSTANTANEOUS CROSS SECTIONAL AREA

L_o = INITIAL GAUGE LENGTH

L_1 = INSTANTANEOUS GAUGE LENGTH

σ = NOMINAL STRESS = P/Ao

σ_T = TRUE STRESS

ε_E = NOMINAL STRAIN = $L - Lo/_{Lo}$

ε_T = TRUE PLASTIC STRAIN

n = STRAIN HARDENING EXPONENT

K = STRENGTH COEFFICIENT

TRUE STRESS σ_T

True stress is defined as applied force P divided by the instantaneous cross sectional area A_1

$$\sigma_T = \frac{P}{A_1} \qquad (A1)$$

TRUE PLASTIC STRAIN ε_T

True plastic strain is defined as follows.

$$\varepsilon_T = \frac{L_1 - Lo}{Lo} + \frac{L_2 - L_1}{L_1} + \frac{L_3 - L_2}{L_2} + \ldots\ldots\ldots \frac{L_n - L_{n-1}}{L_{n-1}}$$

$$= \int_{Lo}^{L_1} \frac{dL}{L} = \log_e \frac{L_n}{Lo}$$

$\therefore$ True plastic strain when the instantaneous gauge length is L_1 may be written.

$$_T = \log_e \frac{L_1}{L_o} \qquad (A2)$$

APPENDIX A (CONT.)

HOLLOMONS' equation relating true stress and true strain is,

$$\sigma_T = K \varepsilon_T^{n}$$

$$\frac{d\,\sigma_T}{d\,\varepsilon_T} = n K \varepsilon_T^{(n-1)}$$

$$= n \frac{\sigma_T}{\varepsilon_T} \tag{A3}$$

$$P = \sigma_T \, A_1$$

$$\therefore \frac{dP}{d\,\varepsilon_T} = A_1 \frac{d\,\sigma_T}{d\,\varepsilon_T} + \sigma_T \frac{d\,A_1}{d\,\varepsilon_T} \tag{A4}$$

<u>At the U. T. S.</u> $\frac{dP}{d\,\varepsilon_T} = 0$

$$\therefore A_1 \frac{d\,\sigma_T}{d\,\varepsilon_T} = - \sigma_T \frac{dA_1}{d\,\varepsilon_T} \tag{A5}$$

$\varepsilon_T = \mathrm{LOG}_E \left(\frac{Ll}{Lo}\right)$ $\therefore$ ASSUMING CONSTANCY OF VOLUME UP TO THE U. T. S., THEN

$$A_o L_o = A_1 L_1$$

$$\therefore \varepsilon_T = \mathrm{LOG}_E \left(\frac{Ll}{Lo}\right) = \mathrm{LOG}_E \left(\frac{Ao}{A_1}\right)$$

$$\therefore A_1 = A_o \, \mathrm{EXP}\,(-\varepsilon_T)$$

$$\therefore \frac{dA_1}{d\,\varepsilon_T} = - A_o \, \mathrm{EXP}\,(-\varepsilon_T)$$

$$= -A_1 \tag{A6}$$

SUBSTITUTING INTO (A5) ONE OBTAINS

$$\frac{d\,\sigma_T}{d\,\varepsilon_T} = \sigma_T \tag{A7}$$

CONSIDERATION OF EQUATIONS (A3) AND (A7) REVEALS THAT <u>AT THE U. T. S.</u> FOR A MATERIAL OBEYING HOLLOMON'S RELATIONSHIP, $\varepsilon_T = n$.

APPENDIX B :

DERIVATION OF RELATIONSHIP BETWEEN SURFACE AND CRACK TIP DISPLACEMENT

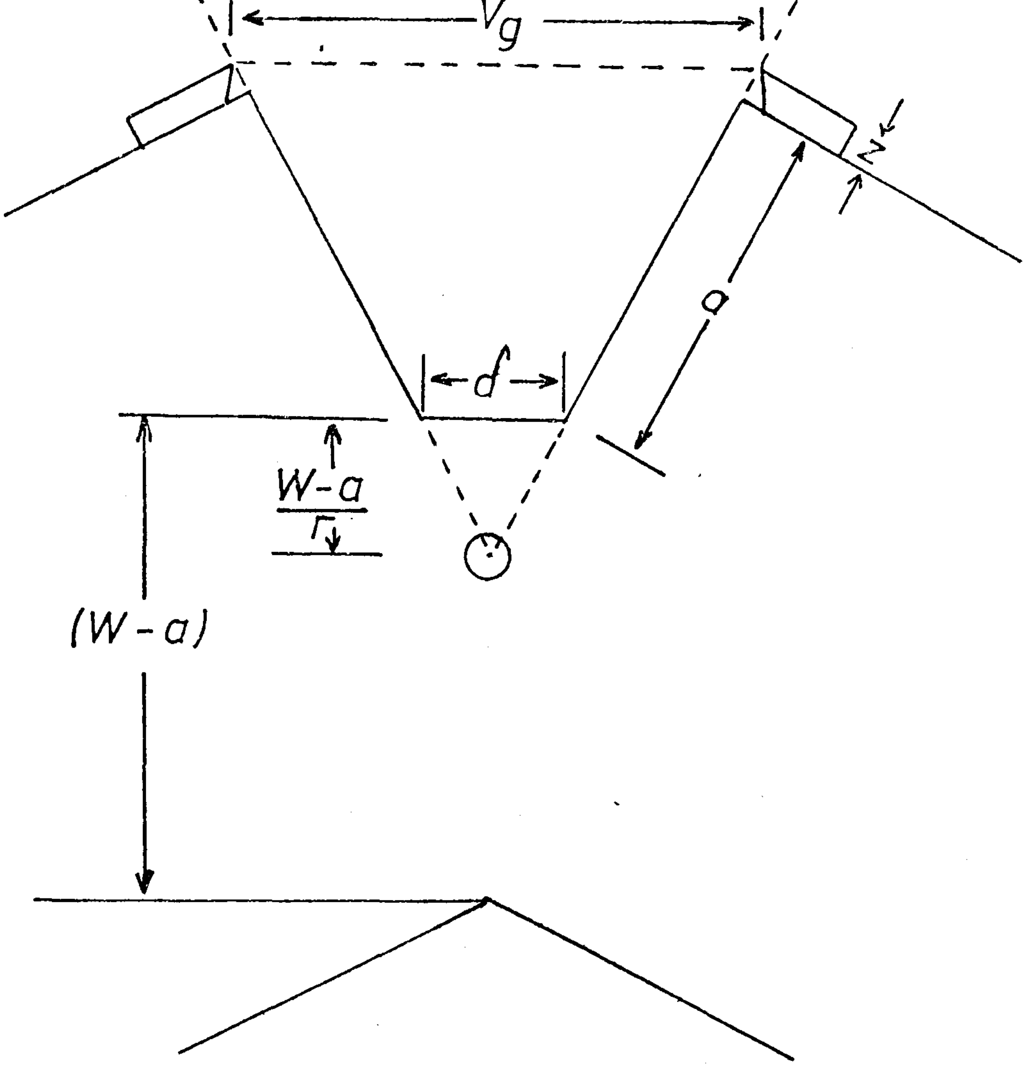

Vg ; Knife Edge opening

δ ; Crack Tip Opening

a ; Crack Length
W ; Specimen width
Z ; Knife Edge thickness

⊙ ; Assumed centre of rotation

$\frac{1}{r}$ (W-a) ; Distance from crack tip of the assumed centre of rotation

utilising the theory of similar triangles ;

$$\frac{V_g}{\delta} = \frac{a + Z + \frac{1}{r}(W-a)}{\frac{1}{r}(W-a)}$$

$$\therefore \frac{V_g}{\delta} = \frac{a + Z}{\frac{1}{r}(W-a)} + 1$$

APPENDIX C

ALLOY P6

SPECIMEN NUMBER	TEST TEMP ^{o}C	n_A	n_B	n_C	K_A Kg.mm^{-2}	K_B Kg.mm^{-2}	K_C Kg.mm^{-2}
1	20		0.215	0.169		43.1	47.2
2 e	20 e		0.230e	0.181e		41.8e	45.5e
3	20		0.237	0.185		40.7	44.8
4	-10		0.237	0.202		42.1	44.6
5	-10		0.229	0.179		42.3	46.9
6	-10		0.244	0.204		41.7	44.5
7	-30		0.274	0.218		40.6	44.2
8	-30		0.261	0.203		41.2	45.5
9	-30		0.253	0.193		41.3	46.2
10	-50		0.256	0.229		42.2	44.1
11	-50		0.250	0.210		42.9	46.3
12	-50		0.248	0.204		44.0	47.3
13	-77		0.251	0.204		44.9	49.3
14	-77		0.258	0.206		44.1	48.8
15	-196	0.188			70.3		
16	-196	0.174			72.5		
17	-196	0.179			72.0		
18	-196	0.172			72.6		

(CONT.)

APPENDIX C

ALLOY P7

SPECIMEN NUMBER	TEST TEMP ^{o}C	n_A	n_B	n_C	K_A $Kg.mm^{-2}$	K_B $Kg.mm^{-2}$	K_C $Kg.mm^{-2}$
1	20	0.109			96.2		
2	20	0.103			91.7		
3 e	20 e	0.106e			94.4e		
17	0	0.112			98.7		
18	0	0.112			98.5		
10	-30	0.124			95.2		
11	-30	0.135			100.1		
12	-30	0.135			96.3		
16	-30	0.116			103.5		
7	-50	0.124			101.8		
8	-50	0.122			105.0		
9	-50	0.127			105.0		
4	-77	0.125			105.9		
5	-77	0.124			104.1		
6	-77	0.124			104.3		
19	-110	0.115			115.0		
13	-196	0.108			124.7		
15	-196	0.108			122.4		

(CONT.)

APPENDIX C

ALLOY P8

SPECIMEN NUMBER	TEST TEMP ^{o}C	n_A	n_B	n_C	K_A Kg mm^{-2}	K_B Kg mm^{-2}	K_C Kg mm^{-2}
9 e	20 e		0.313 e	0.228 e		22.4 e	26.4 e
10	20		0.318	0.237		22.3	25.8
12	20		0.309	0.228		22.9	26.7
18	-10		0.301	0.221		24.3	28.9
19	-10		0.318	0.243		23.9	27.5
20	-10		0.306	0.253		23.5	26.1
21	-10		0.312	0.236		23.4	27.2
22	-30		0.327	0.257		24.4	27.7
23	-30		0.316	0.241		24.6	28.7
24	-30		0.315	0.257		23.9	26.6
25	-30		0.309	0.231		24.2	28.5
26	-45		0.321	0.252		24.6	27.6
27	-45		0.353	0.245		23.2	28.5
28	-45		0.327	0.251		24.3	28.1
29	-45		0.324	0.251		24.6	28.5
30	-60		0.303	0.231		26.5	30.8
31	-60		0.325	0.250		24.9	29.0
32	-60		0.314	0.252		25.9	29.4
33	-60		0.313	0.231		25.5	30.6
13	-77		0.290	0.234		27.3	31.2
14	-77		0.298	0.263		26.9	28.9
15	-77		0.302	0.256		27.4	30.1
16	-77		0.325	0.267		26.2	29.2
17	-77		0.307	0.251		26.5	30.0
34	-196	0.148			66.9		
35	-196	0.147			66.5		
36	-196	0.145			66.7		

(CONT.)

APPENDIX C

ALLOY P9

SPECIMEN NUMBER	TEST TEMP °C	n_A	n_B	n_C	K_A $Kg.mm^{-2}$	K_B $Kg.mm^{-2}$	K_C $Kg.mm^{-2}$
2	20		0.323	0.234		20.9	24.6
3	20		0.319	0.238		21.2	24.3
4 e	20 e		0.312e	0.235e		20.7e	24.1e
8	0		0.326	0.245		21.3	24.6
9	0		0.318	0.234		21.0	24.2
10	0		0.317	0.233		21.1	25.1
11	-15		0.328	0.242		21.1	24.1
12	-15		0.327	0.239		21.4	24.8
13	-15		0.322	0.240		21.2	24.6
14	-30		0.329	0.243		21.6	25.3
15	-30		0.356	0.261		21.4	25.0
16	-30		0.328	0.237		21.7	24.8
17	-45		0.328	0.247		21.9	25.8
18	-45		0.328	0.243		22.4	25.1
19	-45		0.326	0.248		22.3	25.3
20	-60		0.318	0.235		23.0	26.1
21	-60		0.321	0.260		23.4	26.8
22	-60		0.322	0.249		23.7	27.3
5	-77		0.304	0.243		25.6	29.8
6	-77		0.302	0.245		25.8	30.1
23	-85		0.294	0.242		26.6	30.8
24	-95		0.268	0.243		29.1	33.9
25	-130	0.205			42.3		
26	-130	0.203			43.1		
27	-138	0.201			43.2		

(CONTD.)

APPENDIX C

ALLOY P10

SPECIMEN NUMBER	TEST TEMP °C	n_A	n_B	n_C	K_A Kg mm^{-2}	K_B Kg mm^{-2}	K_C Kg mm^{-2}
1	20		0.263	0.191		32.0	36.7
2	20		0.250	0.188		32.5	37.0
3	20		0.255	0.207		32.1	35.2
4	20		0.261	0.203		31.3	35.1
5e	20e		0.255e	0.196e		32.0e	36.0e
43	20		0.247	0.191			
11	0		0.257	0.197		32.8	37.0
12	0		0.248	0.185		33.4	38.1
13	0		0.258	0.200		32.7	36.7
14	0		0.242	0.184		33.6	38.2
15	0		0.246	0.203		33.6	36.7
16	-15		0.250	0.192		33.1	37.7
17	-15		0.260	0.195		32.5	37.5
18	-15						
19	-15		0.267	0.201		31.4	36.4
20	-15						
21	-30						
22	-30		0.266	0.197		33.8	38.9
23	-30		0.284	0.212		32.2	36.9
24	-30		0.270	0.202		32.8	37.8
25	-30		0.250	0.177		33.9	40.0
26	-45		0.268	0.183		33.3	40.3
27	-45		0.259	0.196		34.7	39.7
28	-45		0.286	0.215		32.2	37.3
29	-45		0.269	0.196		33.6	39.2
30	-45		0.273	0.209		33.9	38.6

(CONT.)

APPENDIX C

ALLOY P10 (CONT.)

SPECIMEN NUMBER	TEST TEMP °C	n_A	n_B	n_C	K_A $Kg.mm^{-2}$	K_B $Kg.mm^{-2}$	K_C $Kg.mm^{-2}$
31	- 60		0.264	0.195		34.9	40.6
32	- 60		0.274	0.218		34.3	38.5
33	- 60		0.284	0.208		33.0	39.0
34	- 60						
35	- 60		0.264	0.196		34.1	40.1
6	- 77		0.280	0.230		34.3	38.1
7	- 77		0.293	0.219		33.3	39.2
8	- 77		0.288	0.231		33.9	38.0
9	- 77		0.287	0.218		34.5	39.7
10	- 77		0.291	0.217		34.2	40.0
41	- 90		0.289	0.238		34.6	38.4
42	- 90		0.292	0.228		33.7	38.4
39	-105		0.292	0.216		34.9	41.1
40	-105		0.294	0.228		34.4	39.7
36	-196	0.162			68.2		
37	-196	0.162			67.6		
38	-196	0.165			66.7		

(CONT.)

APPENDIX C

ALLOY P11 (8μ)

SPECIMEN NUMBER	TEST TEMPERATURE ^{o}C	n_A	n_B	n_C	K_A $Kgmm^{-2}$	K_B $Kgmm^{-2}$	K_C $Kgmm^{-2}$
1	20		0.194	0.157		37.16	40.01
2	20		0.213	0.163		36.29	39.49
3	- 77	0.203			40.57		
4	- 30	0.206			37.92		

ALLOY P11 (42μ)

SPECIMEN NUMBER	TEST TEMPERATURE ^{o}C	n_A	n_B	n_C	K_A $Kgmm^{-2}$	K_B $Kgmm^{-2}$	K_C $Kgmm^{-2}$
1	20		0.272	0.225		24.1	28.03
2	20		0.278	0.208		25.1	28.99
3	-77		0.285	0.251		28.31	30.37
4	-30		0.301	0.240		25.75	29.12

APPENDIX D

ALLOY P6

SPECIMEN NUMBER	CRACK LENGTH, a	TEST TEMP.	SLOW CRACK GROWTH	δ_i
1	9.38 mm	20°C	✓	0.127 mm
2	8.86 mm	20°C	✓	0.138 mm
3	8.72 mm	20°C	✓	0.137 mm
4	9.52 mm	20°C	✓	0.0907 mm
5	10.38 mm	-30°C	✓	0.0749 mm
6	9.54 mm	-30°C	✓	0.1089 mm
7	9.20 mm	-50°C		0.0272 mm
8	8.84 mm	-50°C		0.0839 mm
9	9.46 mm	-50°C		0.0918 mm
10	9.075 mm	-77°C		0.120 mm
11	9.80 mm	-77°C		0.105 mm
12	9.275 mm	-77°C		0.102 mm
13	9.275 mm	-196°C		0.271 mm
14	8.80 mm	-196°C		0.0300 mm

ALLOY P7

SPECIMEN NUMBER	CRACK LENGTH, a	TEST TEMP.	SLOW CRACK GROWTH	δ_i
1	9.075 mm	20°C	✓	0.0926 mm
2	9.075 mm	20°C	✓	0.0793 mm
3	9.325 mm	20°C	✓	0.0718 mm
4	9.300 mm	-30°C		0.0466 mm
5	9.175 mm	-30°C		0.0616 mm
6	9.325 mm	-30°C		0.0437 mm
7	9.575 mm	-50°C		0.0524 mm
8	8.975 mm	-50°C		0.0557 mm
11	9.175 mm	-50°C		0.0492 mm
9	9.250 mm	-77°C		0.0377 mm
10	9.400 mm	-77°C		0.0350 mm
12	9.075 mm	-196°C		0.0226 mm
13	9.200 mm	-196°C		0.0255 mm

(CONT.)

APPENDIX D

ALLOY P8

SPECIMEN NUMBER	CRACK LENGTH, a m.m	TEST TEMP °C	SLOW CRACK GROWTH	δ_i m.m.
22	9.466	20	✓	0.379
4	8.992	20	✓	0.383
21	9.000	0	✓	0.334
8	9.779	0	✓	0.2509
16	9.068	-30	✓	0.2179
5	9.229	-30	✓	0.2818
2	9.060	-30	✓	0.323
6	9.042	-30	✓	0.259
15	9.000	-45	✓	0.185
3	9.051	-45		
7	9.356	-45	✓	0.276
9	9.269	-45	✓	0.185
12	9.254	-60		0.251
13	9.008	-60		0.289
14	8.687	-60		0.255
10	10.736	-77		0.120
11	9.000	-77		0.126

(CONT.)

APPENDIX D

ALLOY P9

SPECIMEN NUMBER	CRACK LENGTH, a m.m.	TEST TEMP °C	SLOW CRACK GROWTH	δ_i m.m
2	9.305	20	✓	0.471
4	9.364	20	✓	0.446
25	9.212	20	✓	0.563
26	9.804	20	✓	0.489
34	9.220	0	✓	0.392
35	9.403	0	✓	0.425
11	9.178	-30	✓	0.301
16	9.313	-30	✓	0.365
22	9.652	-30	✓	0.292
X	9.711	-30	✓	0.260
9	9.322	-45	✓	0.290
20	9.364	-45	✓	0.227
36	8.754	-45	✓	0.232
13	9.356	-60		0.194
14	9.432	-60		0.148
21	9.601	-60	✓	0.241
1	9.536	-77		0.080
12	9.872	-77		0.097
23	9.025	-77		0.070

(CONT.)

APPENDIX D

ALLOY P 1 0

SPECIMEN NUMBER	CRACK LENGTH a. m. m.	TEST TEMP. °C	SLOW CRACK GROWTH	δ_i m. m.
11	10.084	20	✓	0.510
22	9.423	0	✓	0.504
18	9.957	0	✓	0.498
16	0.567	-30	✓	0.526
13	9.482	-30	✓	0.498
17	9.025	-45	✓	0.369
14	9.423	-45	✓	0.319
21	9.313	-45	✓	0.338
15	9.415	-60	✓	0.341
20	9.406	-60	✓	0.257
19	9.262	-77	✓	0.314
10	9.023	-77	✓	0.231

ALLOY P 11

SPECIMEN NUMBER	CRACK LENGTH a. m. m.	TEST TEMP. °C	SLOW CRACK GROWTH	δ i. m. m.	
9	8.966	20	✓	0.308	8μ
3	9.296	20	✓	0.310	
1	9.525	20	✓	0.333	
7	9.563	-30	✓	0.238	
11	10.046	-30	✓	0.315	
6	8.915	-30	✓	0.195	
5	9.423	-77	✓	0.184	
4	8.941	-77	✓	0.175	
16	8.915	20	✓	0.210	42μ
21	9.220	20	✓	0.215	
13	9.226	20	✓	0.239	
19	9.093	-30	✓	0.190	
14	9.136	-30	✓	0.193	
20	9.195	-77		0.127	

ALLOY	C	Si	S	P	Mn	Ni	Cr	Mo	Sn	Al	Cu	HEAT TREATMENT	GRAIN SIZE
P1	0.22	0.01	0.004	0.005	0.02	0.01	0.01	0.01	0.01	0.023	0.03	900°C 1 hr. AIR COOL 400°C TEMPER	VARIABLE
P2	0.225	0.01	0.005	0.005	1.46	0.01	0.01	0.01	0.01	0.037	0.03	900°C 1 hr. AIR COOL 400°C TEMPER	
P3	0.39	0.01	0.006	0.006	1.23	-	-	0.015	-	0.032		900°C 1 hr. AIR COOL 400°C TEMPER	
P4	0.075	0.12	0.010	0.009	2.1	0.63	0.13	0.23	-	-	-	920°C 1 hr. AIR COOL 400°C TEMPER	
P5	0.168	0.60	0.033	0.022	1.12	0.01	0.01	0.01	0.01	-	-	910°C 1 hr. AIR COOL 400°C TEMPER	

TABLE 1 : COMPOSITION, HEAT TREATMENT AND GRAIN SIZE DETAILS OF LABORATORY PRODUCED ALLOYS

ALLOY	C	Si	S	P	Mn	Ni	Cr	Mo	Sn	Al	Cu	HEAT TREATMENT	GRAIN SIZE
P6	0.34	0.49	0.034	0.018	1.56	0.10	0.12	0.06		0.019	0.15	--	4.5μ
P7	0.14	0.34	0.02	0.015	0.65	0.23	2.25	0.87			0.11	--	
P8	0.215	0.06	0.029	0.011	0.83	0.03	0.05	0.02	0.006		0.07	--	25 μ
P9	0.215	0.03	0.039	0.020	0.64	0.01	0.02	0.01	0.003		0.05	--	30 μ
P10	0.17	0.18	0.015	0.020	1.28	0.03	0.12	0.04	0.011		0.16	--	8 μ
P11 (8μ)	0.13	0.27	0.015	0.020	1.21	0.05	0.07	0.03				--	8.5μ
P11 (42μ)	0.13	0.27	0.015	0.020	1.21	0.05	0.07	0.03				1 HOUR AT 1000°C. COOLED IN VACUO	42 μ

TABLE 2 : COMPOSITION, HEAT TREATMENT AND GRAIN SIZE DETAILS OF COMMERCIAL ALLOYS

TABLE 3 : PRE-CRACKING CONDITIONS EMPLOYED

ALLOY	K_{fm}	K_{fa}
P6	44.5 $MNm^{-3/2}$	29 $MNm^{-3/2}$
P7	80 $MNm^{-3/2}$	29 $MNm^{-3/2}$
P8	22.6 $MNm^{-3/2}$	20 $MNm^{-3/2}$
P9	21.2 $MNm^{-3/2}$	19 $MNm^{-3/2}$
P10	36.3 $MNm^{-3/2}$	25 $MNm^{-3/2}$
P11 (8μ)	20.1 $MNm^{-3/2}$	18 $MNm^{-3/2}$
P11 (42μ)	14.1 $MNm^{-3/2}$	12 $MNm^{-3/2}$

K_{fm} = Maximum permissible applied fatigue stress intensit

K_{fa} = Maximum actual applied fatigue stress intensity durin growth of final 2mm of fatigue crack.

TABLE 4 :

ALLOY	YIELD STRESS σ_y Kg. mm^{-2}	U.T.S. Kg. mm^{-2}	% ELONGATION
P6	45.3	59.9	25
P7	81.1	115.9	19
P8	22.9	36.8	56
P9	21.5	35.3	60
P10	36.84	46.6	43
P11 (8μ)	20.4	29.2	35
P11 (42μ)	14.3	25.4	48

ROOM TEMPERATURE PROPERTIES OF THE ALLOYS.

TABLE 5

ALLOY	TOTAL PROJECTED INCLUSION LENGTH mm. mm^{-2}	SULPHIDE PROJECTED LENGTH mm. mm^{-2}	OXIDE PROJECTED LENGTH mm. mm^{-2}	SULPHIDE AREA %	OXIDE AREA %
P6	0.6463	-	-	-	-
P7	0.6778	0.5628	0.0657	0.0887	0.0132
P8	1.5139	0.5672	0.7228	0.0329	0.1280
P9	0.4287	0.2454	0.1532	0.0619	0.0234
P10	0.5046	0.3844	0.0998	0.0621	0.0219
P11	0.4703	-	-	-	-

TRUE STRAIN ε_T %	TRUE STRESS σ_T Kg. mm^{-2}
2.0	49.67
2.5	52.23
3.0	54.51
3.5	56.60
4.0	58.54
4.5	60.16
5.0	61.57
5.5	62.83
6.0	64.00
6.5	65.13
7.0	66.13
7.5	67.08
8.0	67.94
8.5	68.73
9.0	69.48
9.5	70.23
10.0	70.92

TABLE 6 : EXPERIMENTALLY OBTAINED VALUES OF TRUE STRESS AND TRUE STRAIN FOR ALLOY P6 AT -10°C

TRUE STRAIN ε_T %	$d\sigma'_T/d\varepsilon_T$ FROM POLYNOMIAL	$d\sigma'_T/d\varepsilon_T$ BY CALCULATION	% CHANGE
2.5	488	495	- 1.4
3.0	446	341	+ 3.4
3.5	396	384	+ 3.0
4.0	348	346	+0.6
4.5	306	317	-3.6
5.0	271	292	-7.7
5.5	244	231	+5.3
6.0	224	216	+3.6
6.5	209	202	+3.3
7.0	195	191	+2.1
7.5	182	180	+1.1
8.0	169	171	-1.2
8.5	155	163	-5.2
9.0	144	156	-8.3
9.5	141	149	-5.7

TABLE 7 : COMPARISON OF CALCULATED $d\sigma'_T/d\varepsilon_T$ VALUES AND THOSE OBTAINED BY POLYNOMIAL ANALYSIS : ALLOY P6, -10°C.

P6		P7		P8		P9		P10		P11 (8μ)		P11 (42μ)		Temperatur ^{o}C
Average $\delta_i$mm	% Scatter	Average $\delta_i$mm	% Scatter	Average $\delta_i$mm	% Scatter	Average $\delta_i$mm	% Scatter	Average $\delta_i$mm	% Scatter	Average $\delta_i$mm	% Scatter	Average i	% Scatter	
0.123	+12 -26	0.0812	+14 -11	0.381	+5 -5	0.492	+14 -9	Only one result		0.317	+5 -3	0.221	+8 -5	20
				0.292	+14 -14	0.408	+4 -4	0.501	+0.5 -0.5					0
0.0919	+18 -18	0.0506	+21 -13	0.270	+19 -19	0.304	+20 -14	0.512	+3 -3	0.249	+26 -21	0.191	+1 -1	-30
				0.215	+28 -14	0.249	+16 -9	0.342	+8 -6					-45
0.0676	-59 +35	0.0524	+6 -6											-50
				0.265	+9 -5	0.194	+24 -24	0.299	+14 -14					-60
0.109	+10 -6	0.0363	+3 -3	0.123	+2 -2	0.0823	+17 -14	0.272	+15 -15	0.179	+2 -2	only one result		-77
0.0285	+5 -5	0.0240	+6 -6											-196

TABLE 8.

AVERAGE CRITICAL C.O.D. VALUES FOR ALLOYS INVESTIGATED, AND % SCATTER ABOUT THE AVERAGE

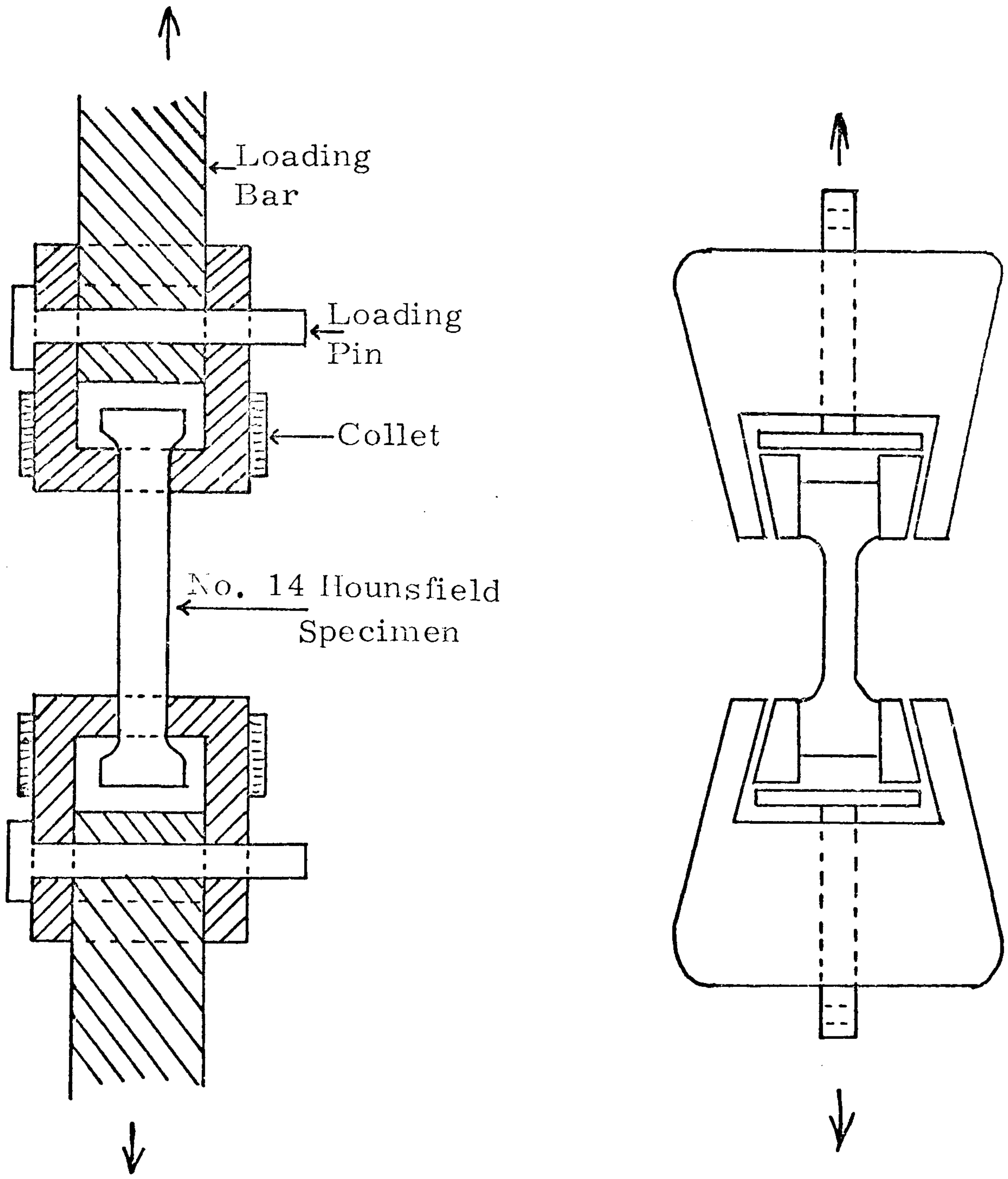

Test Rig used in Testing of Standard No. 14 Hounsfield Specimens.

For Sub-ambient Testing The Test Rig was encased in a Polystyrene container and Equilibrated with a suitable Liquid.

Friction Grip arrangement employed in testing the large non-standard specimen.

FIGURE 1: TENSILE TEST RIG.

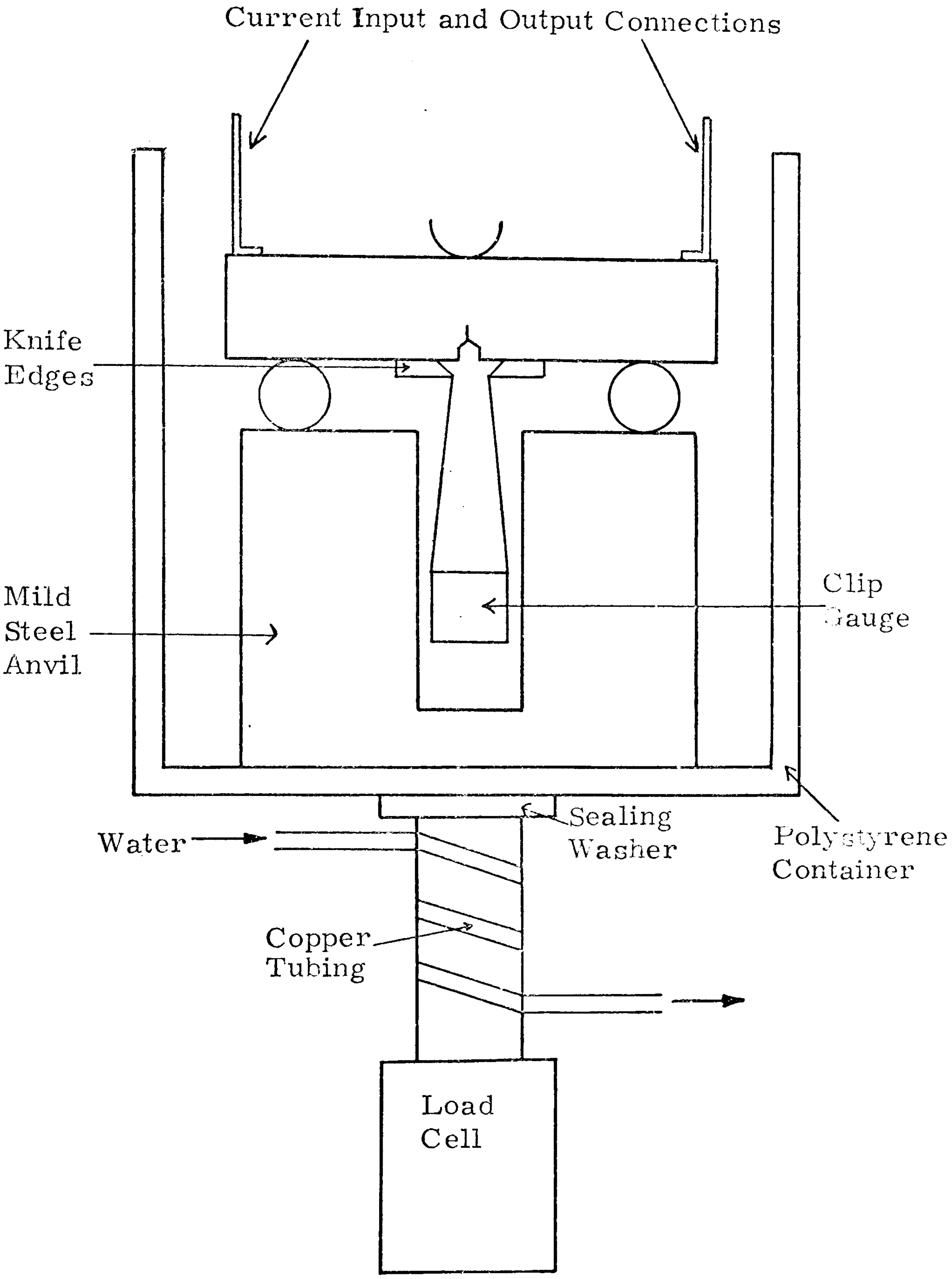

FIGURE 2: FRACTURE TOUGHNESS TEST RIG USED IN THE DETERMINATION OF AMBIENT AND SUB AMBIENT CRITICAL C.O.D. VALUES

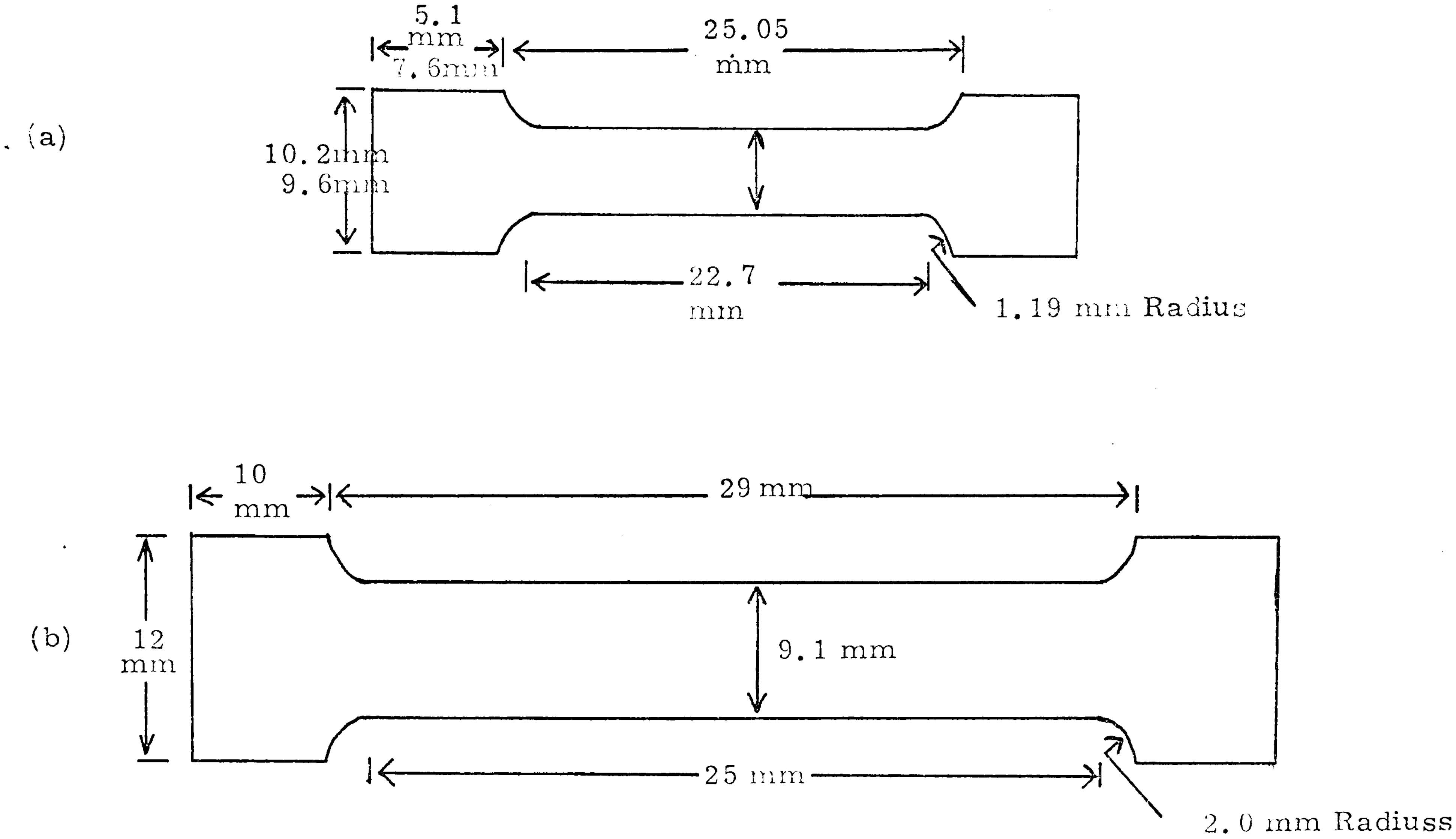

FIGURE 3: TENSILE TEST SPECIMENS UTILISED
(a) STANDARD No. 14 HOUNSFIELD
(b) NON-STANDARD SQUARE ENDED SPECIMEN

Actual Specimen Dimensions
B = 25mm
W = 25 mm
a = 8.5mm
J = 4.0 mm

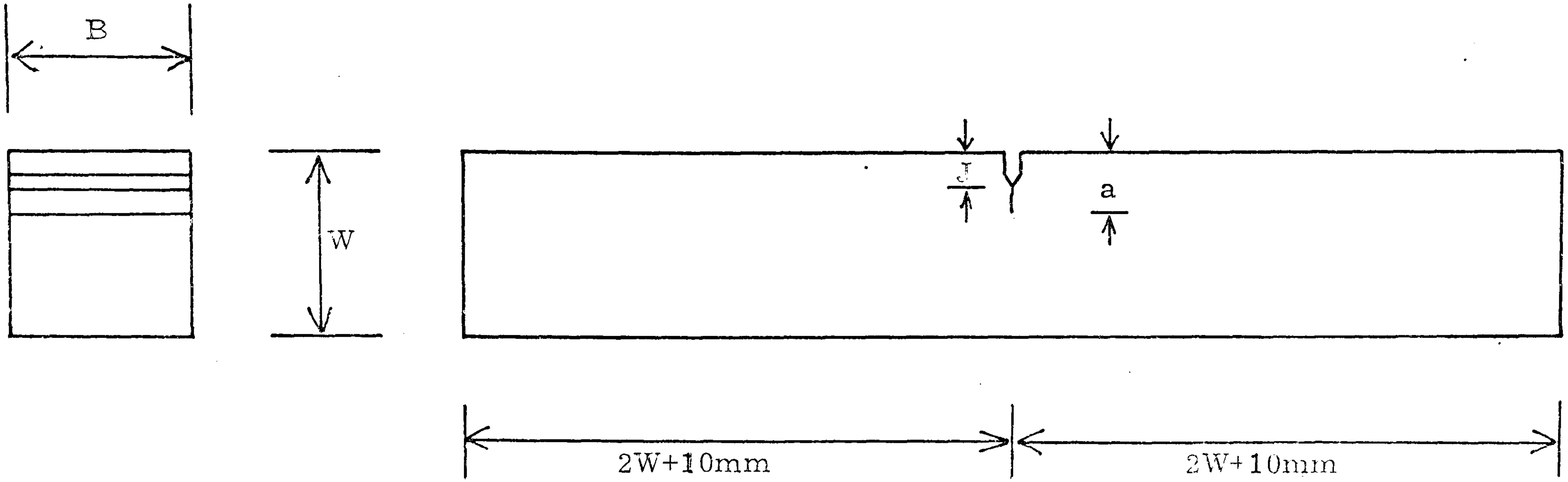

FIGURE 4: THREE POINT BEND TEST PIECE USED IN THE DETERMINATION OF CRITICAL C.O.D.

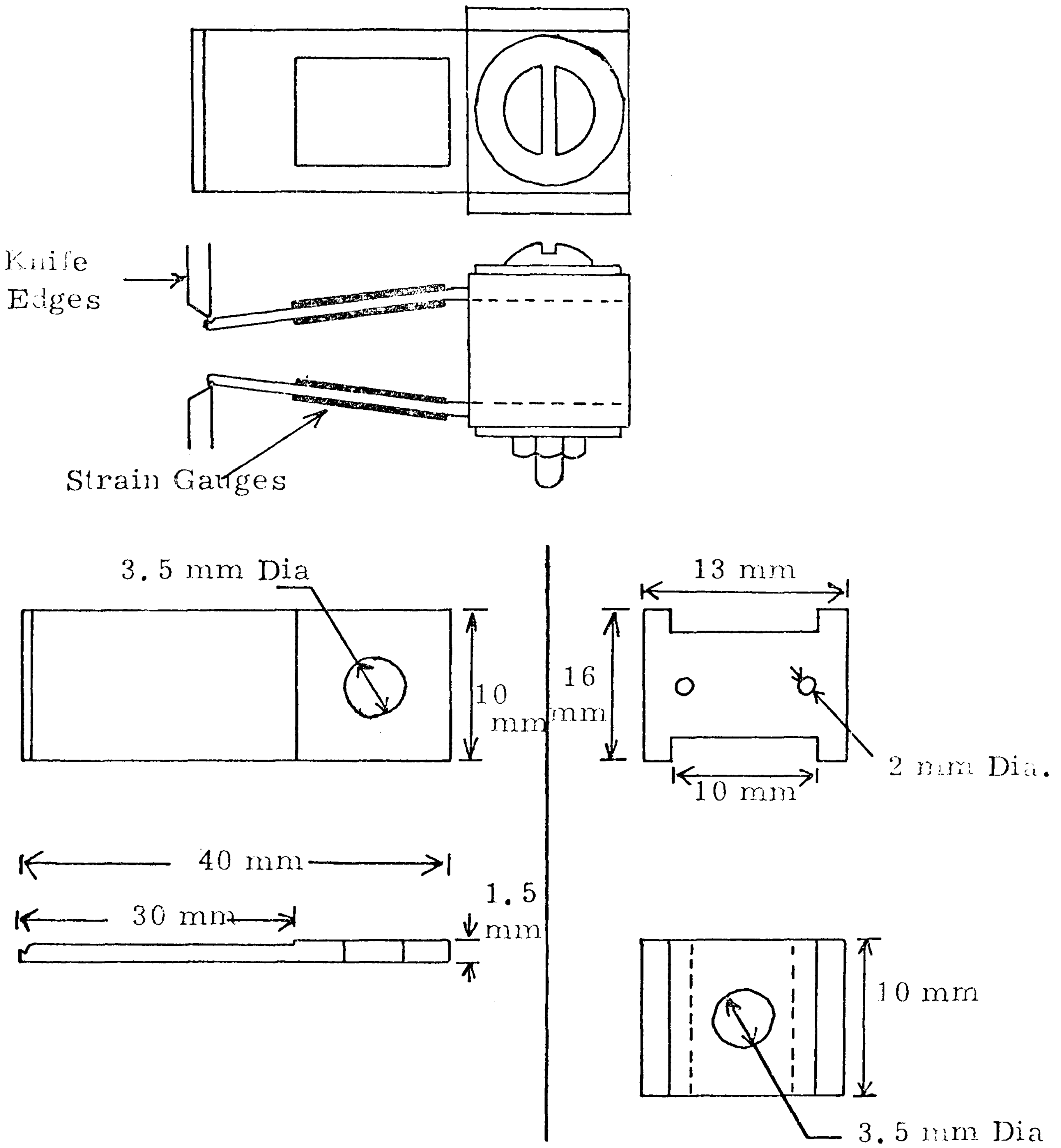

FIGURE 5: DIAGRAMMATIC REPRESENTATION OF DOUBLE CANTILEVER BEAM CLIP GAUGE

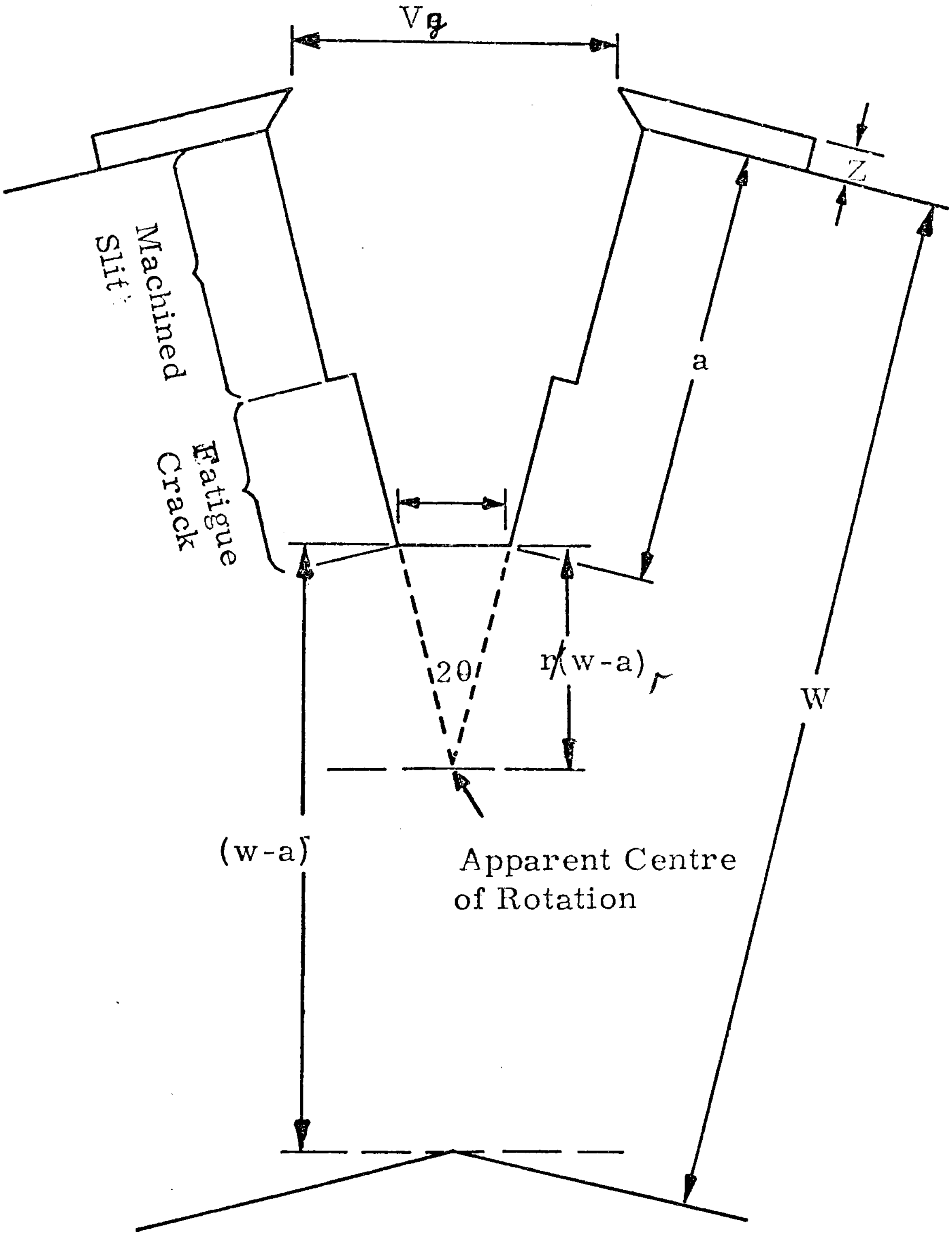

FIGURE 6: DIAGRAMMATIC REPRESENTATION OF NOTCH PROFILE DURING BENDING.

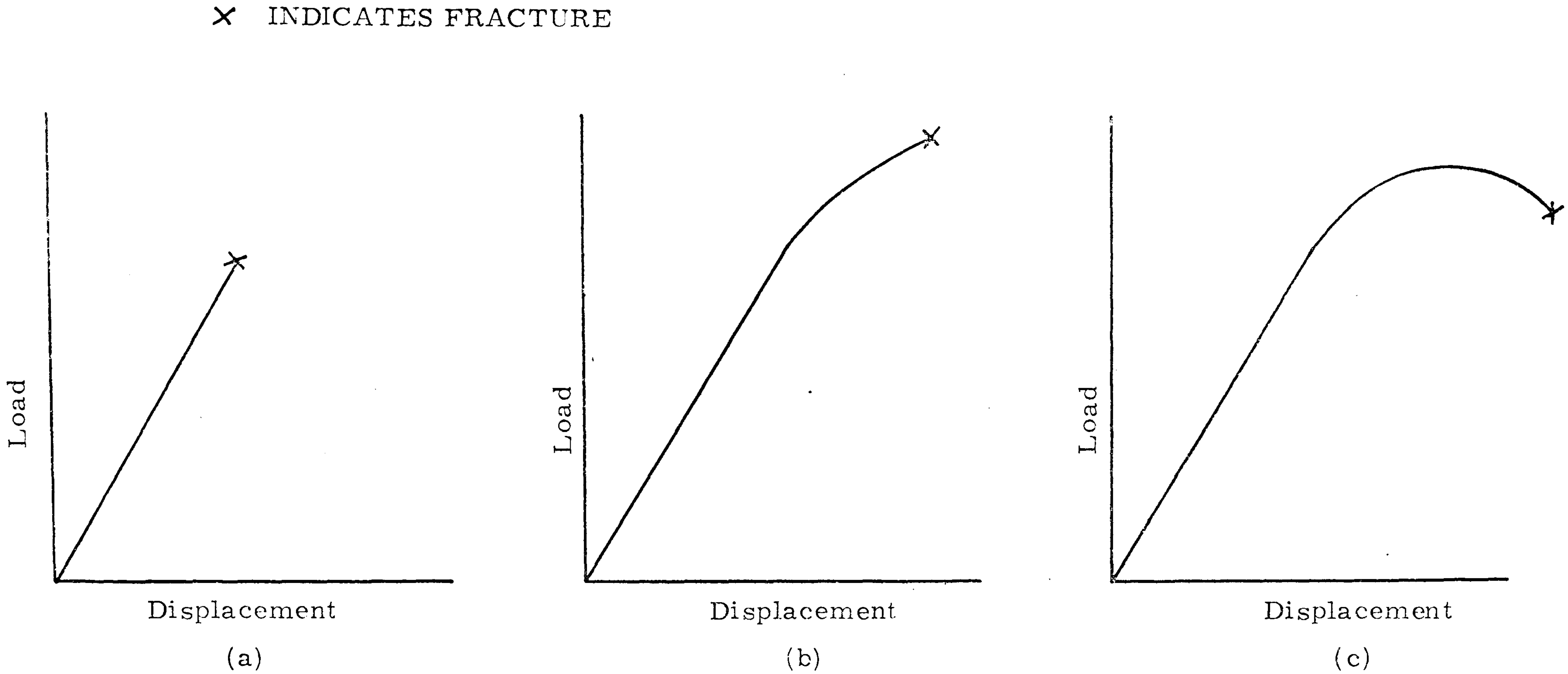

FIGURE 7: TYPICAL CURVES OF LOAD v DISPLACEMENT

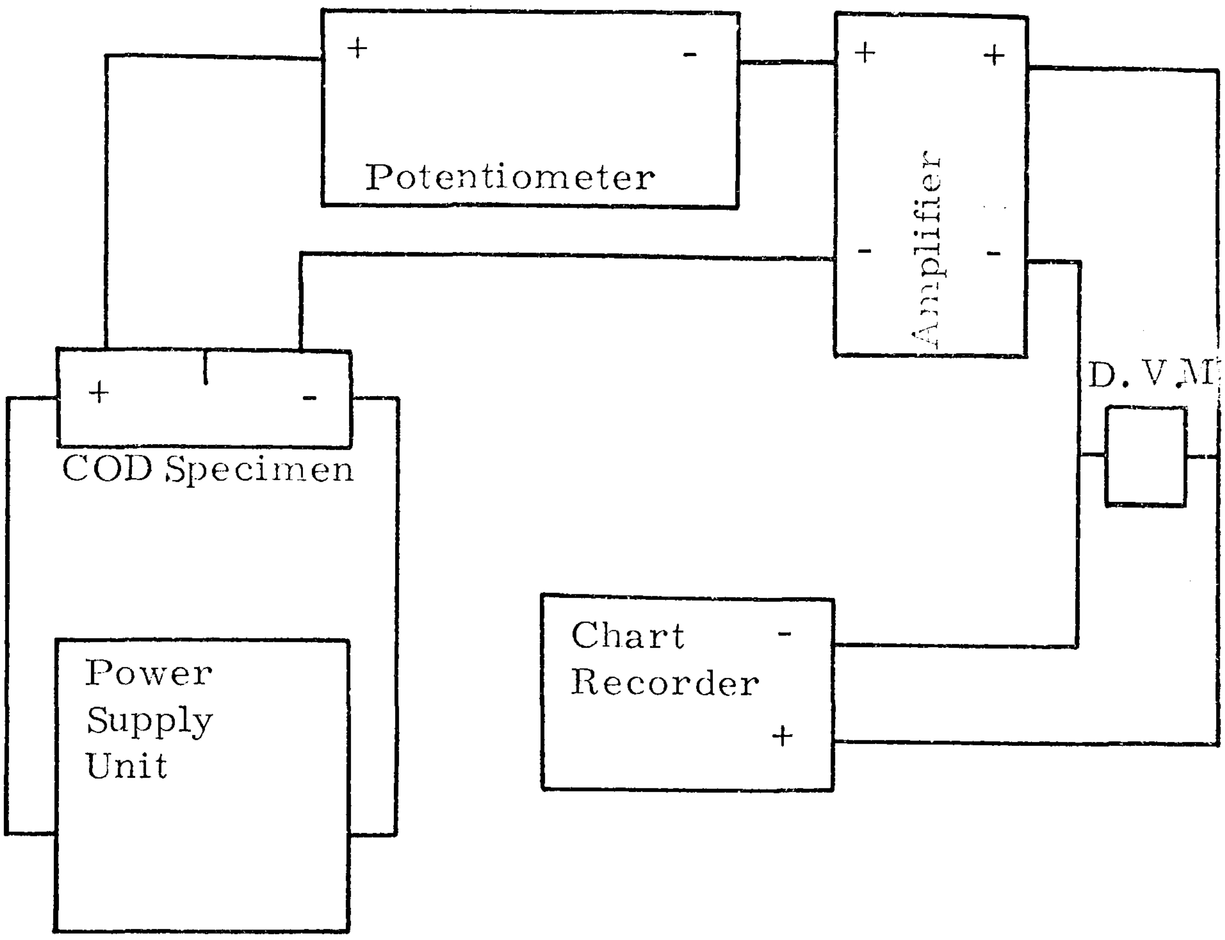

FIGURE 8: DIAGRAMMATIC REPRESENTATION OF POTENTIAL DROP EQUIPMENT

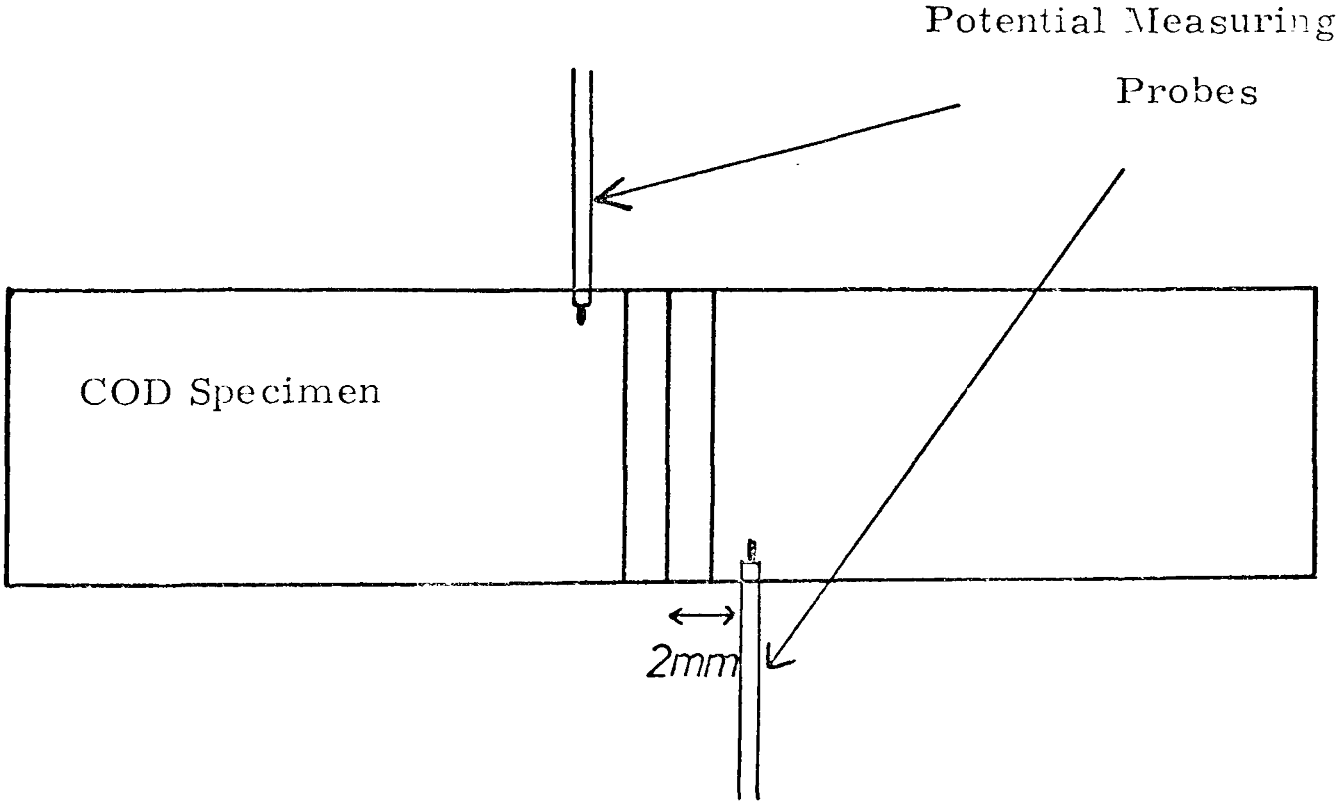

FIGURE 8A: PLAN VIEW OF COD SPECIMEN SHOWING POTENTIAL MEASURING PROBE POSITIONS WITH RESPECT TO SPECIMEN NOTCH

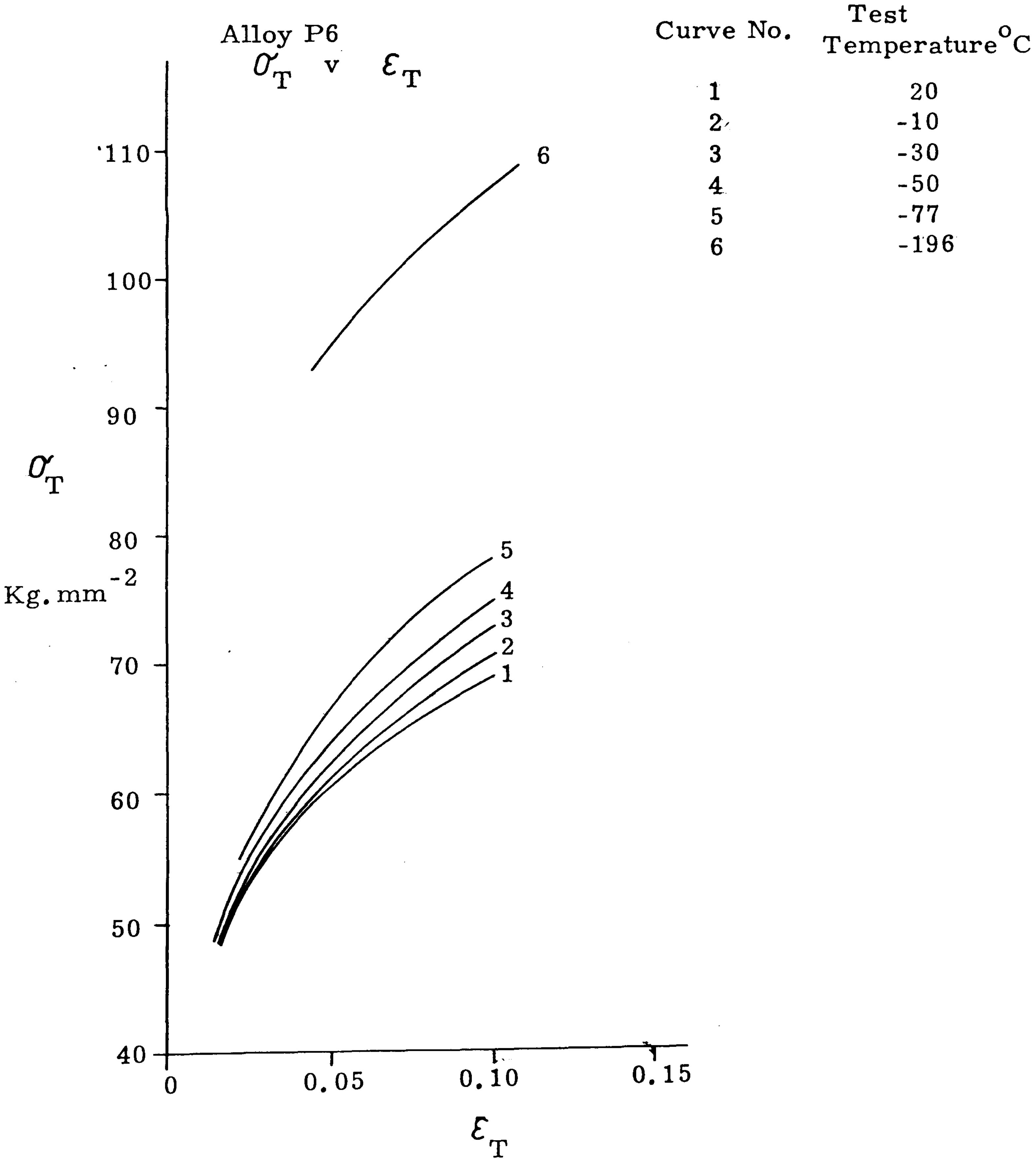

FIGURE9: FAMILY OF FLOW CURVES (ALLOY P6)

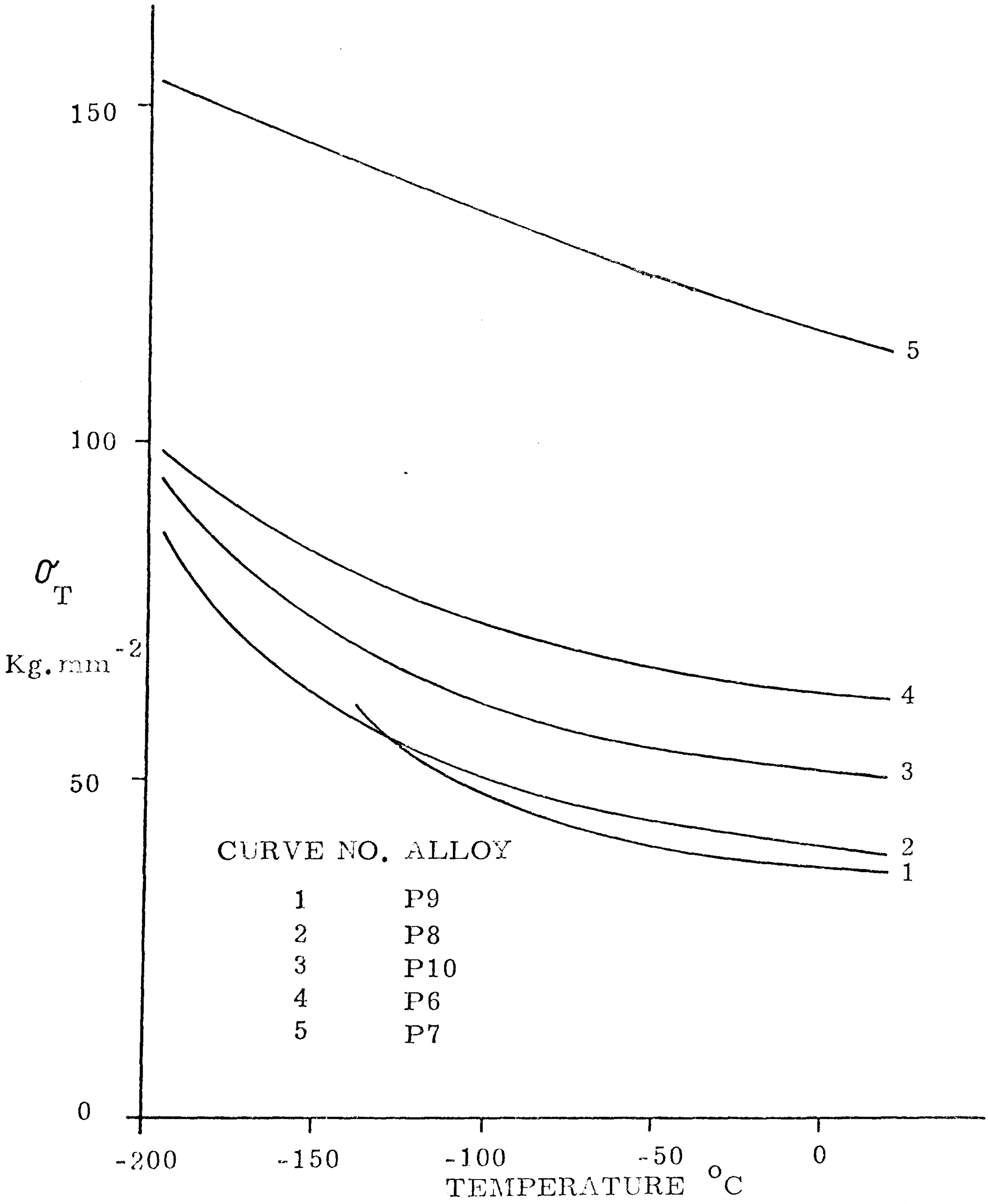

FIGURE 11: VARIATION OF TRUE STRESS (AT 6% TRUE STRAIN) WITH TEMPERATURE FOR ALLOYS P6-P10.

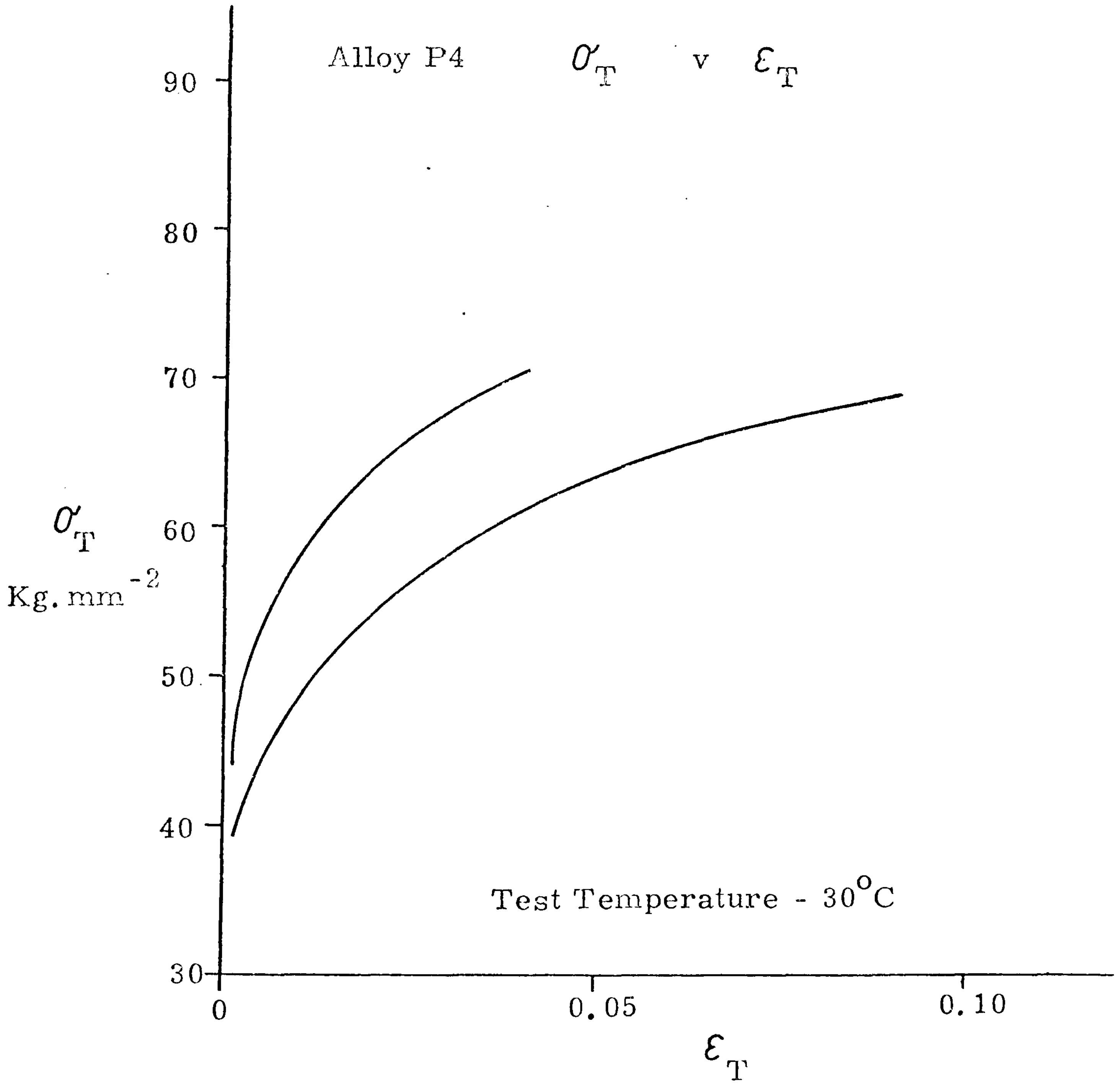

FIGURE 12: TRUE STRESS-TRUE STRAIN CURVES RESULTING FROM TENSILE TESTS PERFORMED ON TWO SPECIMENS OF ALLOY P4 UNDER IDENTICAL CONDITIONS

X100

FIGURE 13 : MICROGRAPH ILLUSTRATING VARIABLE GRAIN SIZE OF ALLOY P4.

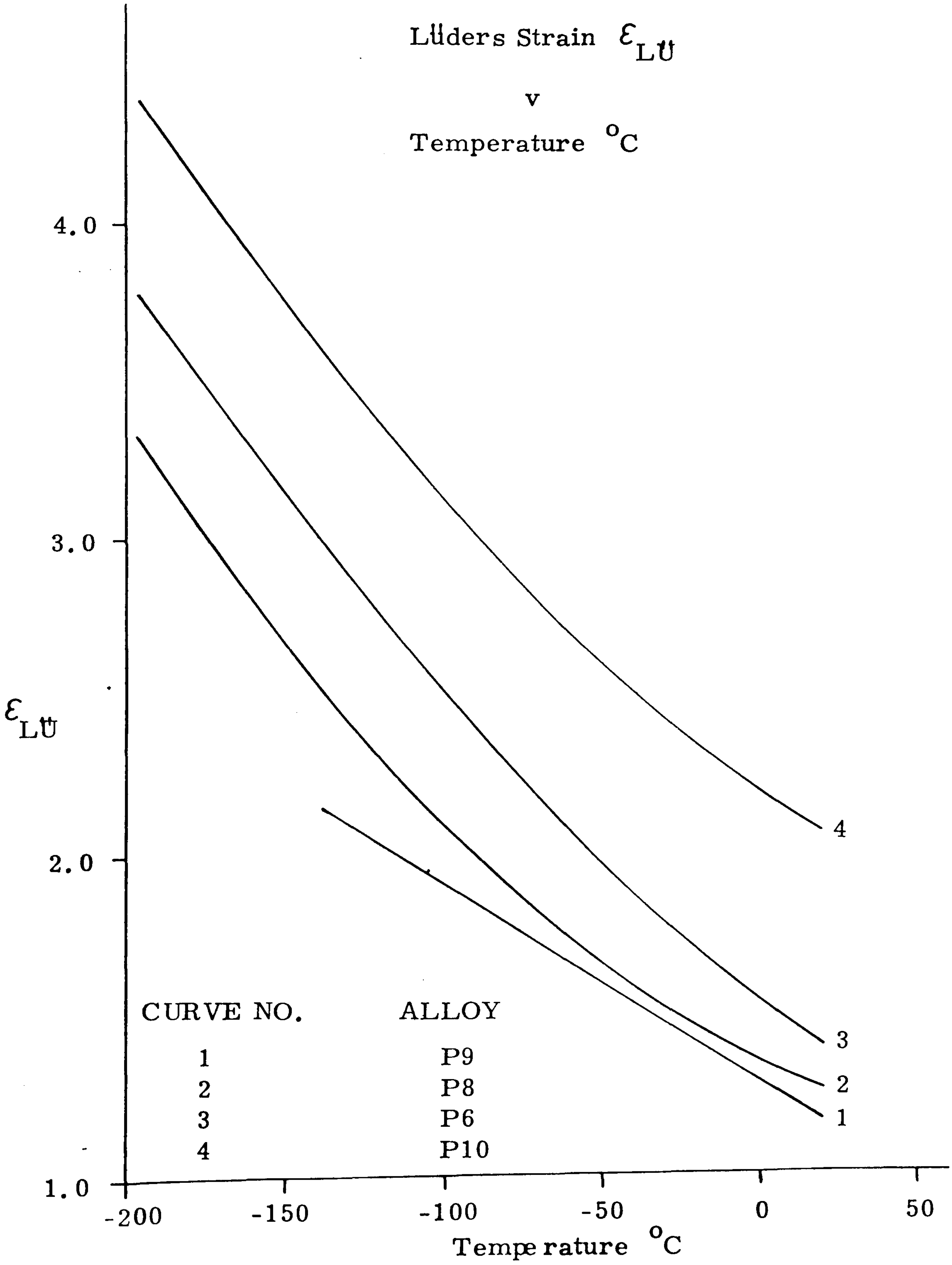

FIGURE 14: VARIATION OF LÜDERS STRAIN WITH TEMPERATURE FOR ALLOYS. P6, P8

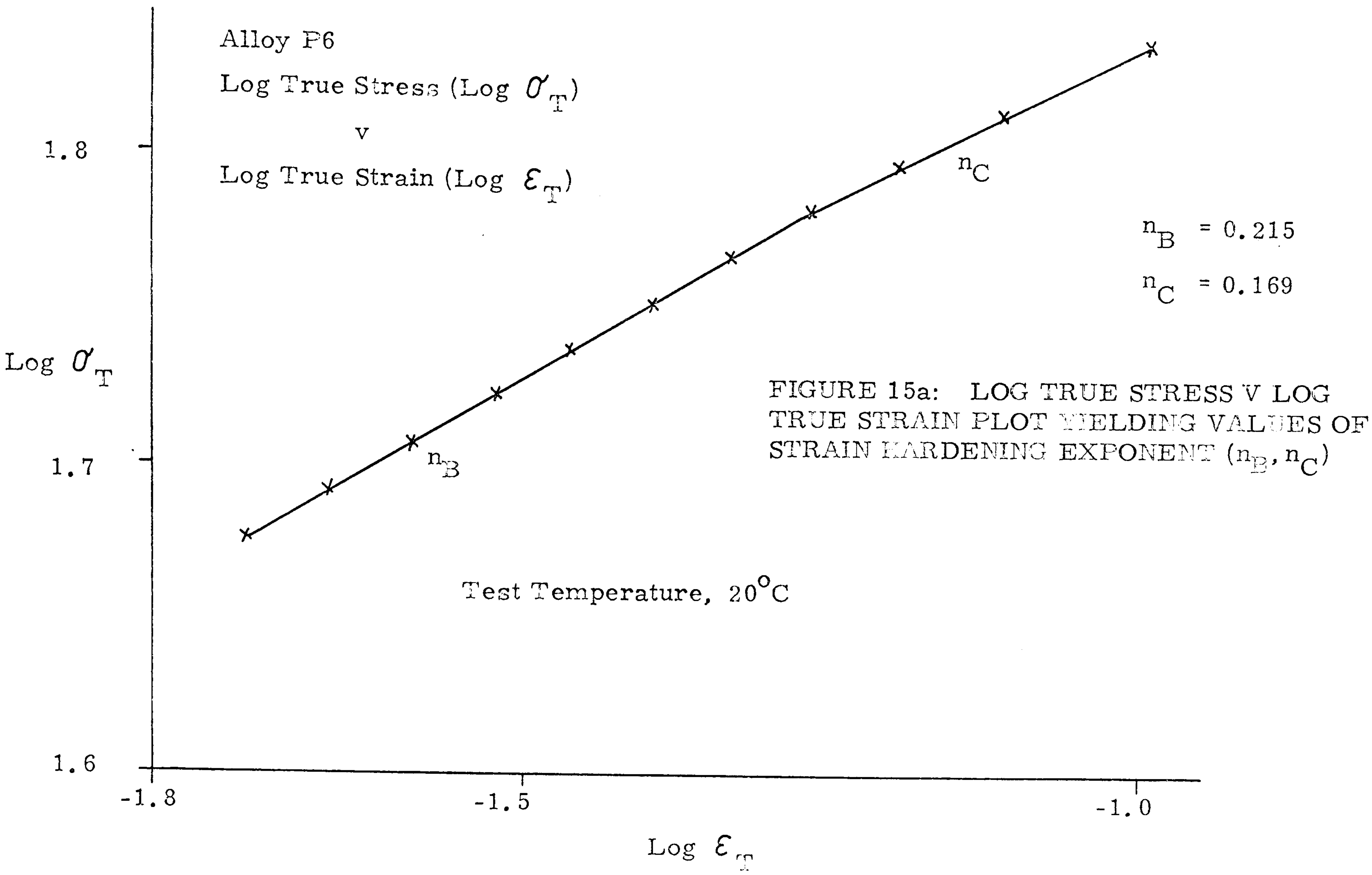

FIGURE 15a: LOG TRUE STRESS V LOG TRUE STRAIN PLOT YIELDING VALUES OF STRAIN HARDENING EXPONENT (n_B, n_C)

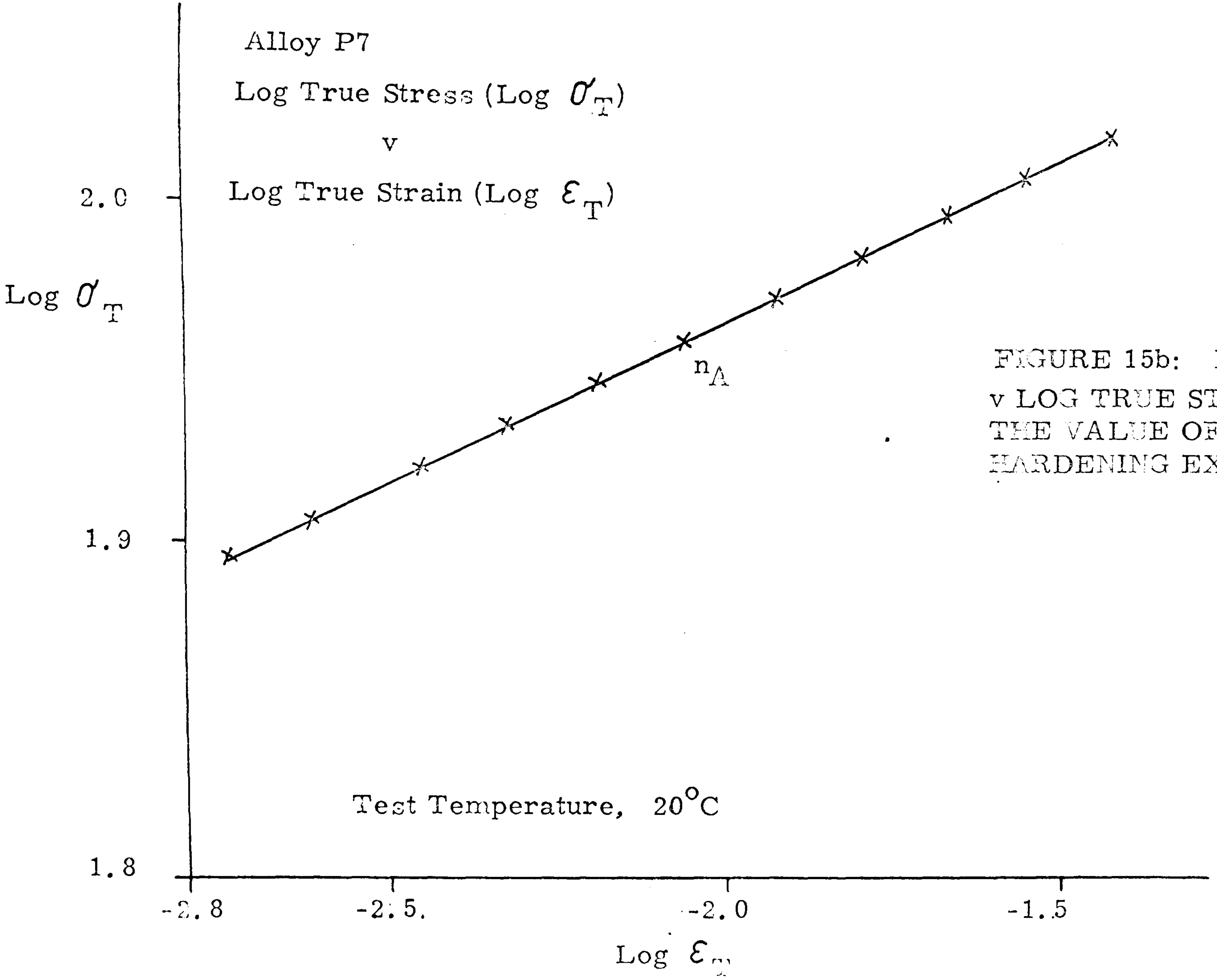

$n_A = 0.106$

FIGURE 15b: LOG TRUE STRESS v LOG TRUE STRAIN PLOT YIELDING THE VALUE OF THE STRAIN HARDENING EXPONENT (n_A)

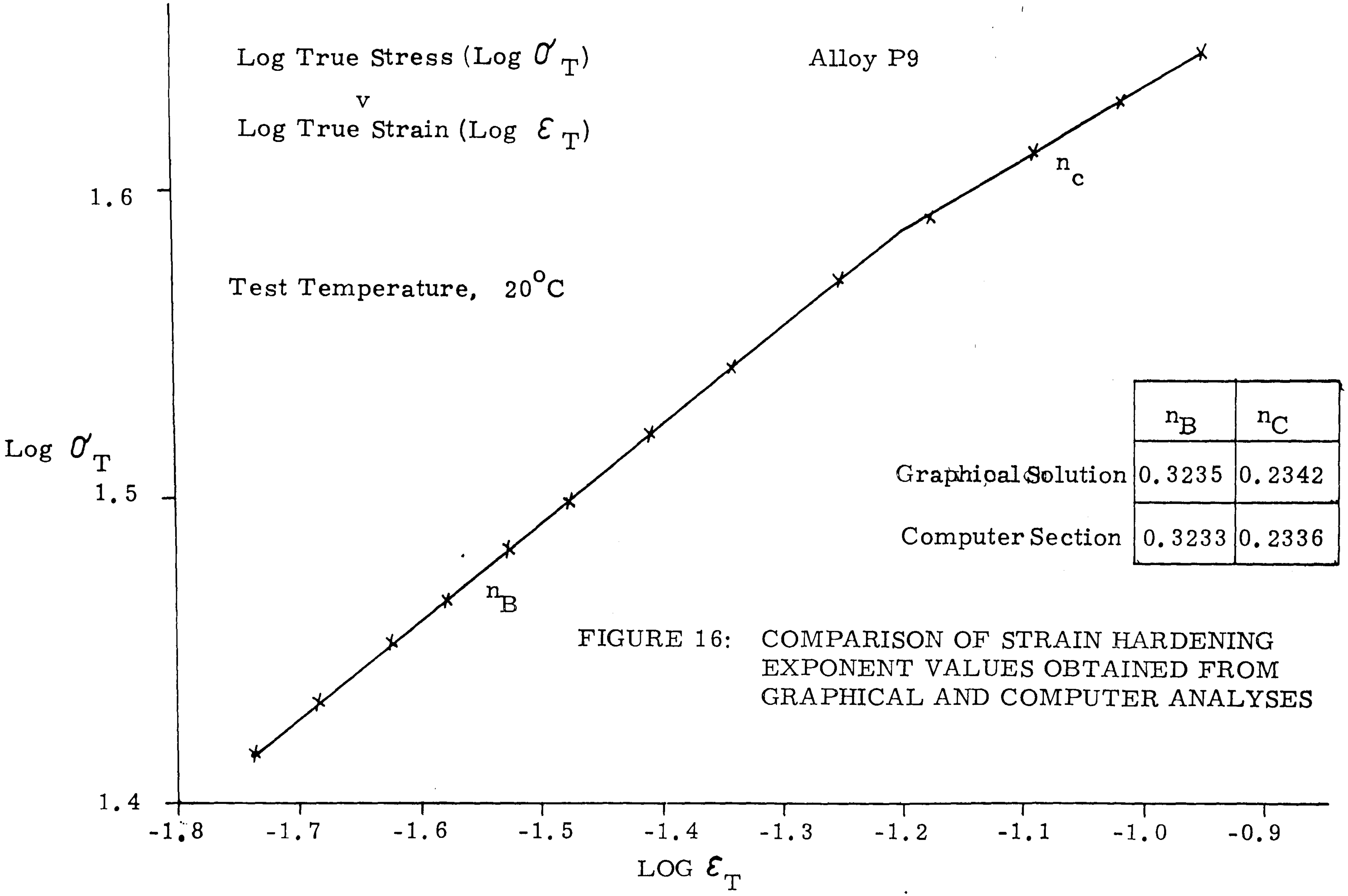

	n_B	n_C
Graphical Solution	0.3235	0.2342
Computer Section	0.3233	0.2336

FIGURE 16: COMPARISON OF STRAIN HARDENING EXPONENT VALUES OBTAINED FROM GRAPHICAL AND COMPUTER ANALYSES

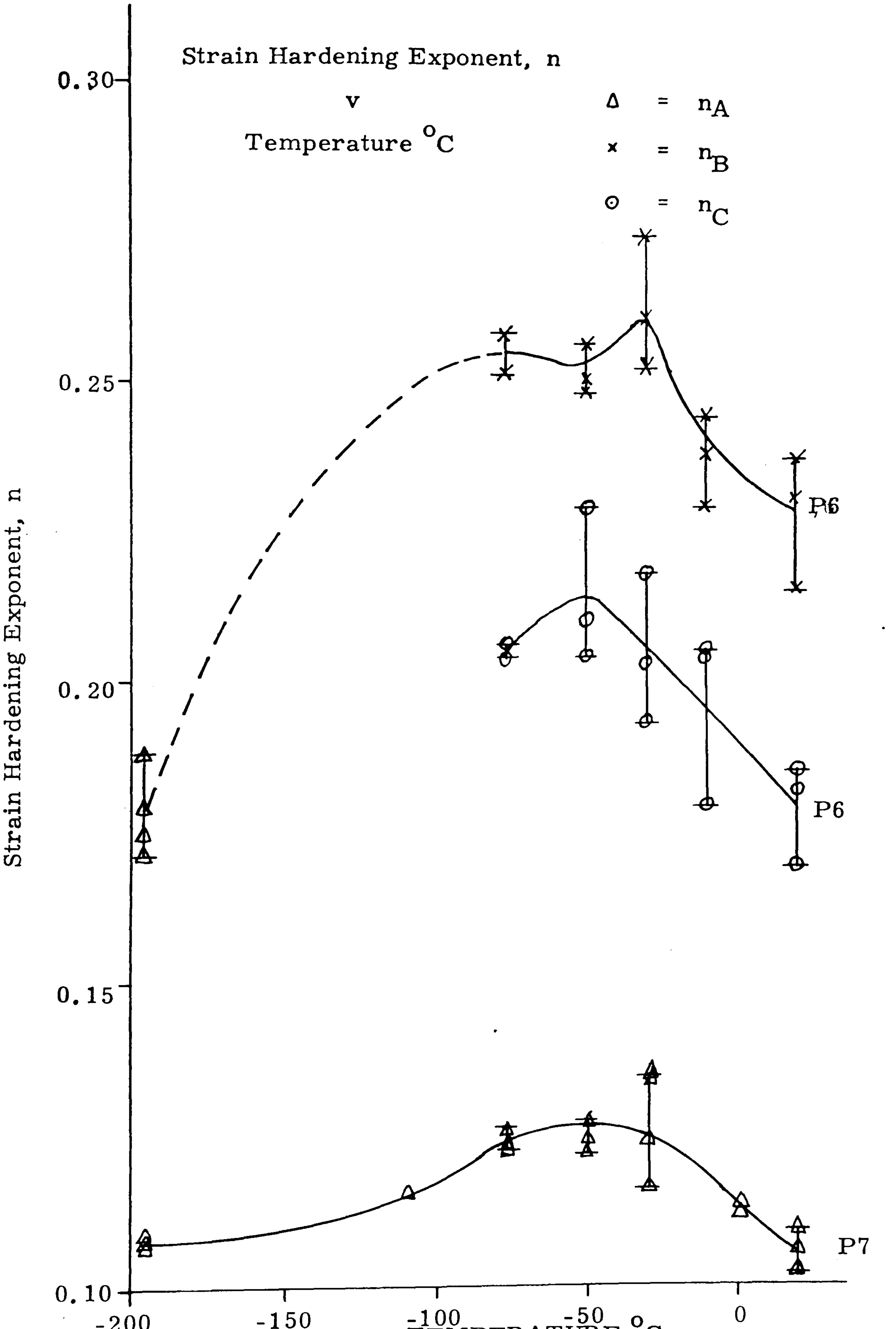

FIGURE 17: VARIATION OF STRAIN HARDENING EXPONENT VALUES WITH TEMPERATURE FOR ALLOYS P6 AND P7

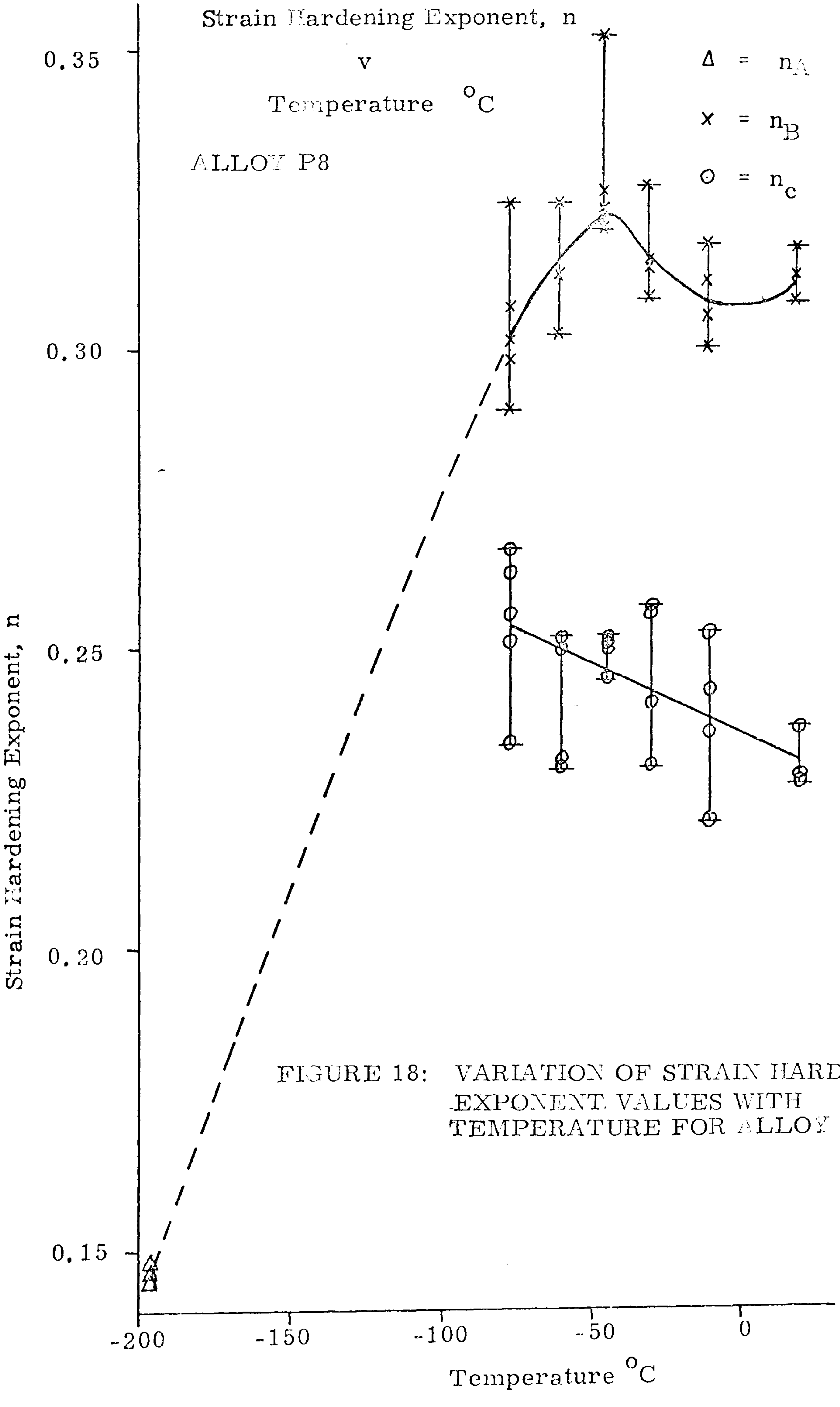

FIGURE 18: VARIATION OF STRAIN HARDENING EXPONENT VALUES WITH TEMPERATURE FOR ALLOY P8.

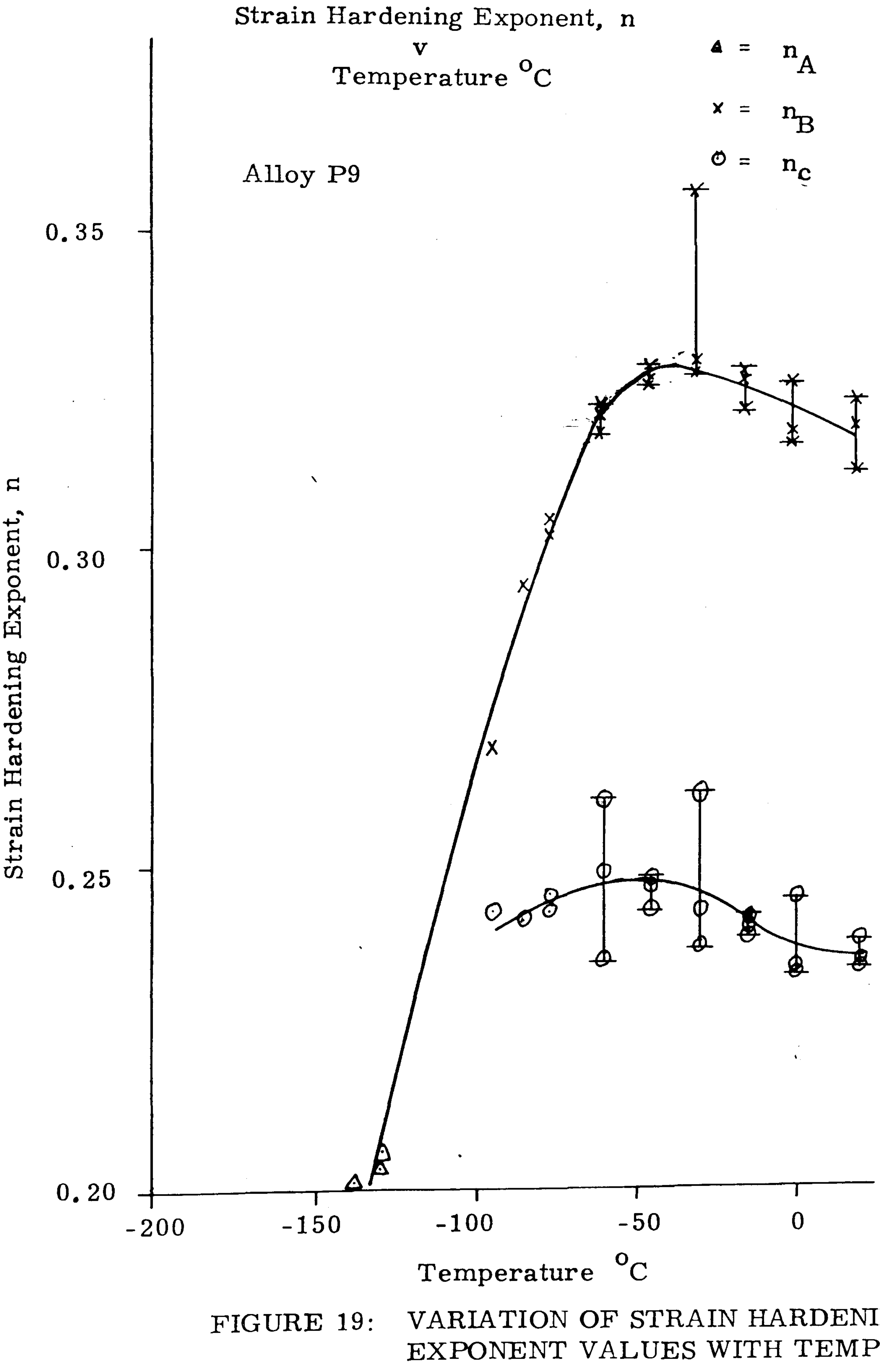

FIGURE 19: VARIATION OF STRAIN HARDENING EXPONENT VALUES WITH TEMPERATURE FOR ALLOY P9

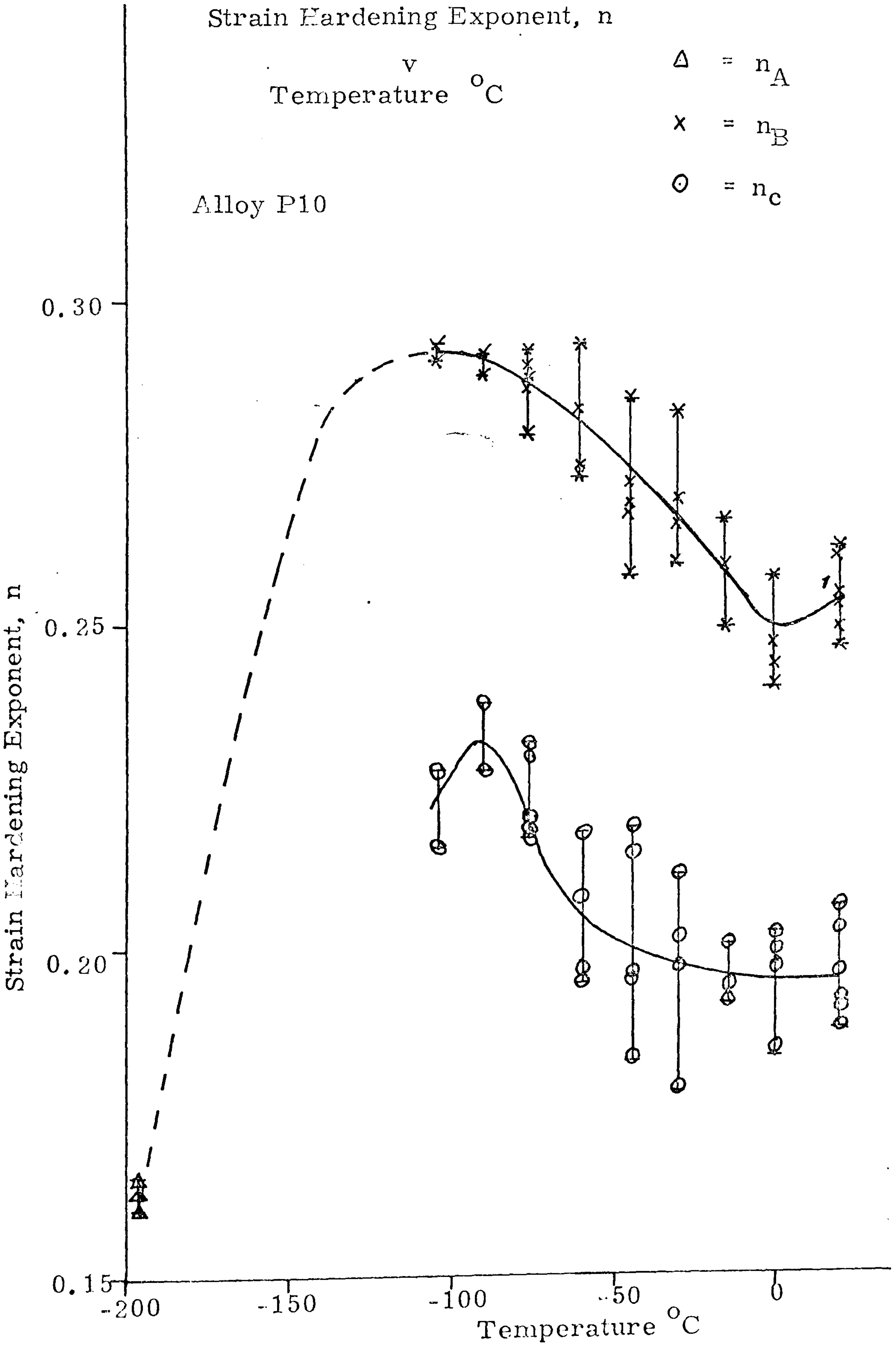

FIGURE 20: VARIATION OF STRAIN HARDENING EXPONENT VALUES WITH TEMPERATURE FOR ALLOY P10

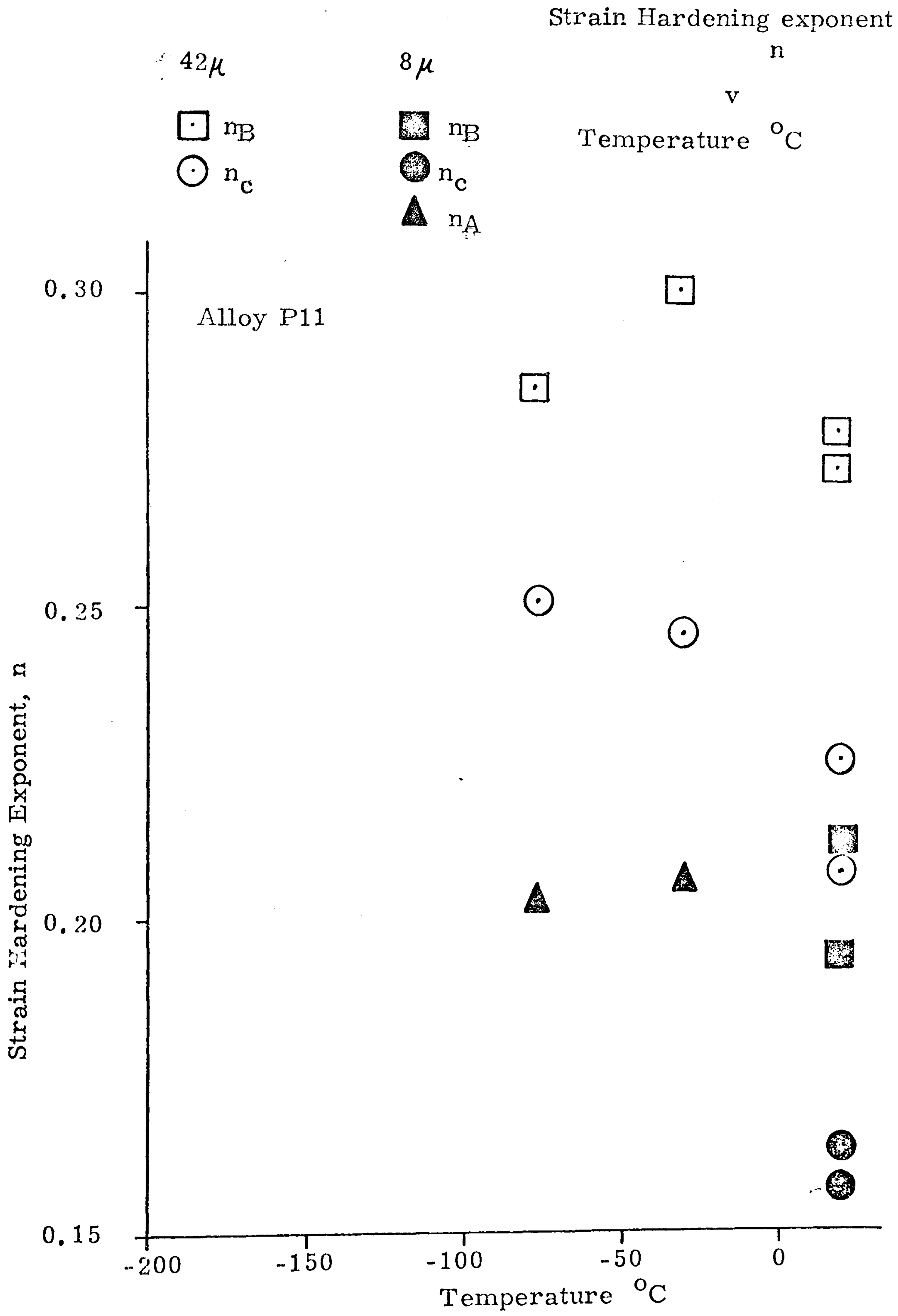

FIGURE 21: VARIATION OF STRAIN HARDENING EXPONENT VALUES WITH TEMPERATURE FOR ALLOY P11 (GRAIN SIZE 42μ, AND 8μ)

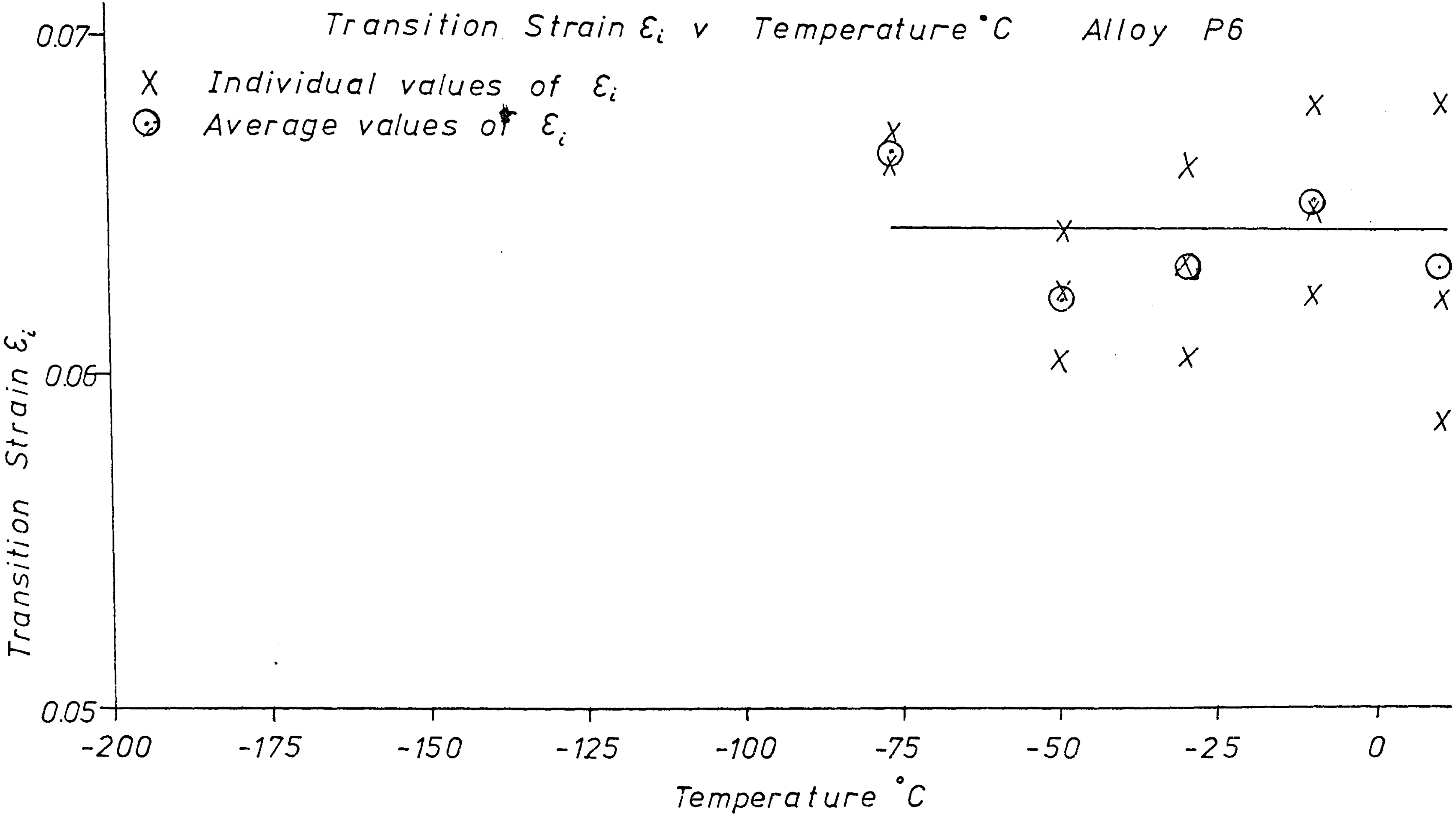

FIGURE 22(a): VARIATION OF TRANSITION STRAIN WITH TEMPERATURE FOR ALLOY P6

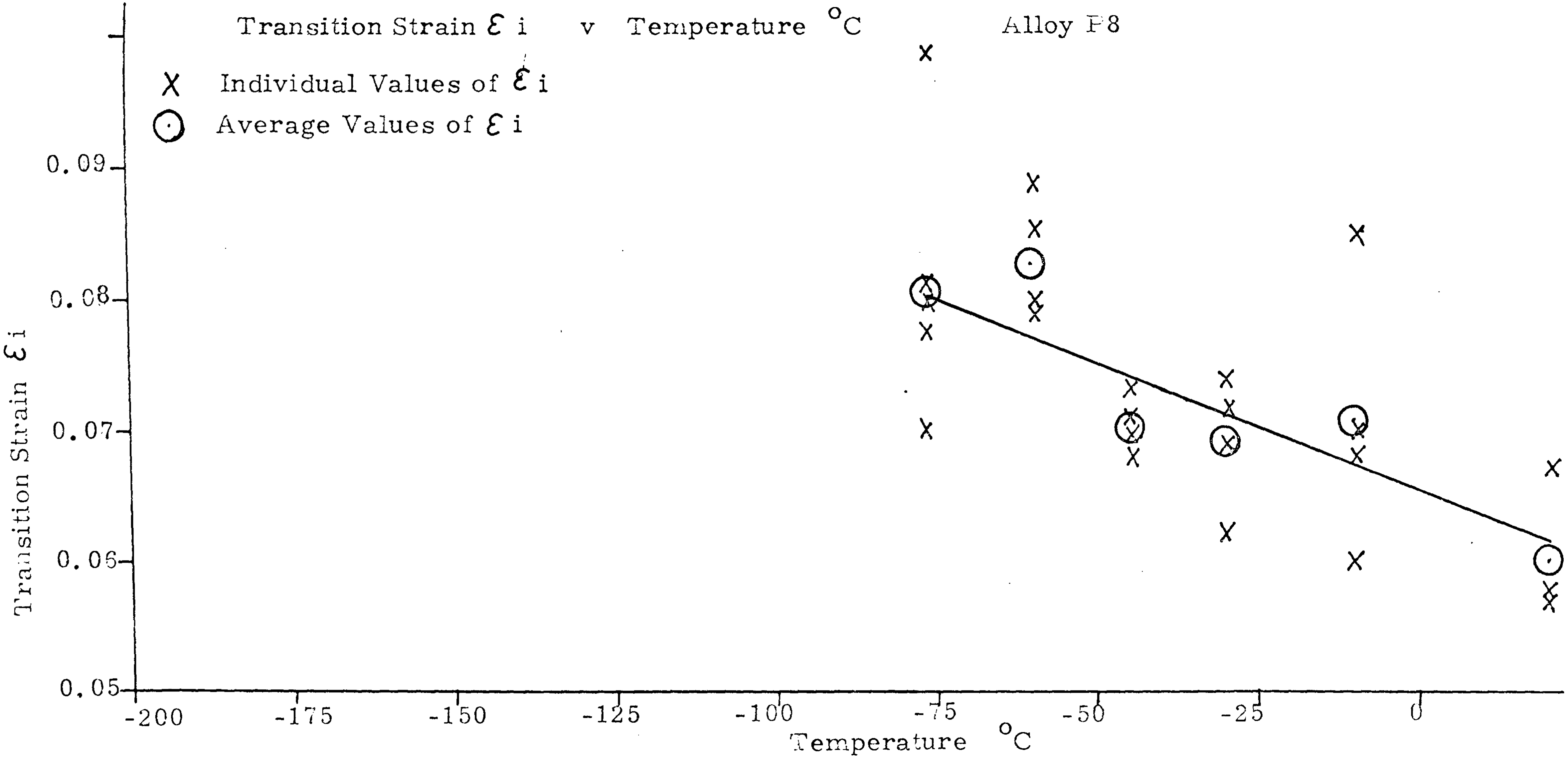

FIGURE 22(b): VARIATION OF TRANSITION STRAIN WITH TEMPERATURE FOR ALLOY P8

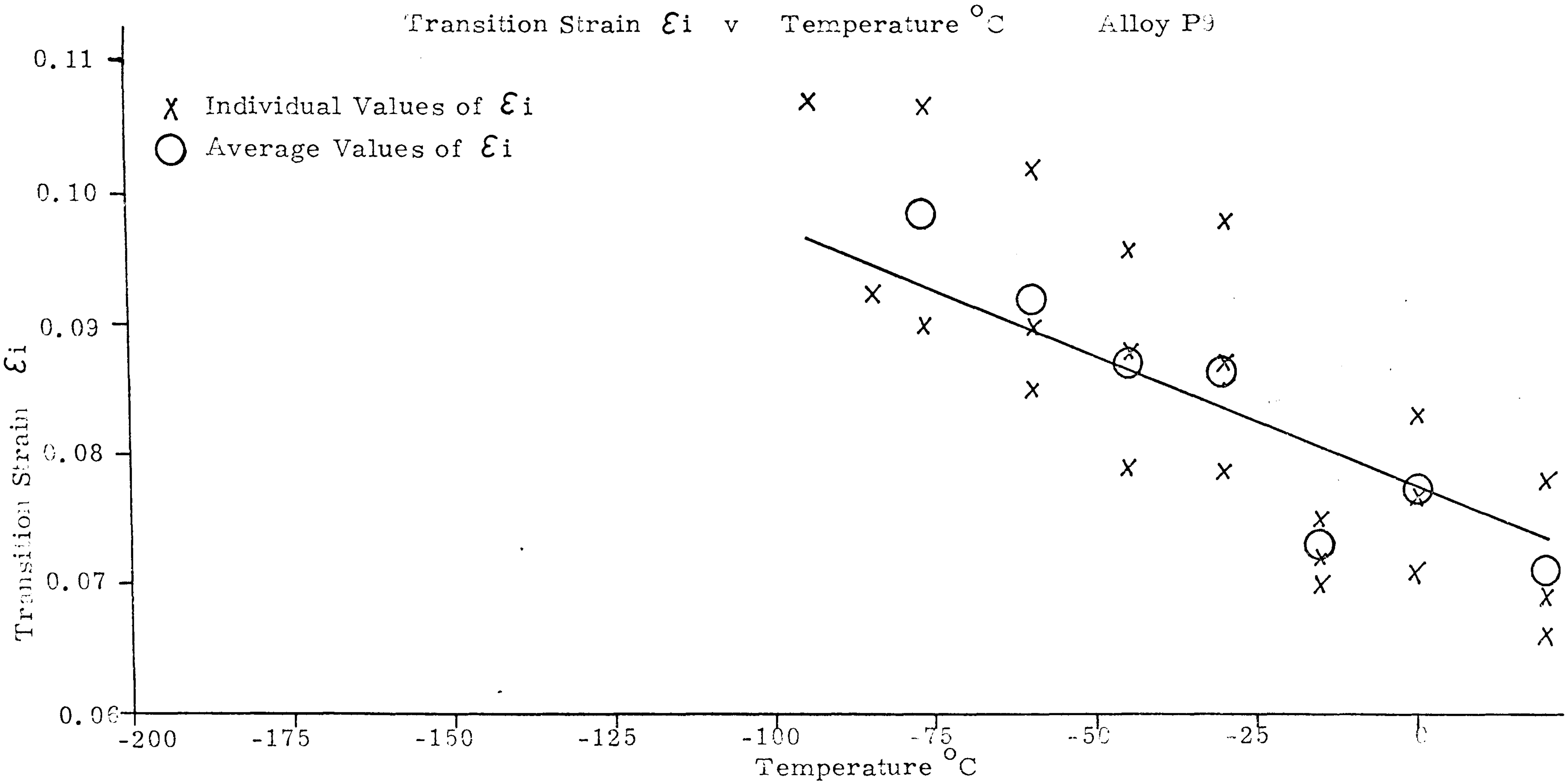

FIGURE 22(c): VARIATION OF TRANSITION STRAIN WITH TEMPERATURE FOR ALLOY P9

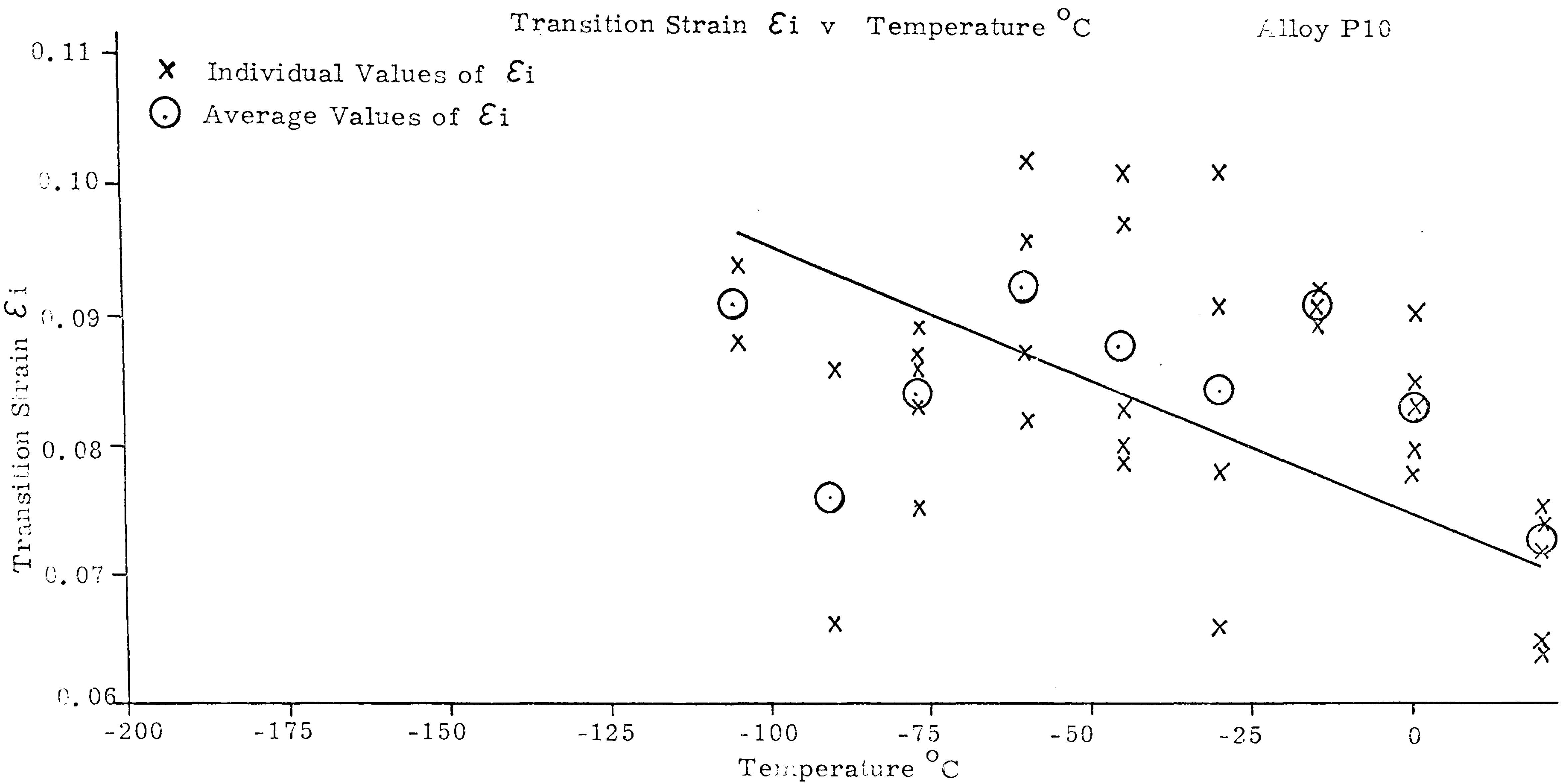

FIGURE 22(d): VARIATION OF TRANSITION STRAIN WITH TEMPERATURE FOR ALLOY P10

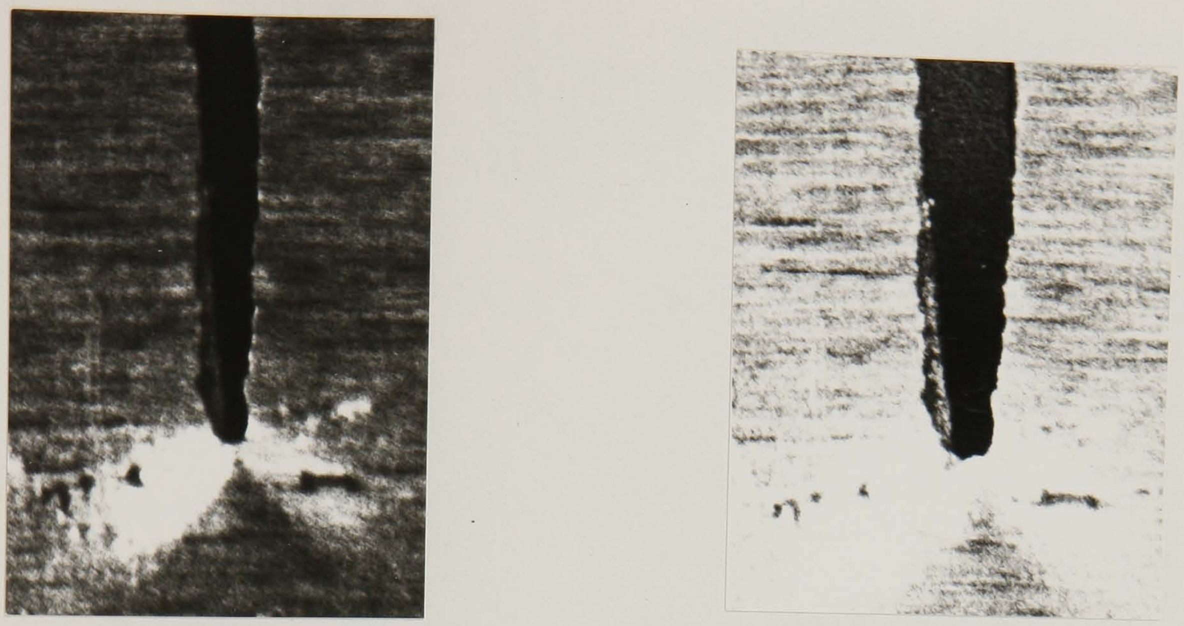

(a) $d = 0.029$ mm
$r = 0.109$

(b) $d = 0.058$ mm
$r = 2.4$

(c) $d = 0.225$ mm
$r = 2.6$

(d) $d = 0.275$ mm
$r = 2.5$

FIGURE 23 : PHOTOGRAPHS OF CRACK TIP AREA DURING C.O.D. TESTING, AT SUCCESSIVELY HIGHER LOADS

FIGURE 24: RELATIONSHIP BETWEEN SURFACE DISPLACEMENT (V_g) AND ROTATIONAL CONSTANT (r)

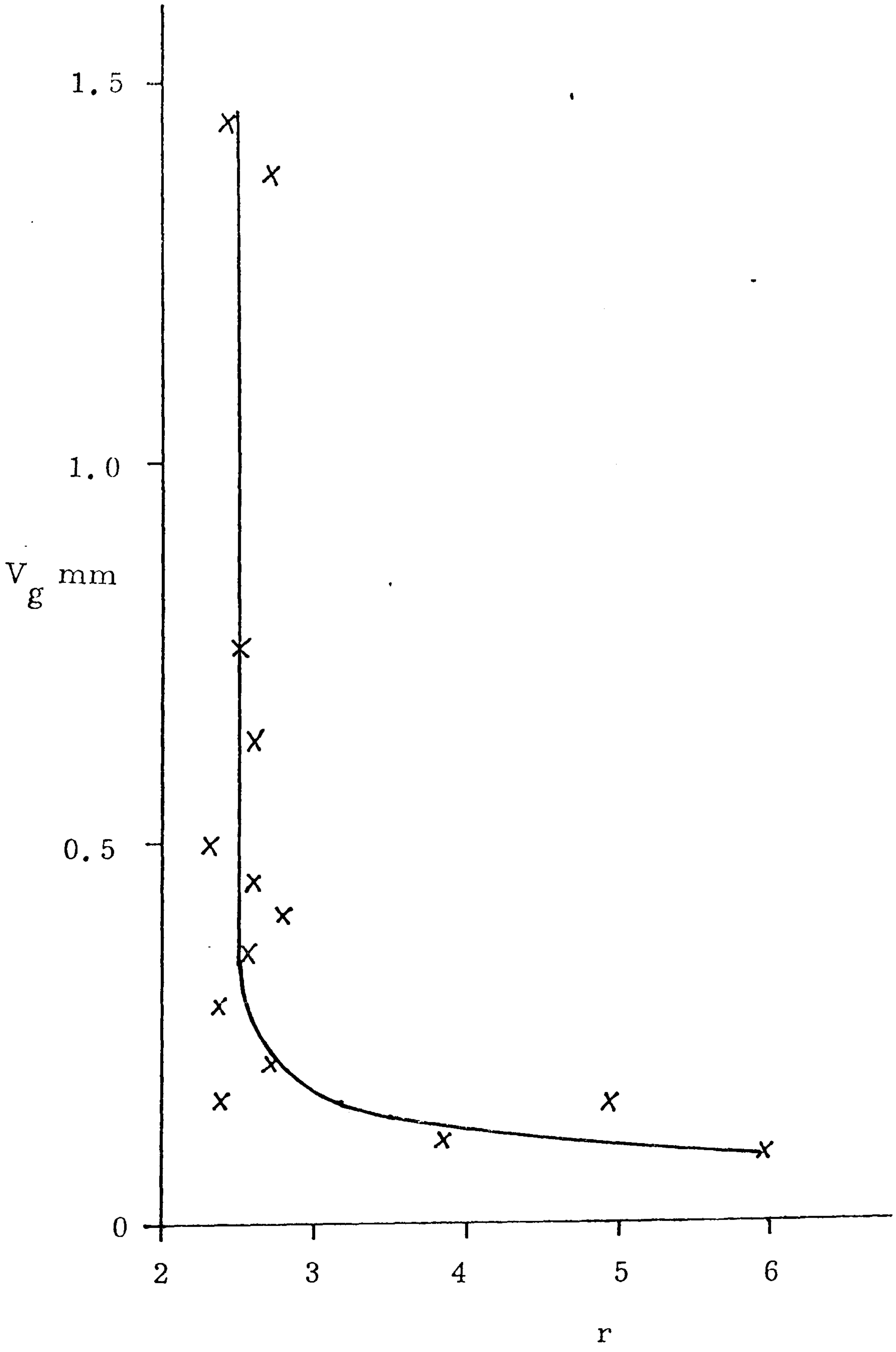

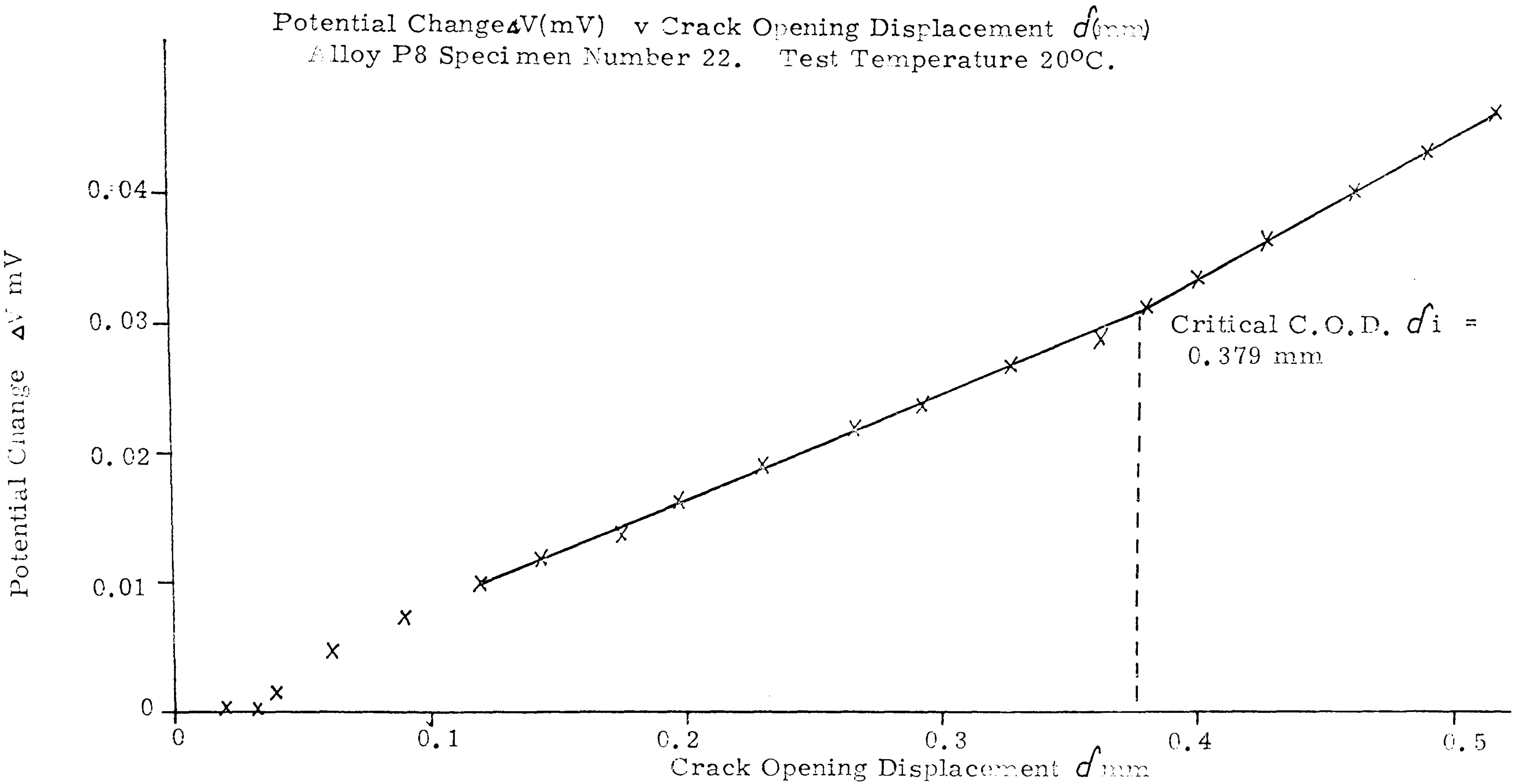

Potential Change ΔV(mV) v Crack Opening Displacement δ(mm)
Alloy P8 Specimen Number 22. Test Temperature 20°C.

FIGURE 25: TYPICAL CURVE SHOWING VARIATION OF POTENTIAL CHANGE WITH CRACK OPENING DISPLACEMENT (ALLOY P8, 20°C)

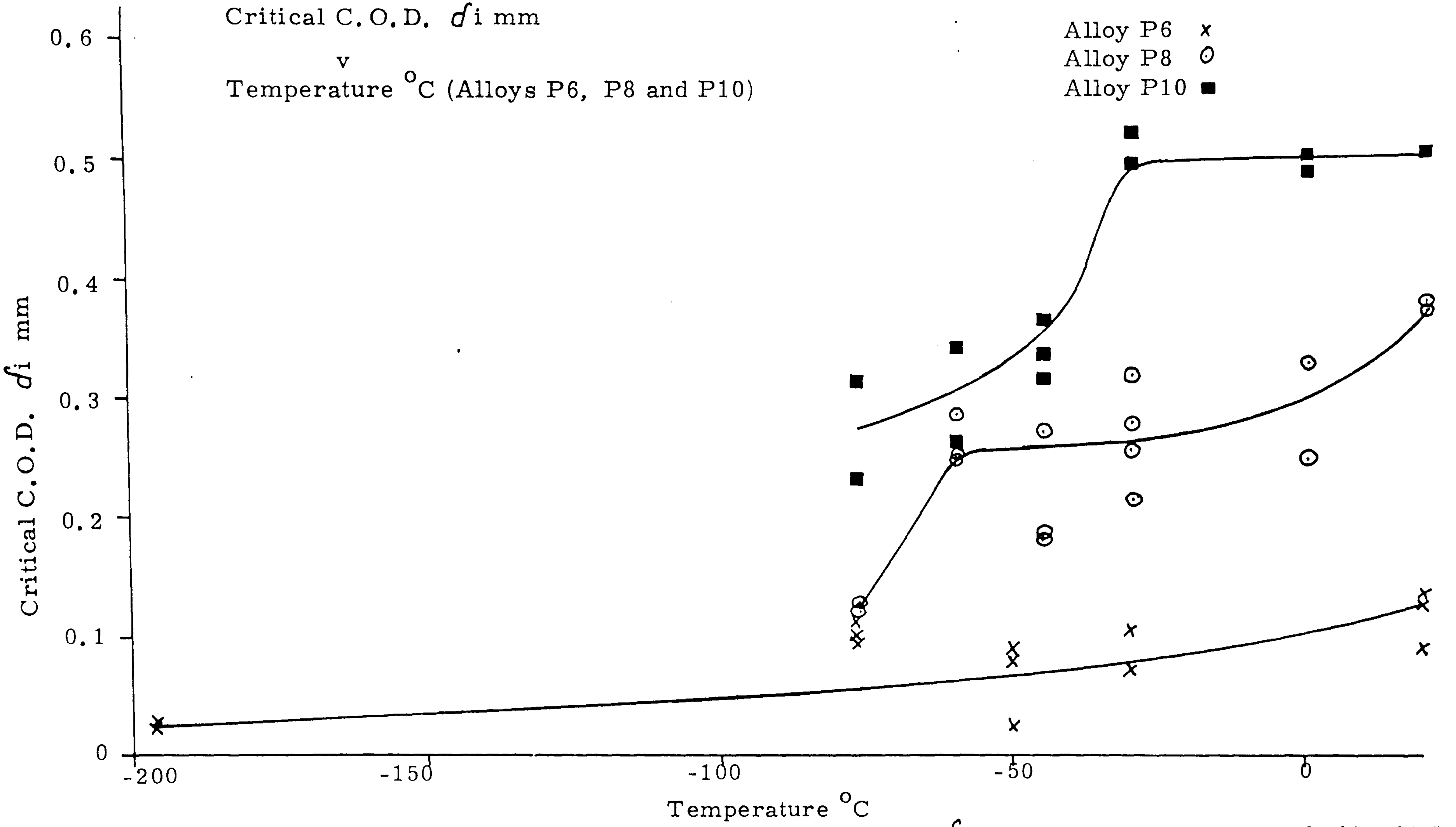

FIGURE 26: VARIATION OF CRITICAL COD δi WITH TEMPERATURE FOR ALLOYS P6, P8 AND P10

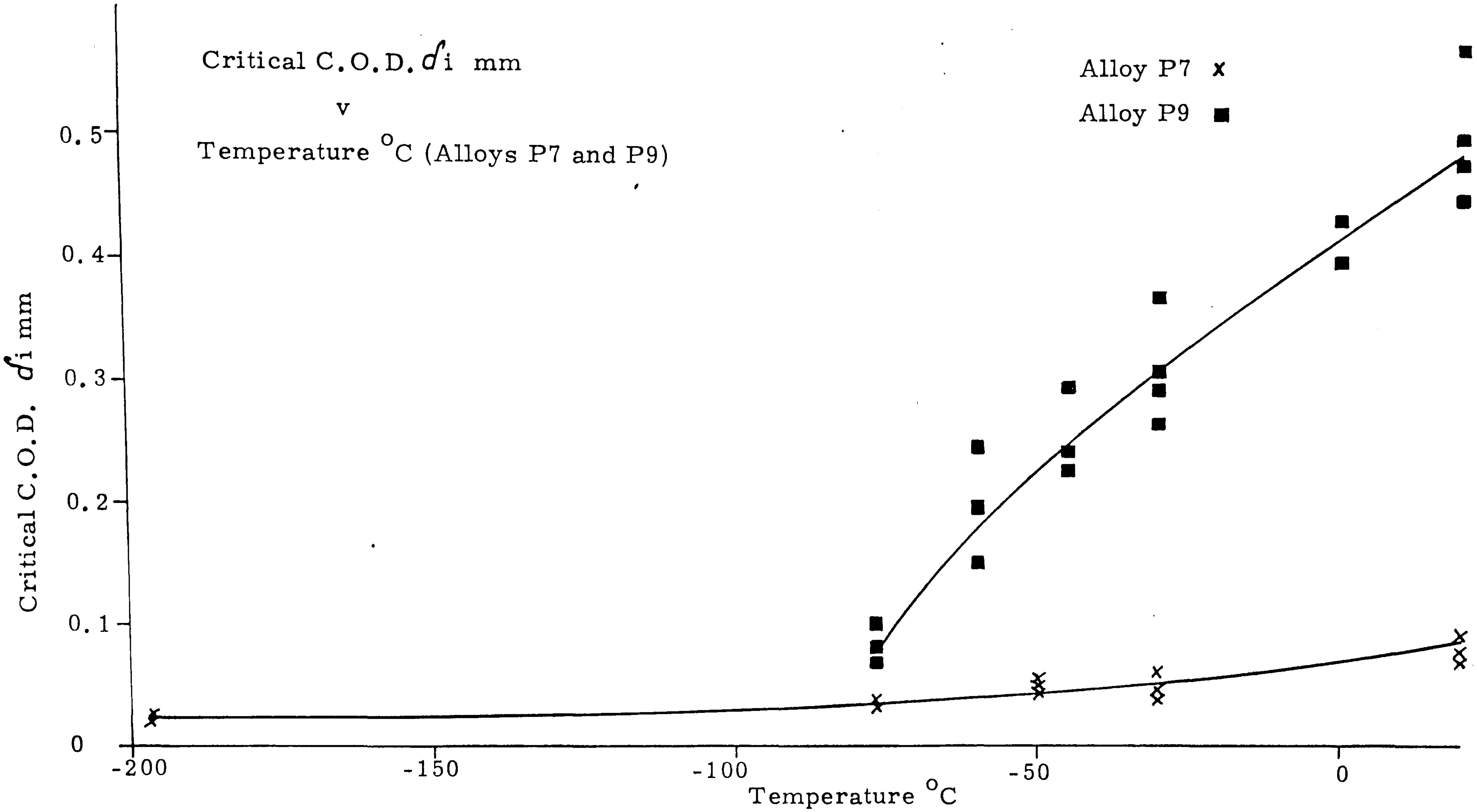

FIGURE 27: VARIATION OF CRITICAL C.O.D. δ_i WITH TEMPERATURE FOR ALLOYS P7 AND P9

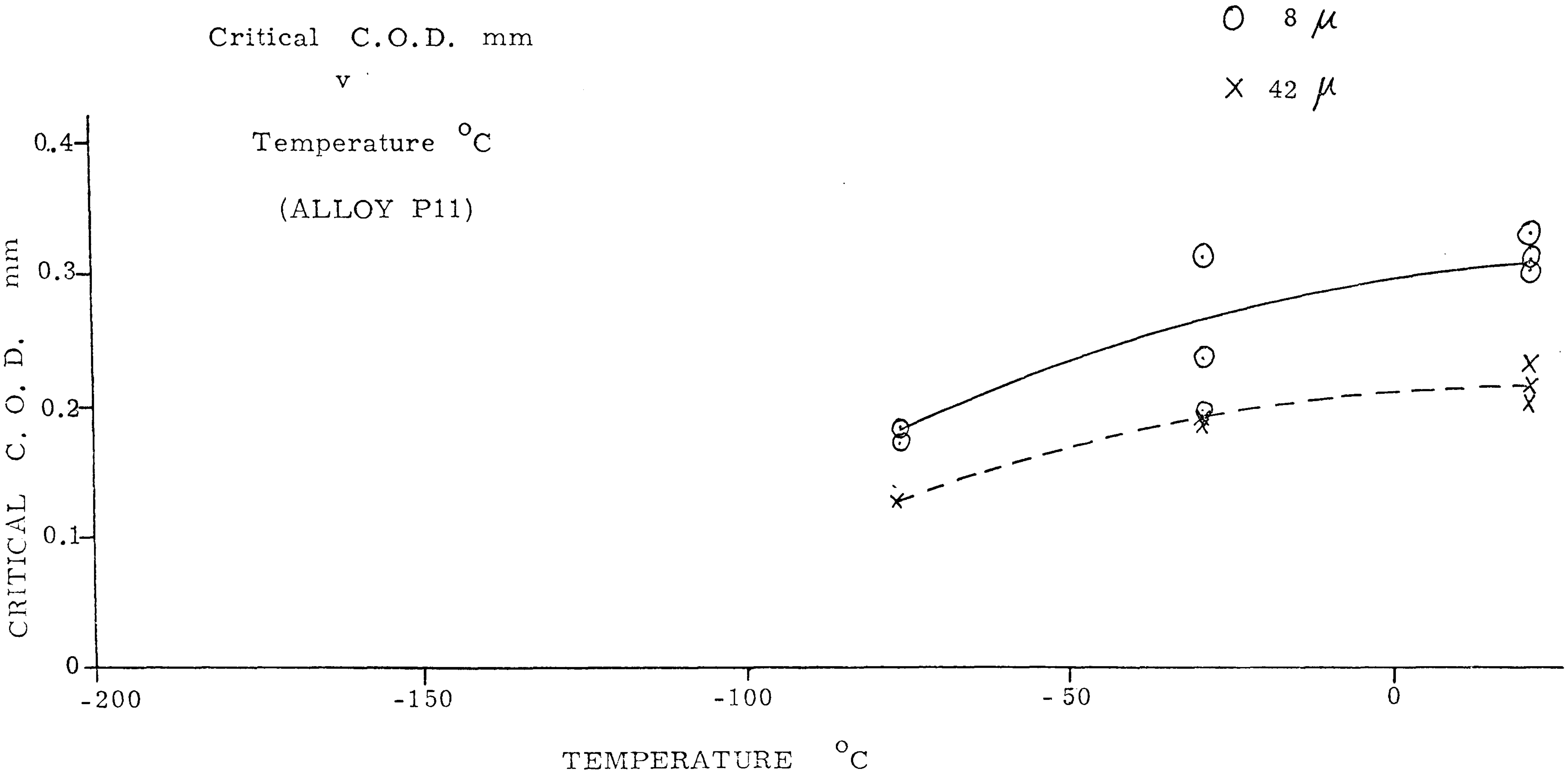

FIGURE 28 : VARIATION OF CRITICAL C.O.D. WITH TEMPERATURE FOR ALLOY P11

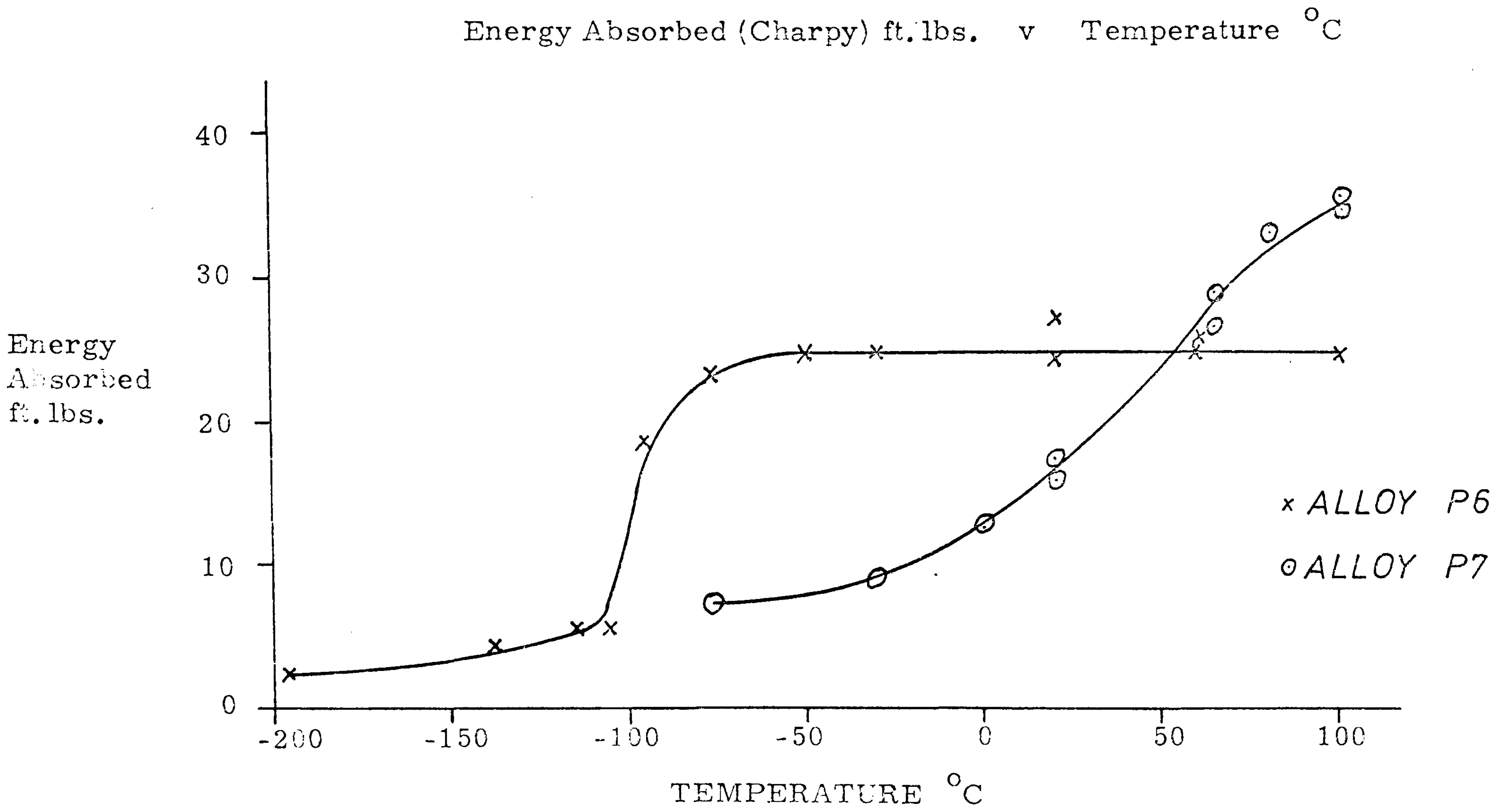

FIGURE 29(a): CHARPY IMPACT TEST RESULTS FOR ALLOYS P6 AND P7

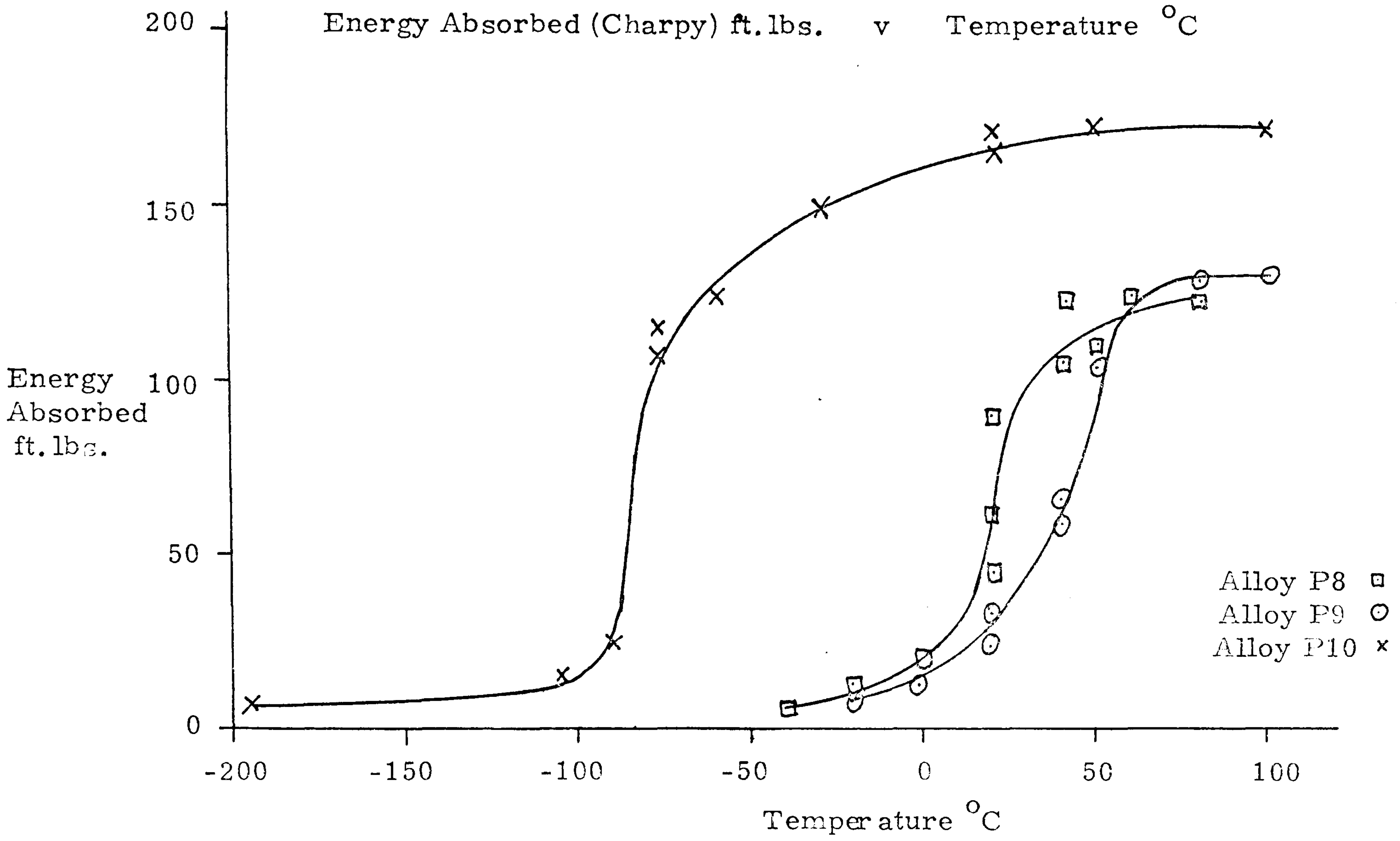

FIGURE 29(b): CHARPY IMPACT TEST RESULTS FOR ALLOYS P8, P9 AND P10

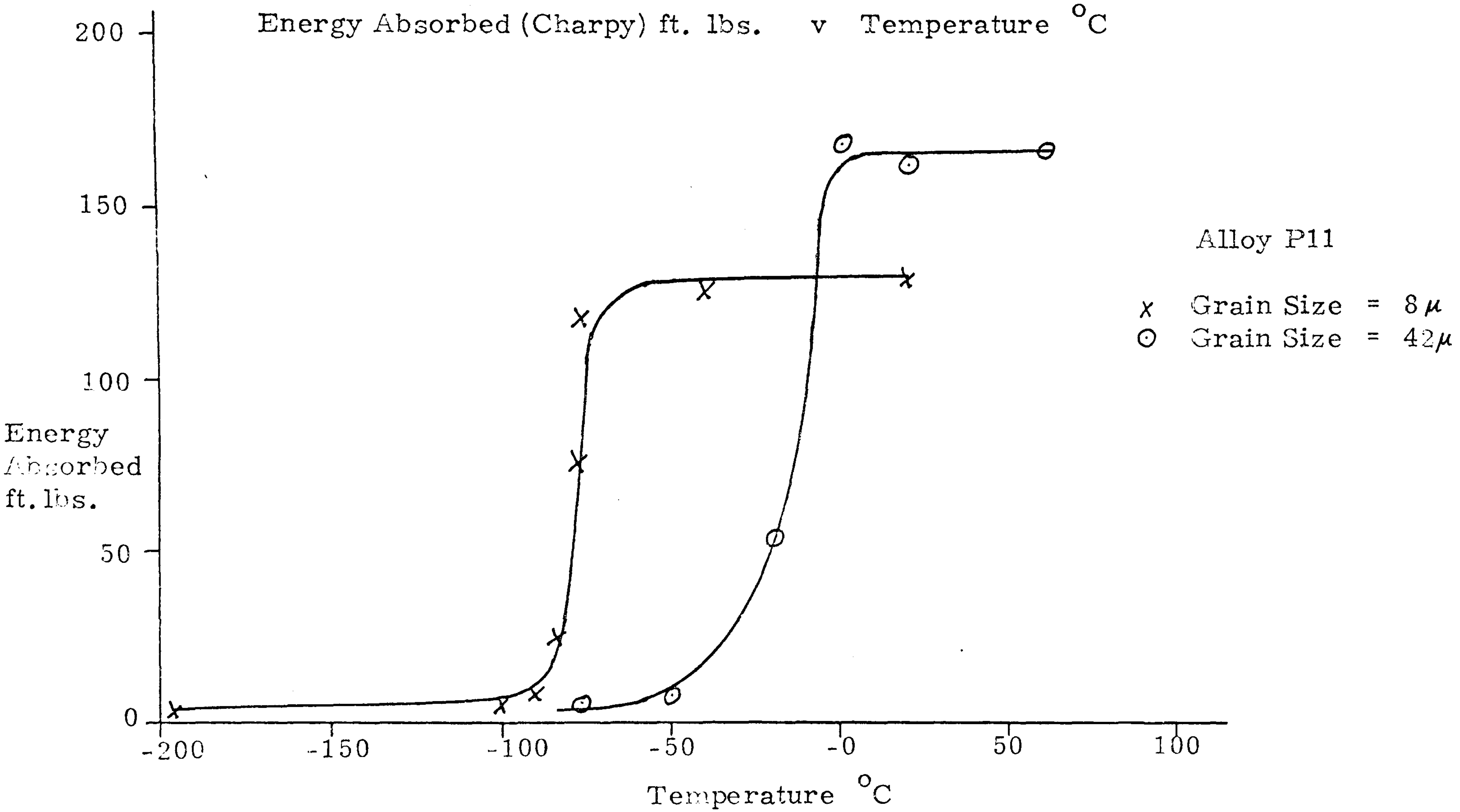

FIGURE 29(c): CHARPY IMPACT TEST RESULTS FOR ALLOY P11

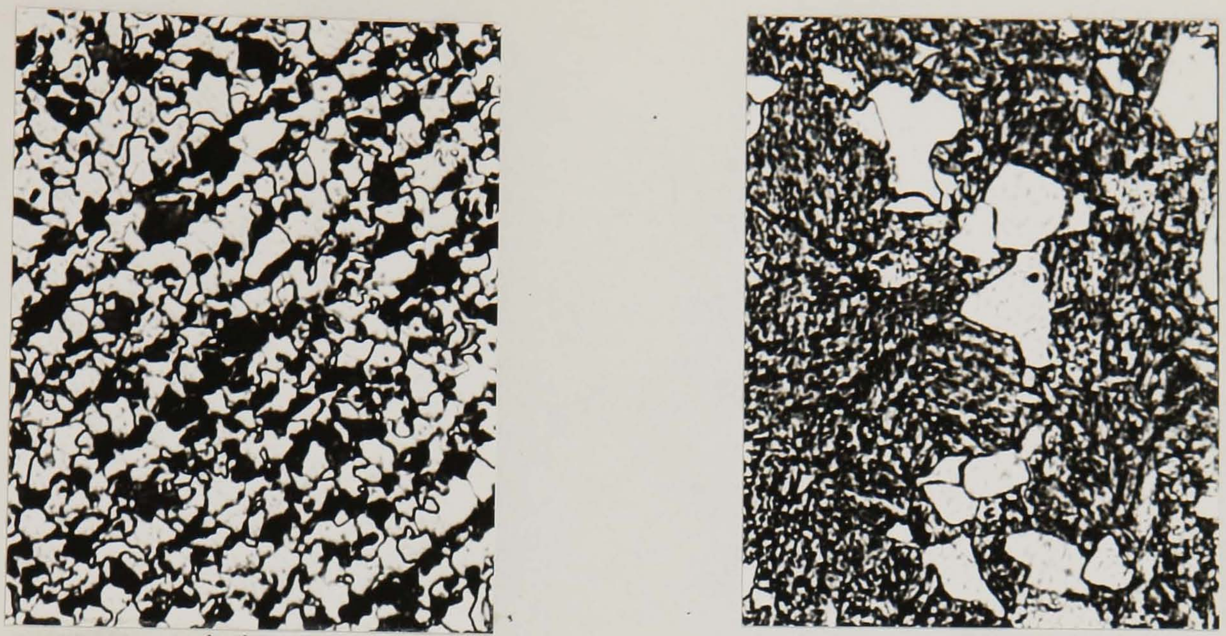

(a)
ALLOY P6 x 400
%PEARLITE = 40%

(b)
ALLOY P7 x 400

(c)
ALLOY P8 x 400
% PEARLITE = 15%

(d)
ALLOY P9 x 400
%PEARLITE = 20%

FIGURE 30 : PHOTOMICROGRAPHS OF ALLOYS USED IN THE PRESENT INVESTIGATION

(CONT.)

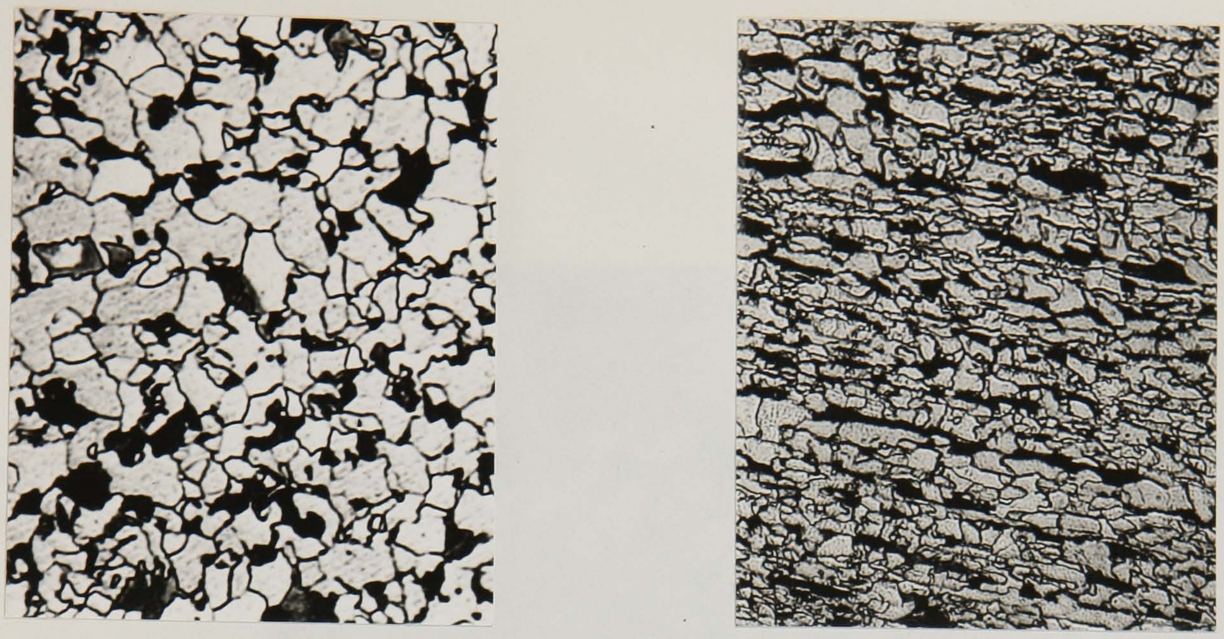

(e)

ALLOY P10 x 400
%PEARLITE = 15%

(f)

ALLOY P11 (8μ) x 200
% PEARLITE = 15%

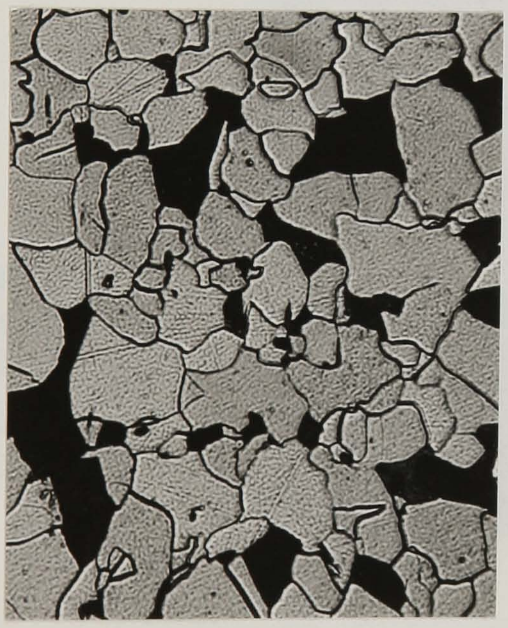

(g)

ALLOY P11 (42μ) x 200
% PEARLITE = 15%

FIGURE 30 (CONT.) : PHOTOMICROGRAPHS OF ALLOYS USED IN THE PRESENT INVESTIGATION

SLOW CRACK GROWTH

EXTENT OF SLOW CRACK GROWTH →

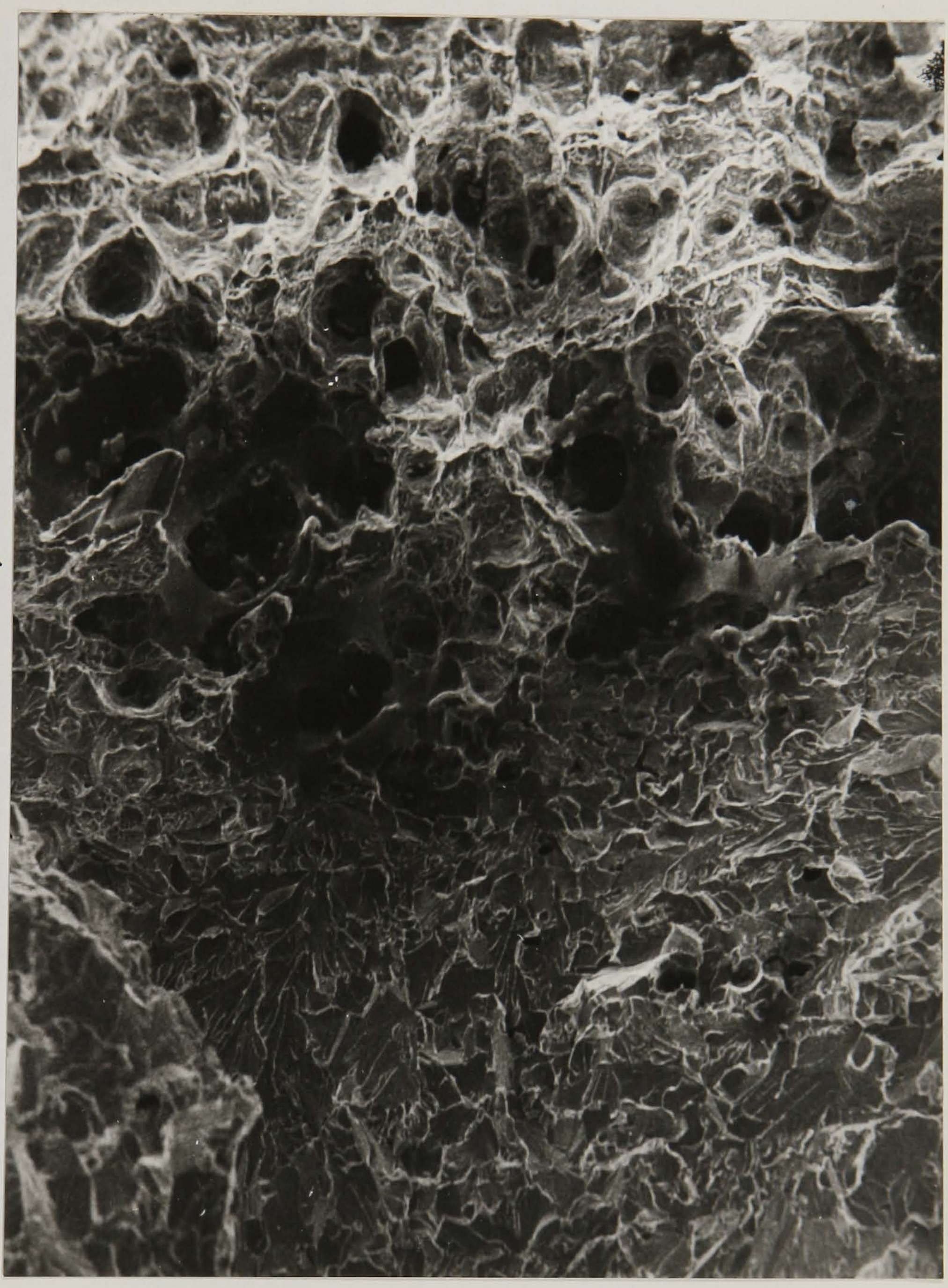

CLEAVAGE FRACTURE (PRODUCED BY COOLING IN LIQUID N_2)

x1K

FIGURE 31(a) : SCANNING ELECTRON MICROGRAPH OF FRACTURE SURFACE PRODUCED DURING C.O.D. TEST ON ALLOY P8 AT +20°C (SPECIMEN NO. P8, 22).

FATIGUE
CRACK GROWTH
REGION

SLOW CRACK
GROWTH REGION

CLEAVAGE
FRACTURE
REGION
FRACTURE
PRODUCED BY
COOLING IN
LIQUID N_2)

x1K

FIGURE 31(b) : SCANNING ELECTRON MICROGRPH OF FRACTURE SURFACE PRODUCED DURING C.O.D. TEST ON ALLOY P8 AT - 32 °C (SPECIMEN P8, 6).

x3K

FIGURE 31 (c) : SCANNING ELECTRON MICROGRAPH OF FRACTURE SURFACE PRODUCED DURING C$_{\delta}$O.D. TEST ON ALLOY P8 AT -77°C. THE MICROGRAPH ILLUSTRATES THE MIXED CLEAVAGE-DUCTILE FAILURE MODE.

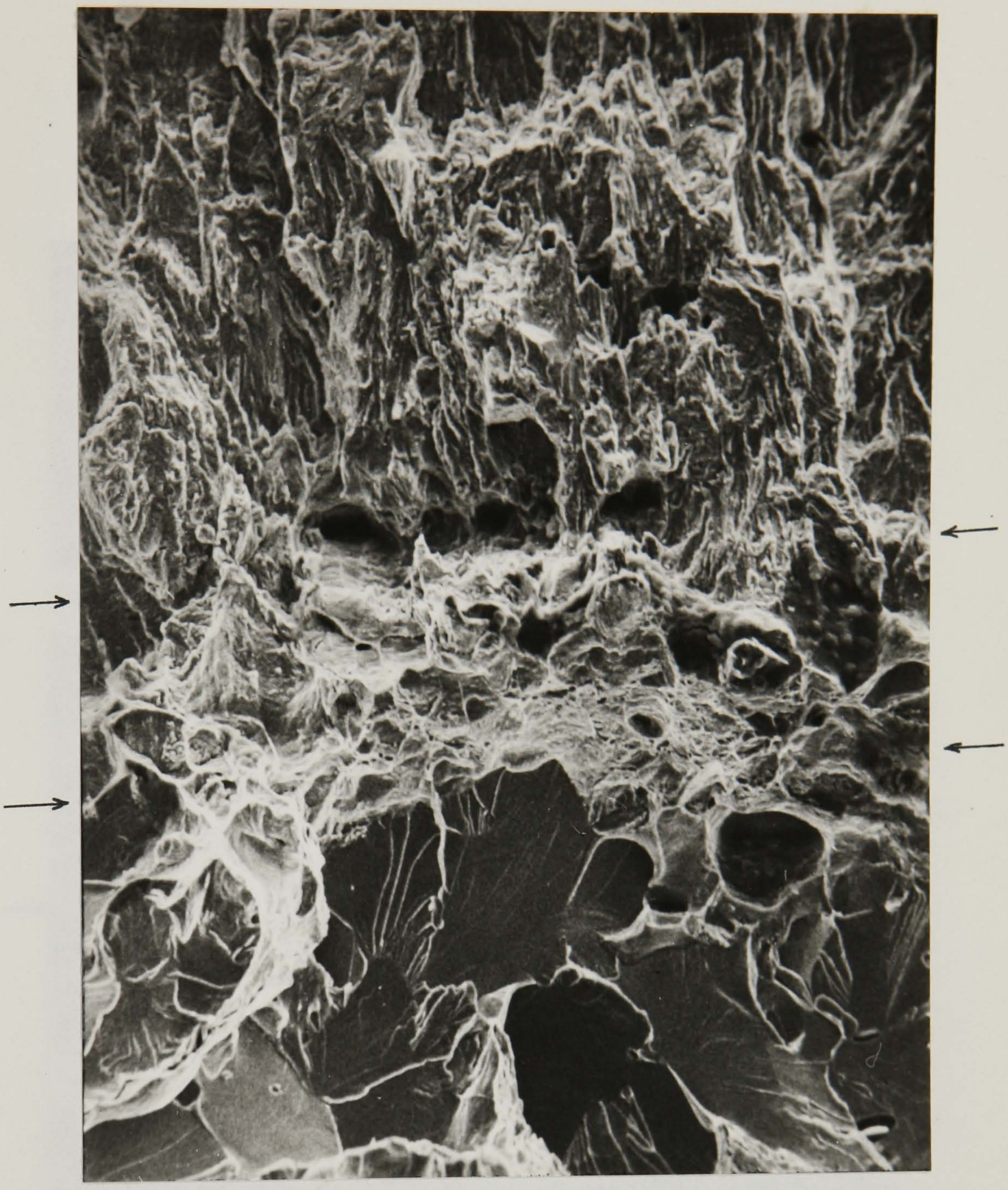

FATIGUE CRACK GROWTH REGION

SLOW CRACK GROWTH REGION

CLEAVAGE FRACTURE REGION (FRACTURE PRODUCED BY COOLING IN LIQUID N_2).

x1K

FIGURE 31 (d): SCANNING ELECTRON MICROGRAPH OF FRACTURE SURFACE PRODUCED DURING C$_{\delta}$O. D. TEST ON ALLOY P9 AT -60°C (SPECIMEN P9, 21).

FIGURE 31 (e) : SCANNING ELECTRON MICROGRAPH OF FRACTURE SURFACE PRODUCED DURING C.O.D. TEST ON ALLOY P9 AT -77°C (SPECIMEN P9, 23).

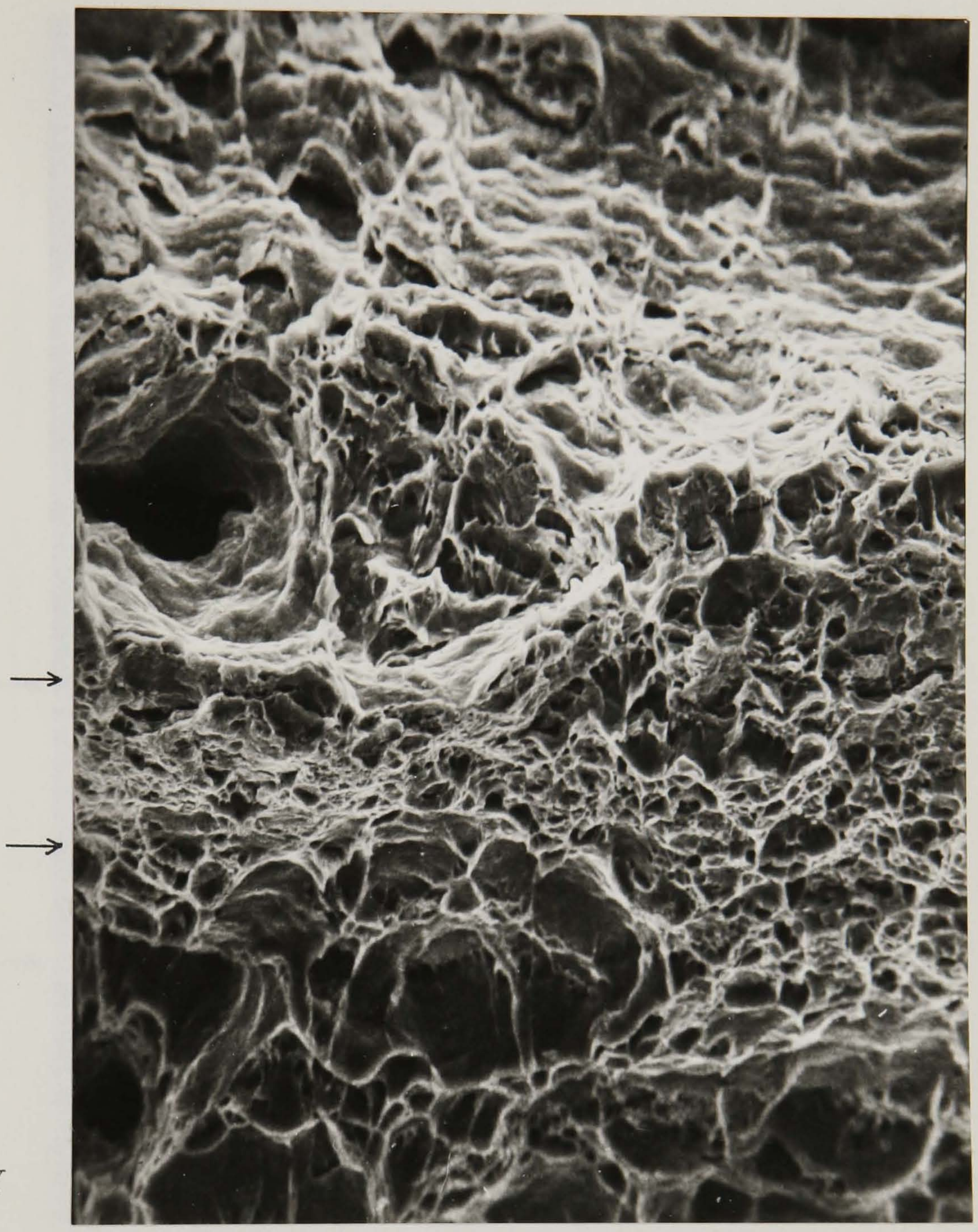

FIGURE 31(f) : SCANNING ELECTRON MICROGRAPH OF FRACTURE SURFACE PRODUCED DURING C.O.D. TEST ON ALLOY P10 AT + 20°C (SPECIMEN P10, 11)

FATIGUE CRACK GROWTH

SLOW CRACK GROWTH

CLEAVAGE FRACTURE REGION (FRACTURE PRODUCED BY COOLING IN LIQUID N_2)

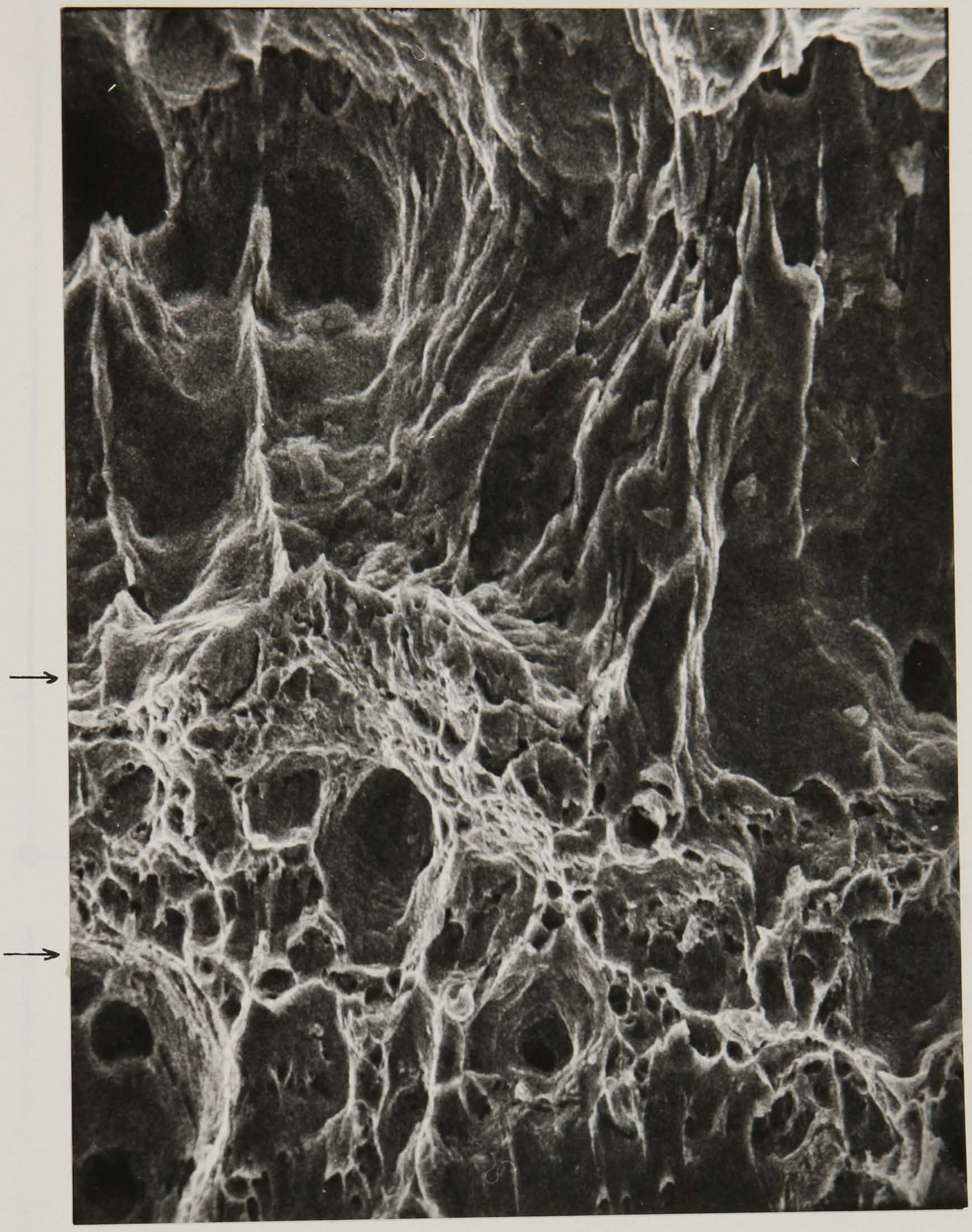

x100

FIGURE 31(g) : SCANNING ELECTRON MICROGRAPH OF FRACTURE SURFACE PRODUCED DURING C.O.D. TEST ON ALLOY P10 AT -77°C (SPECIMEN P10, 6)

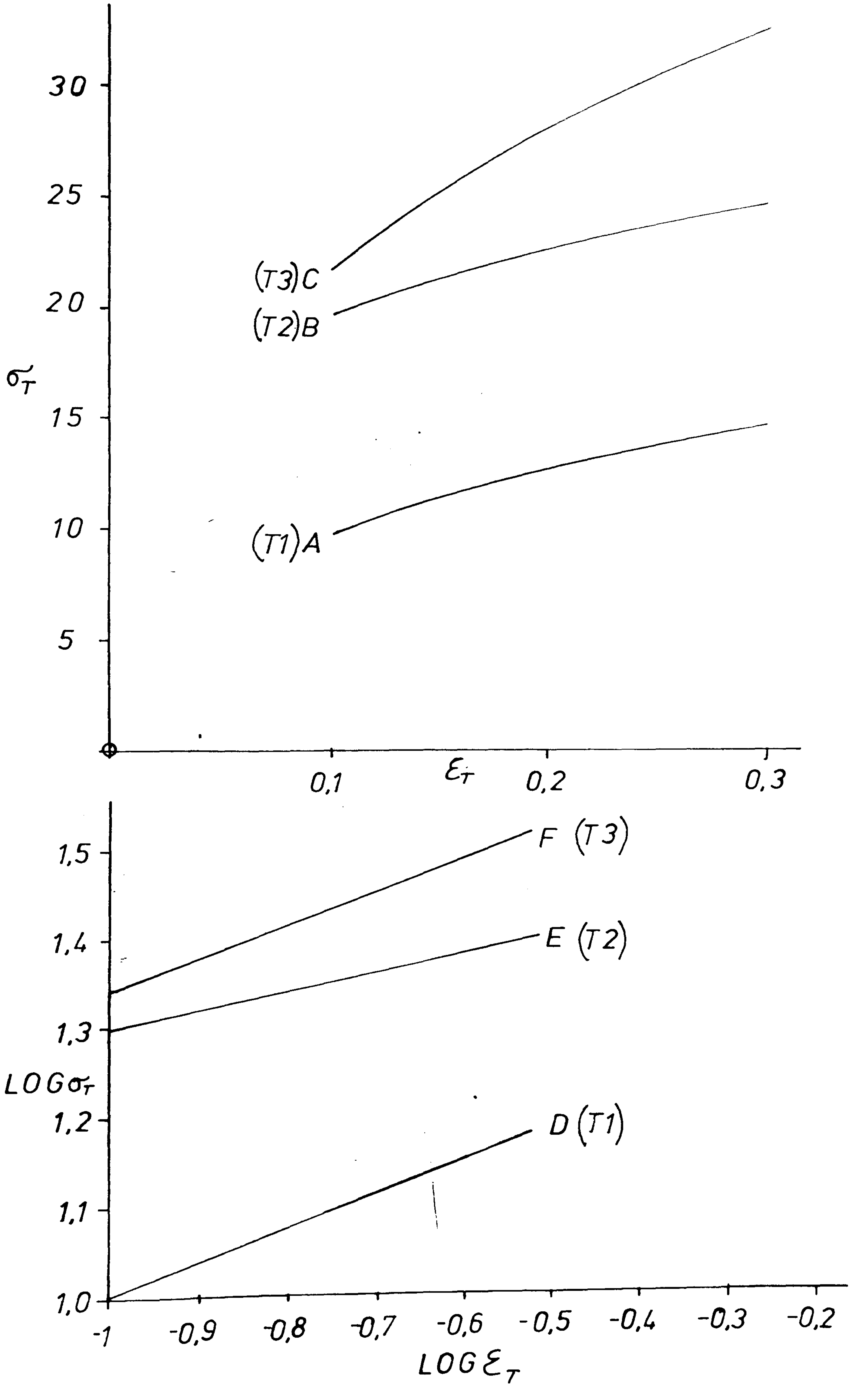

30
25
20
15
10
5
σ_T
(T3)C
(T2)B
(T1)A
0,1
ε_T
0,2
0,3
1,5
1,4
1,3
LOGσ_T
1,2
1,1
1,0
F (T3)
E (T2)
D (T1)
-1
-0,9
-0,8
-0,7
-0,6
-0,5
-0,4
-0,3
-0,2
LOG ε_T

FIGURE 32.

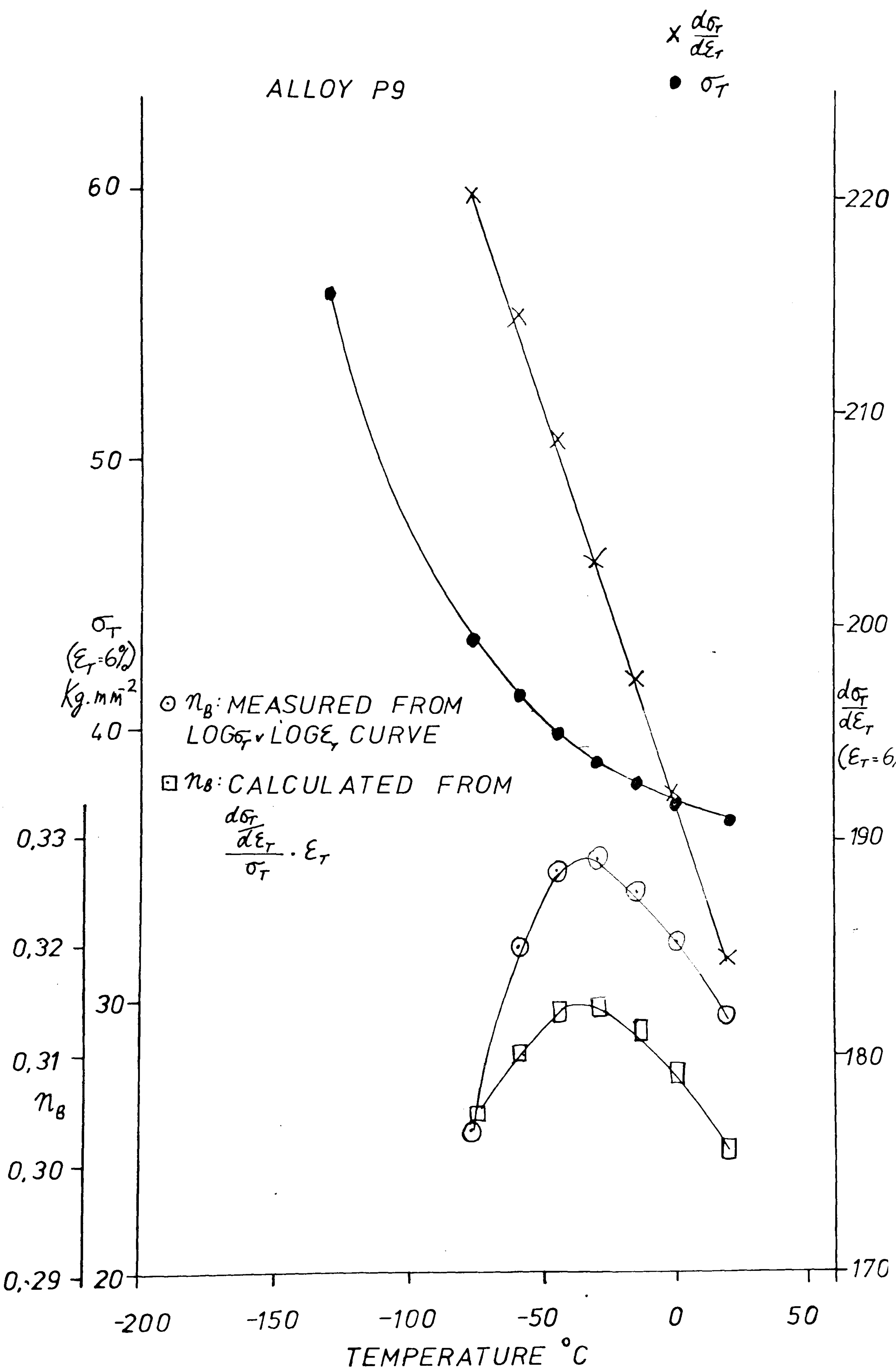
ALLOY P9
× $\frac{d\sigma_T}{d\varepsilon_T}$
● σ_T
σ_T (ε_T=6%) Kg.mm^{-2}
60
50
40
30
20
0,33
0,32
0,31
0,30
0,29
n_B
$\frac{d\sigma_T}{d\varepsilon_T}$ (ε_T=6
220
210
200
190
180
170
⊙ n_B: MEASURED FROM LOGσ_T v LOGε_T CURVE
⊡ n_B: CALCULATED FROM $\frac{\frac{d\sigma_T}{d\varepsilon_T}}{\sigma_T} \cdot \varepsilon_T$
-200
-150
-100
-50
0
50
TEMPERATURE °C

FIGURE 33(a)

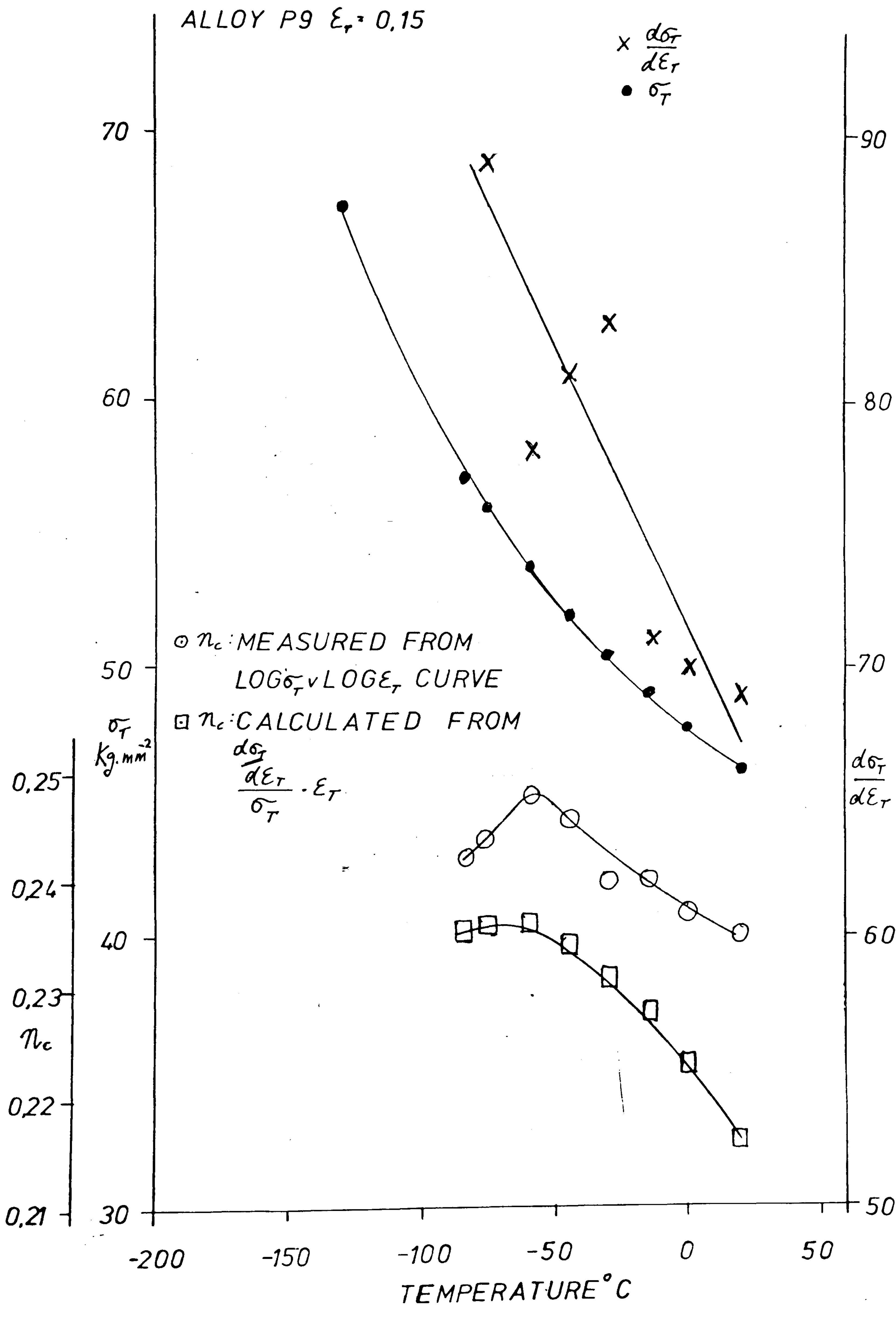
ALLOY P9 $\varepsilon_T = 0,15$
× $\frac{d\sigma_T}{d\varepsilon_T}$
● σ_T
⊙ n_c : MEASURED FROM
LOG σ_T v LOG ε_T CURVE
⊡ n_c : CALCULATED FROM
$\frac{\frac{d\sigma_T}{d\varepsilon_T}}{\sigma_T} \cdot \varepsilon_T$
σ_T Kg.mm^{-2}
n_c
$\frac{d\sigma_T}{d\varepsilon_T}$
70
60
50
40
30
0,25
0,24
0,23
0,22
0,21
90
80
70
60
50
-200
-150
-100
-50
0
50
TEMPERATURE °C

FIGURE 33(b)

FIGURE 34: LOG TRUE STRESS ($Ln\sigma_T$) v LOG TRUE STRAIN ($Ln\,\varepsilon_T$). ALLOY P6 (- 10°C)

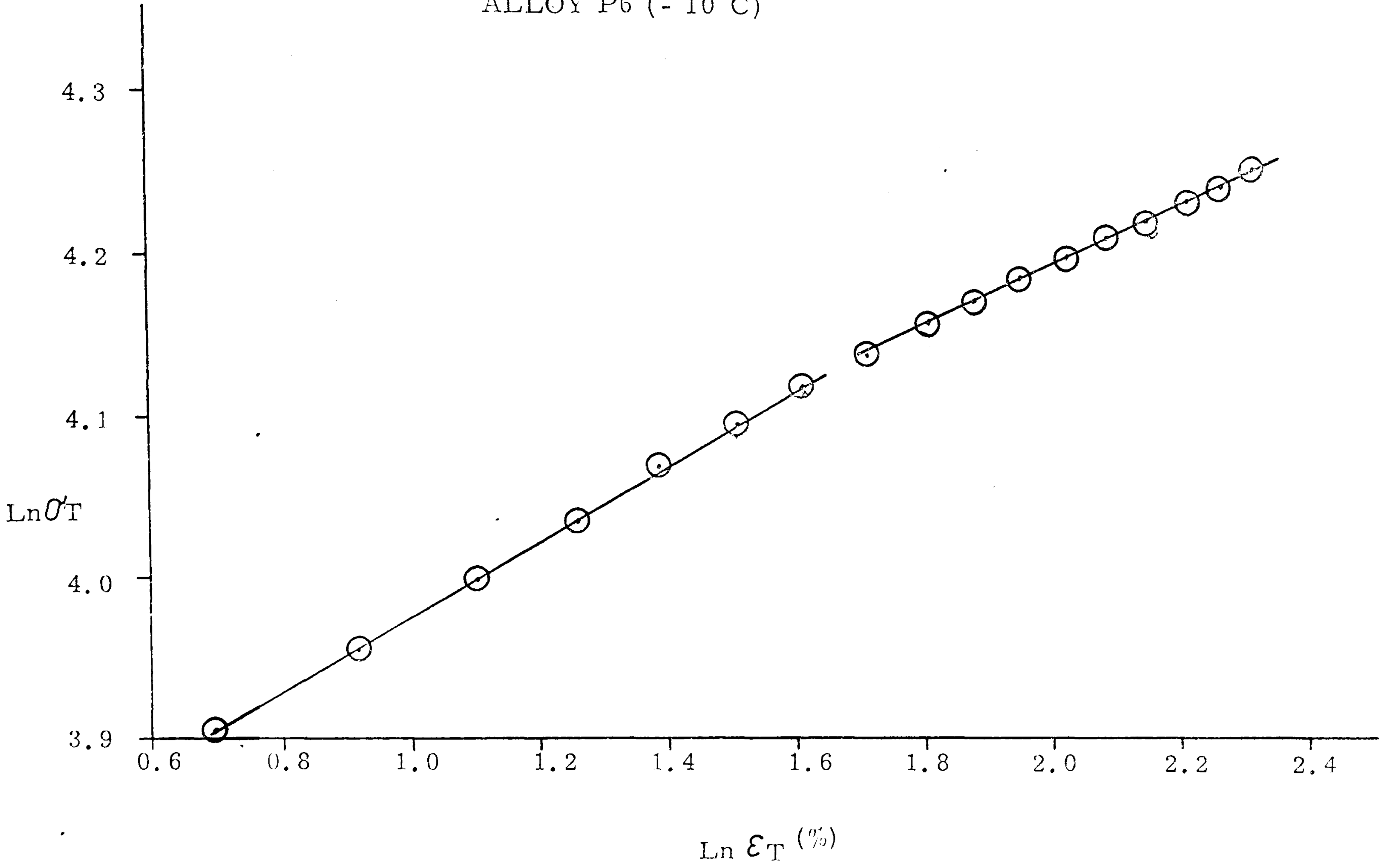

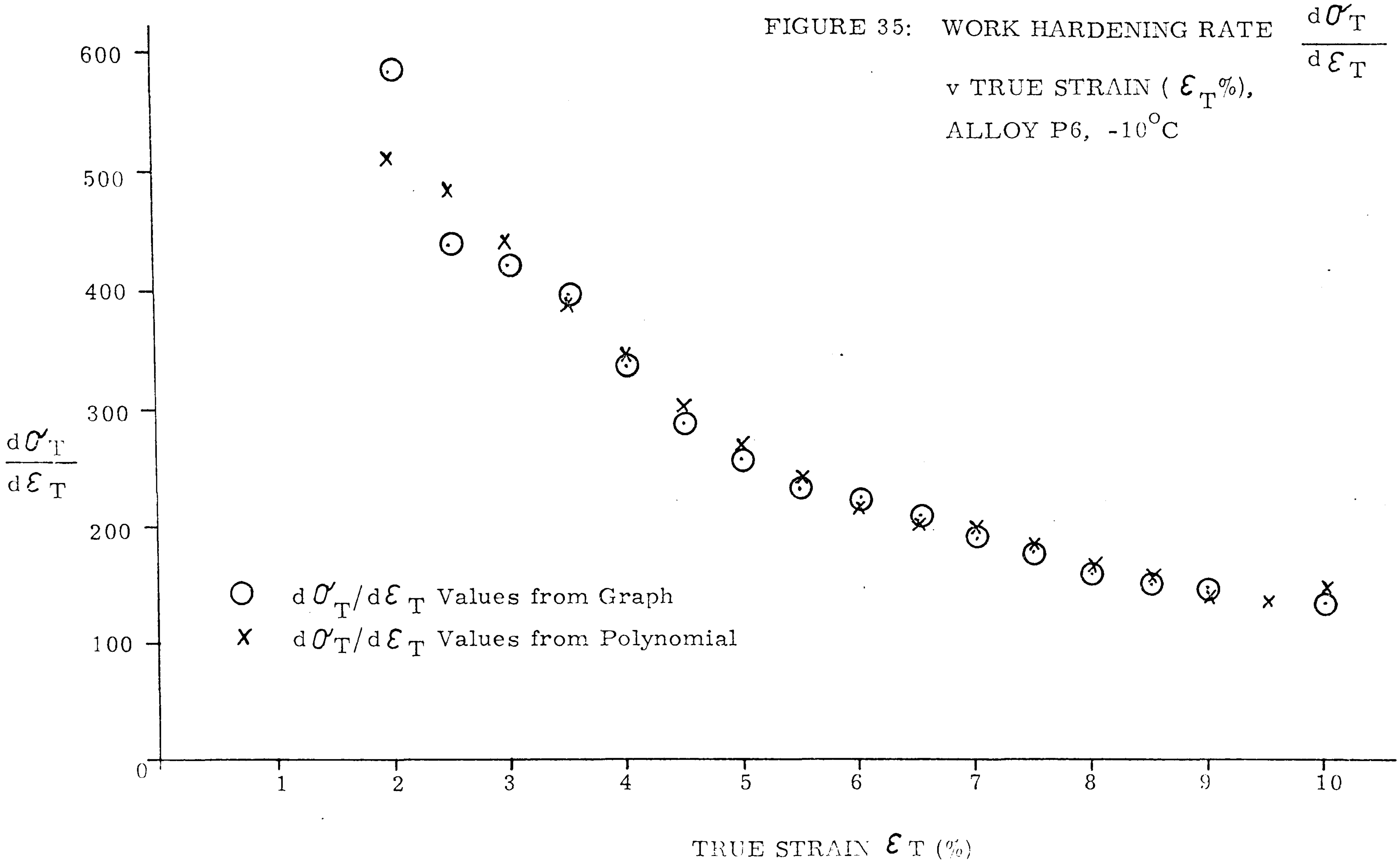

FIGURE 35: WORK HARDENING RATE $\frac{d\sigma_T}{d\varepsilon_T}$ v TRUE STRAIN (ε_T%), ALLOY P6, -10°C

FIGURE 36: MEASURED Ln $\frac{d\sigma_T}{d\varepsilon_T}$ VALUES v Ln ε_T (%)

ALLOY P6, -10°C

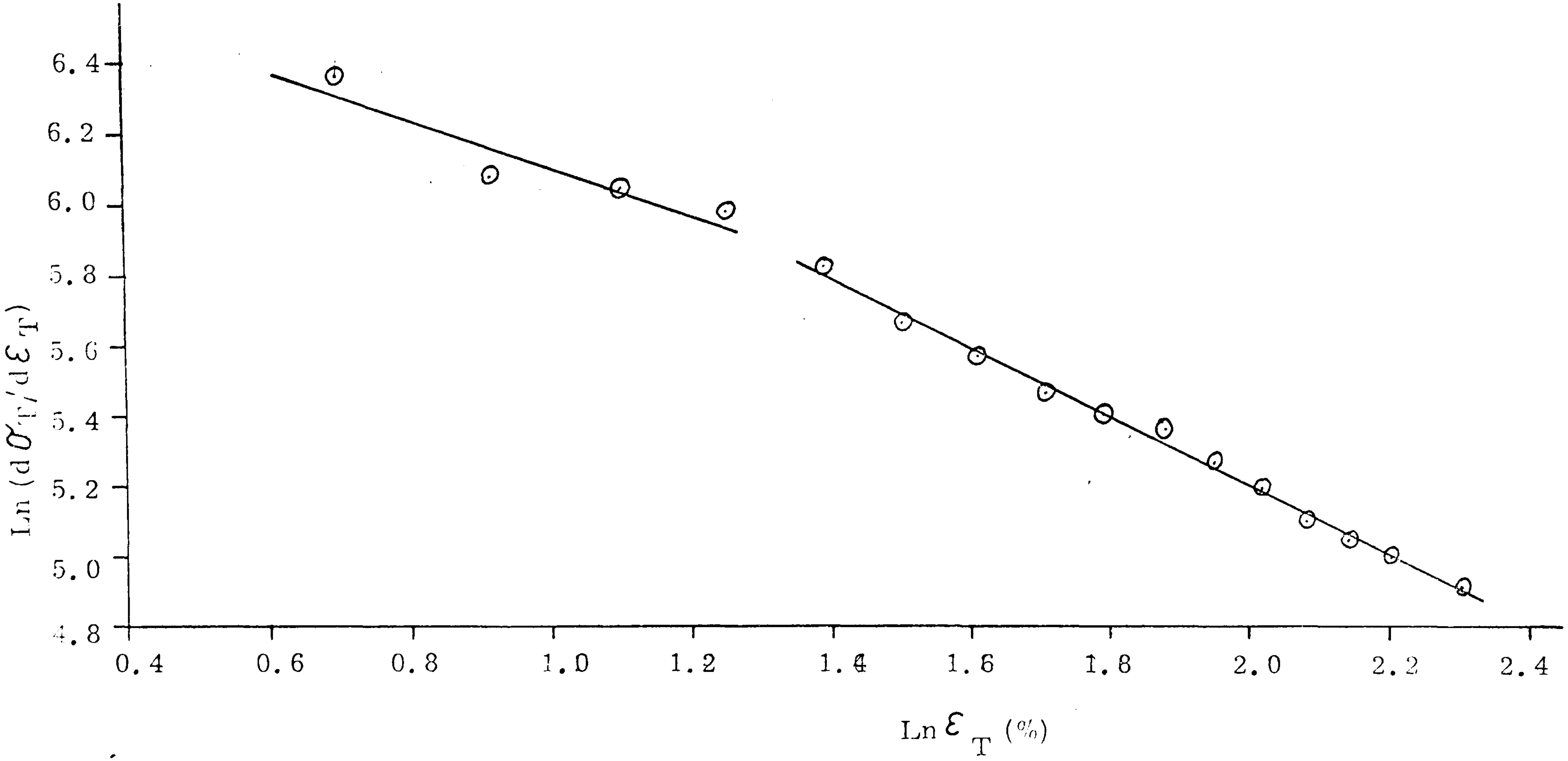

FIGURE 37: Ln $\frac{d\sigma_T}{d\varepsilon_T}$ VALUES DERIVED FROM POLYNOMIAL DIFFERENTATION

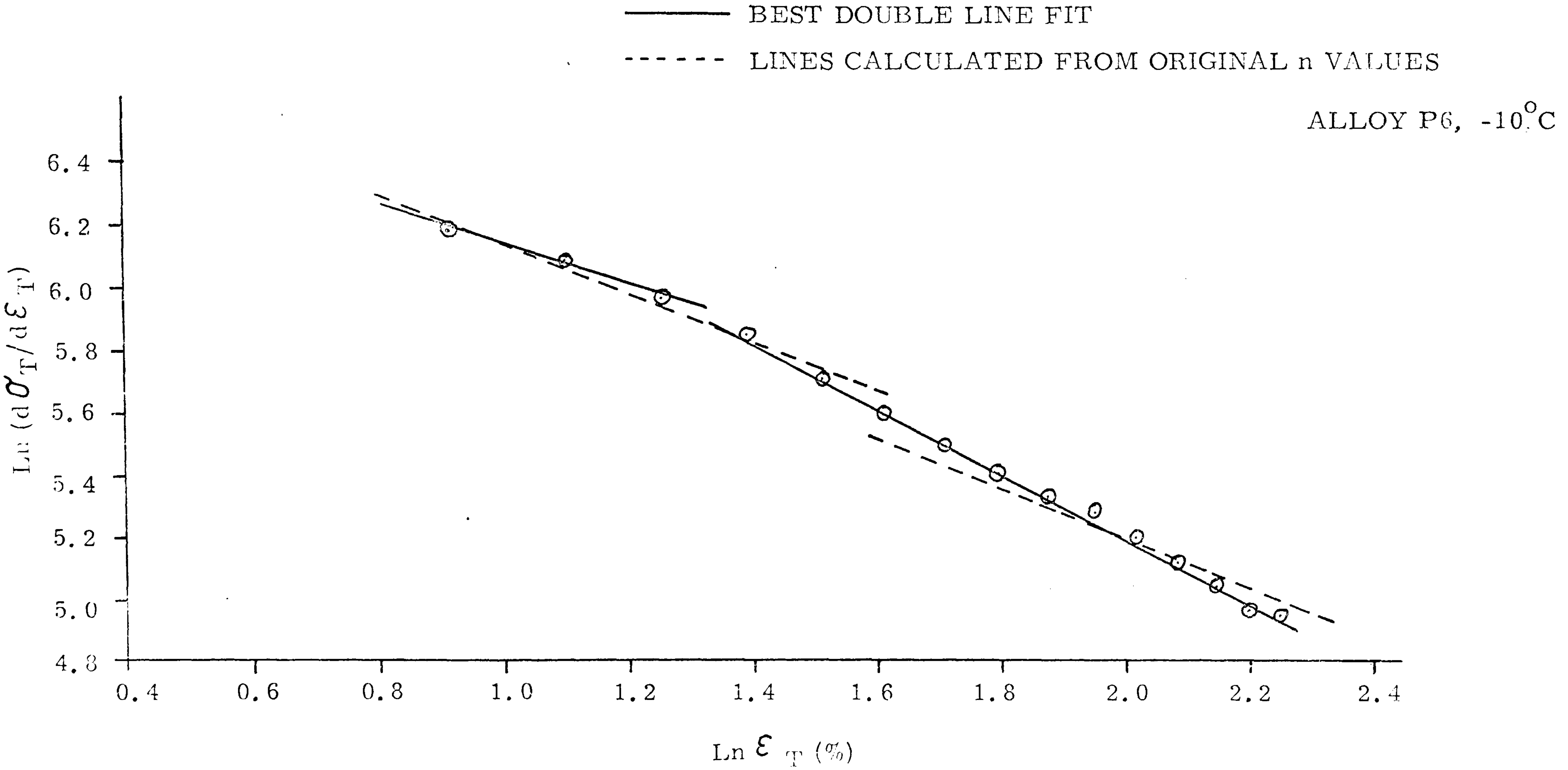

FIGURE 38: VARIATION OF WORK HARDENING RATE $\frac{d\sigma'_T}{d\varepsilon_T}$ WITH STRAIN (ε_T) FOR VARIOUS TEST TEMPERATURES

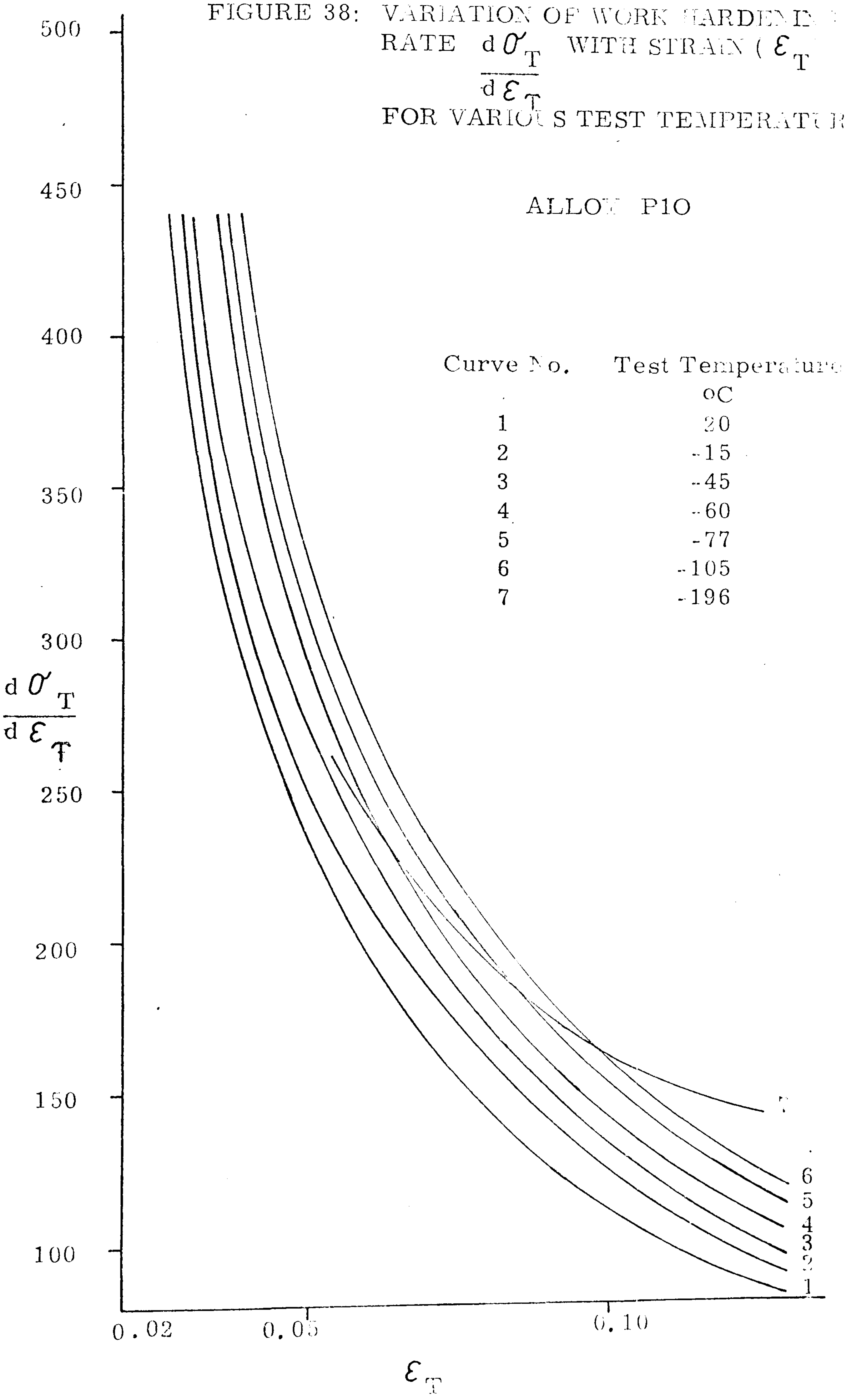

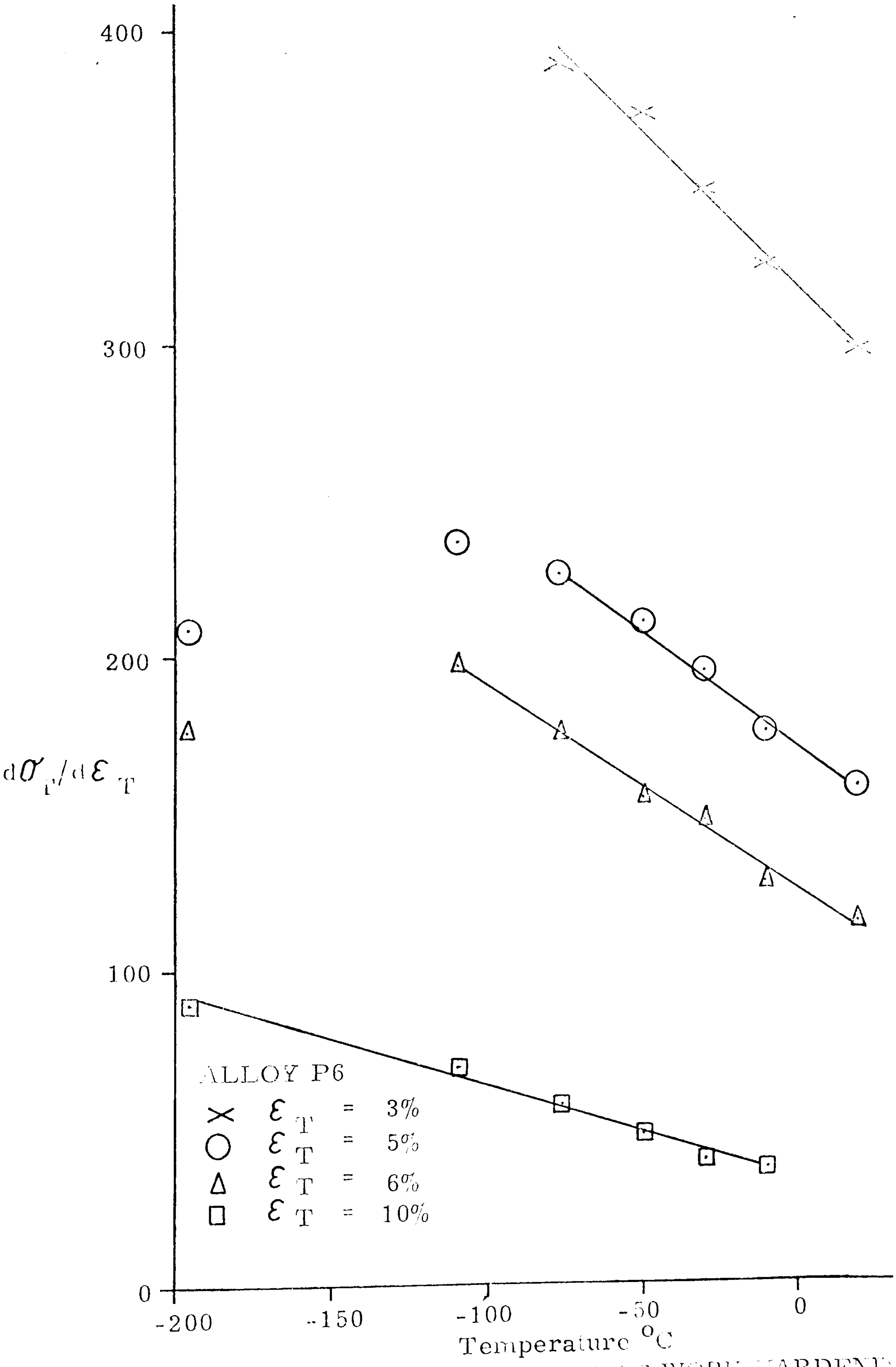

FIGURE 39(a): VARIATION OF WORK HARDENING RATE ($d\sigma_T/d\varepsilon_T$) W.R.T. TEMPERATURE (°C) FOR VARIOUS VALUES OF ε_T

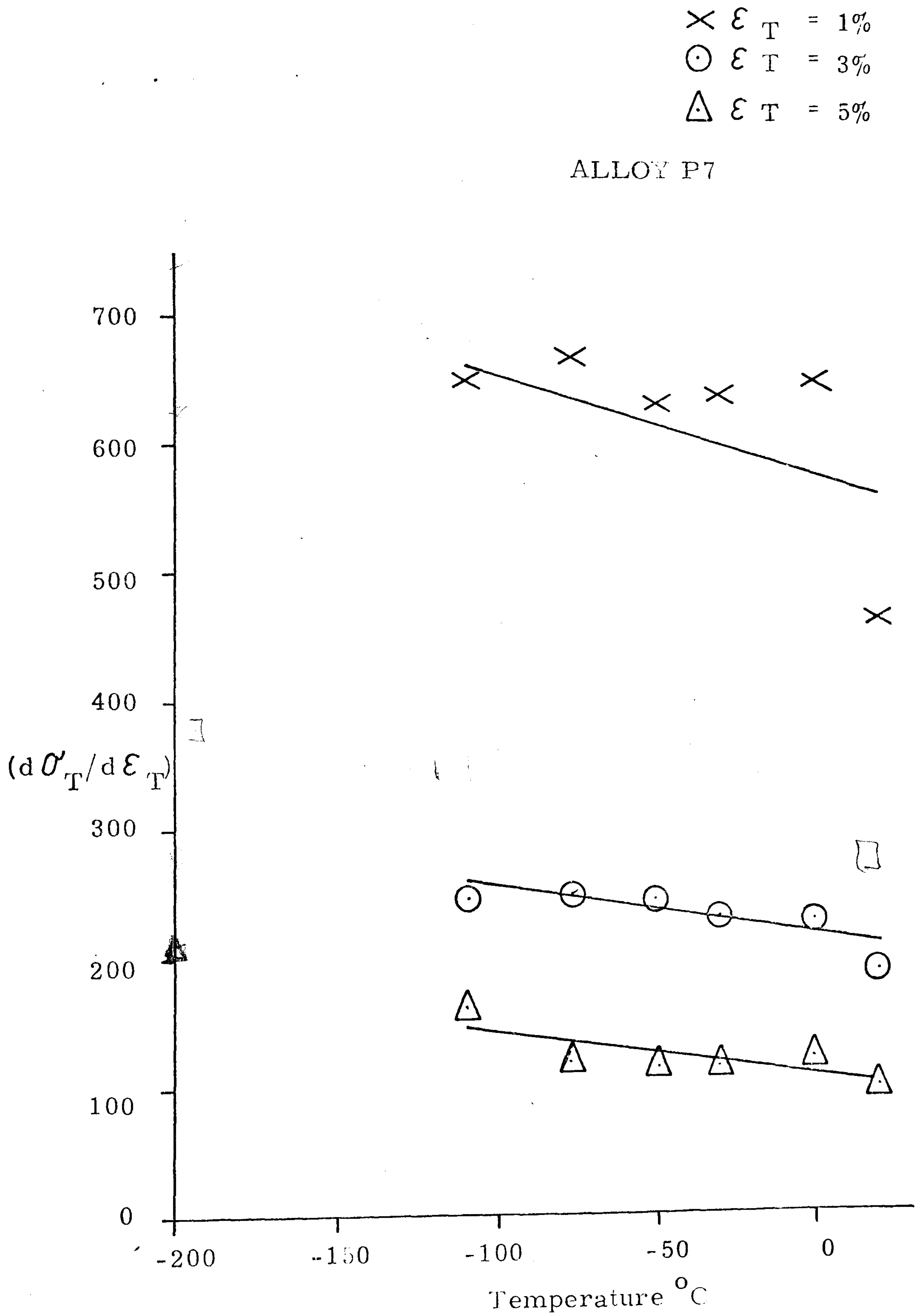

FIGURE 39(b): VARIATION OF WORK HARDENING RATE ($d\sigma_T/d\varepsilon_T$) WITH TEMPERATURE (°C) FOR VARIOUS VALUES OF ε_T

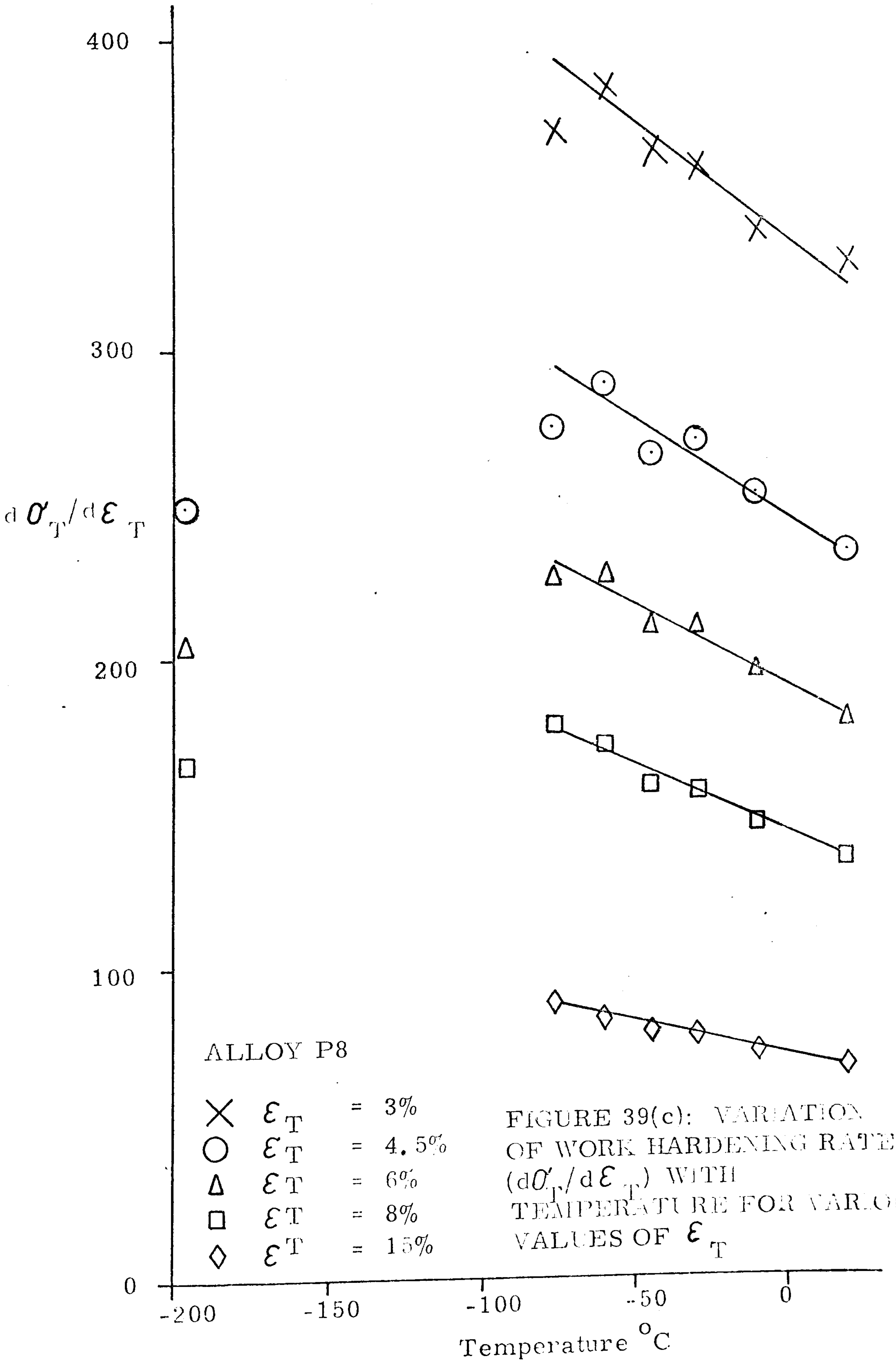

FIGURE 39(c): VARIATION OF WORK HARDENING RATE ($d\sigma_T/d\varepsilon_T$) WITH TEMPERATURE FOR VARIOUS VALUES OF ε_T

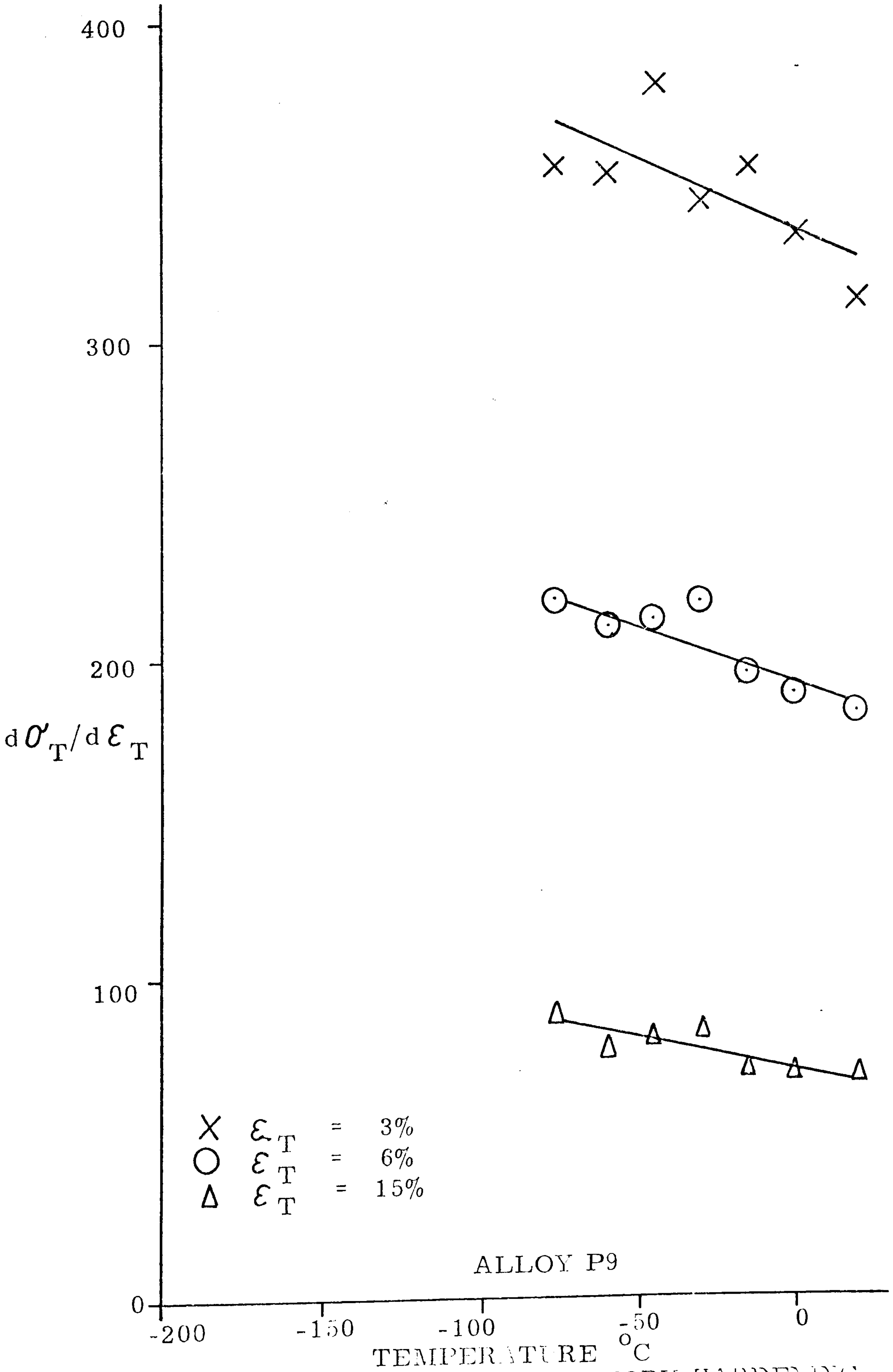

FIGURE 39(d): VARIATION OF WORK HARDENING RATE ($d\sigma'_T/d\varepsilon_T$) WITH TEMPERATURE FOR VARIOUS VALUES OF ε_T

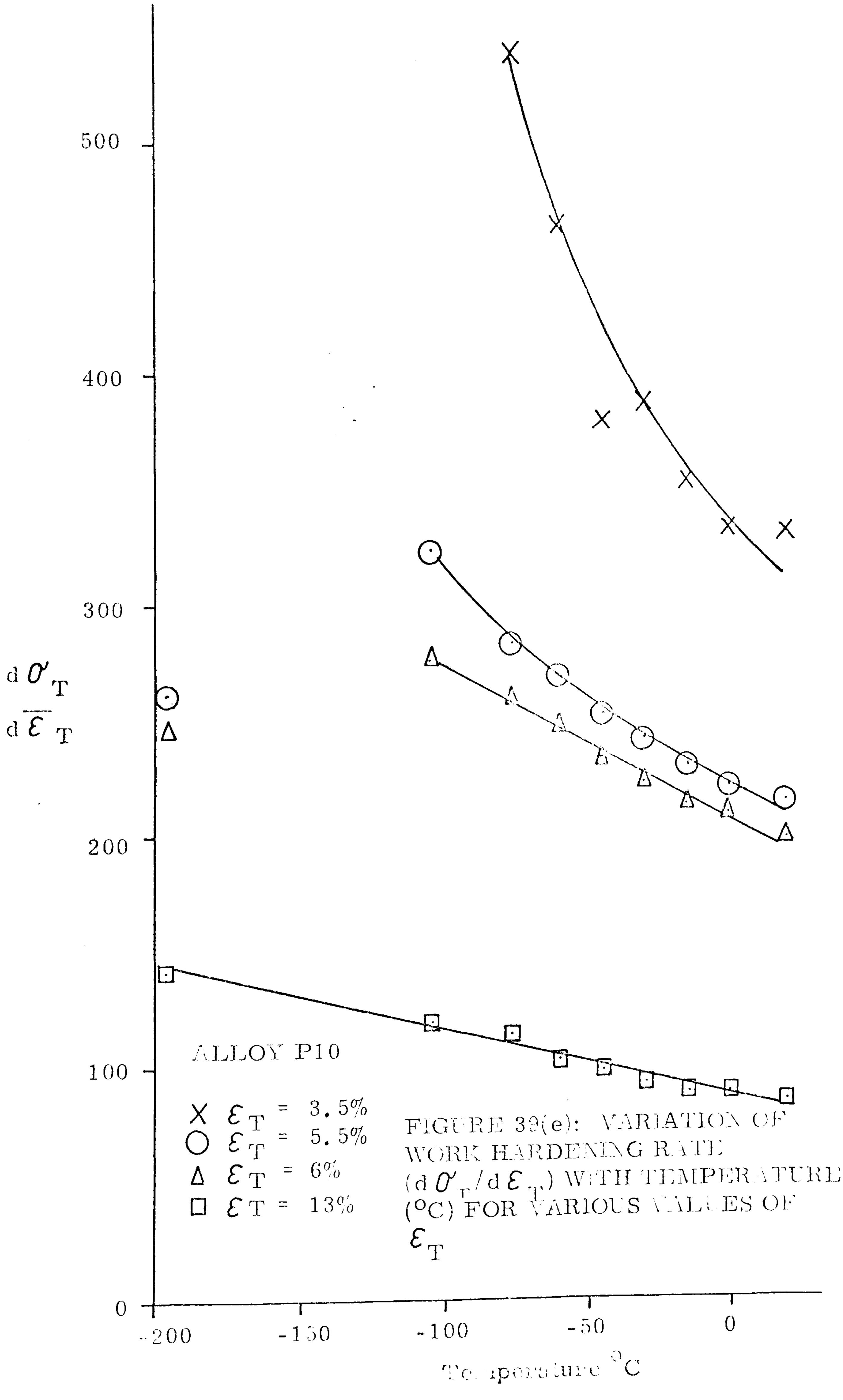

FIGURE 39(e): VARIATION OF WORK HARDENING RATE ($d\sigma'_T/d\varepsilon_T$) WITH TEMPERATURE (°C) FOR VARIOUS VALUES OF ε_T

FIGURE 40: STRAIN HARDENING EXPONENT (n) v PLASTIC INSTABILITY STRAIN (ε_{PI}), ALLOY P10

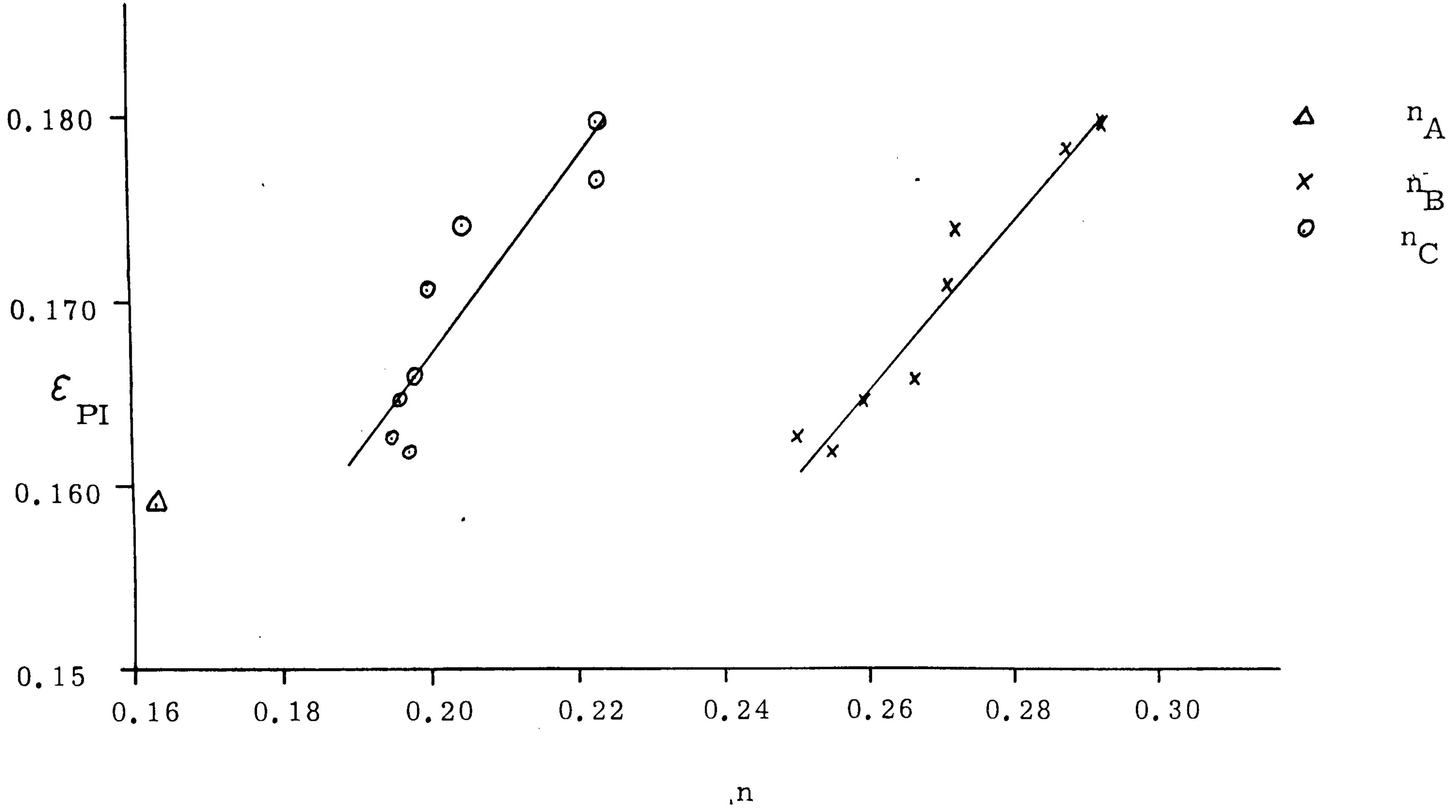

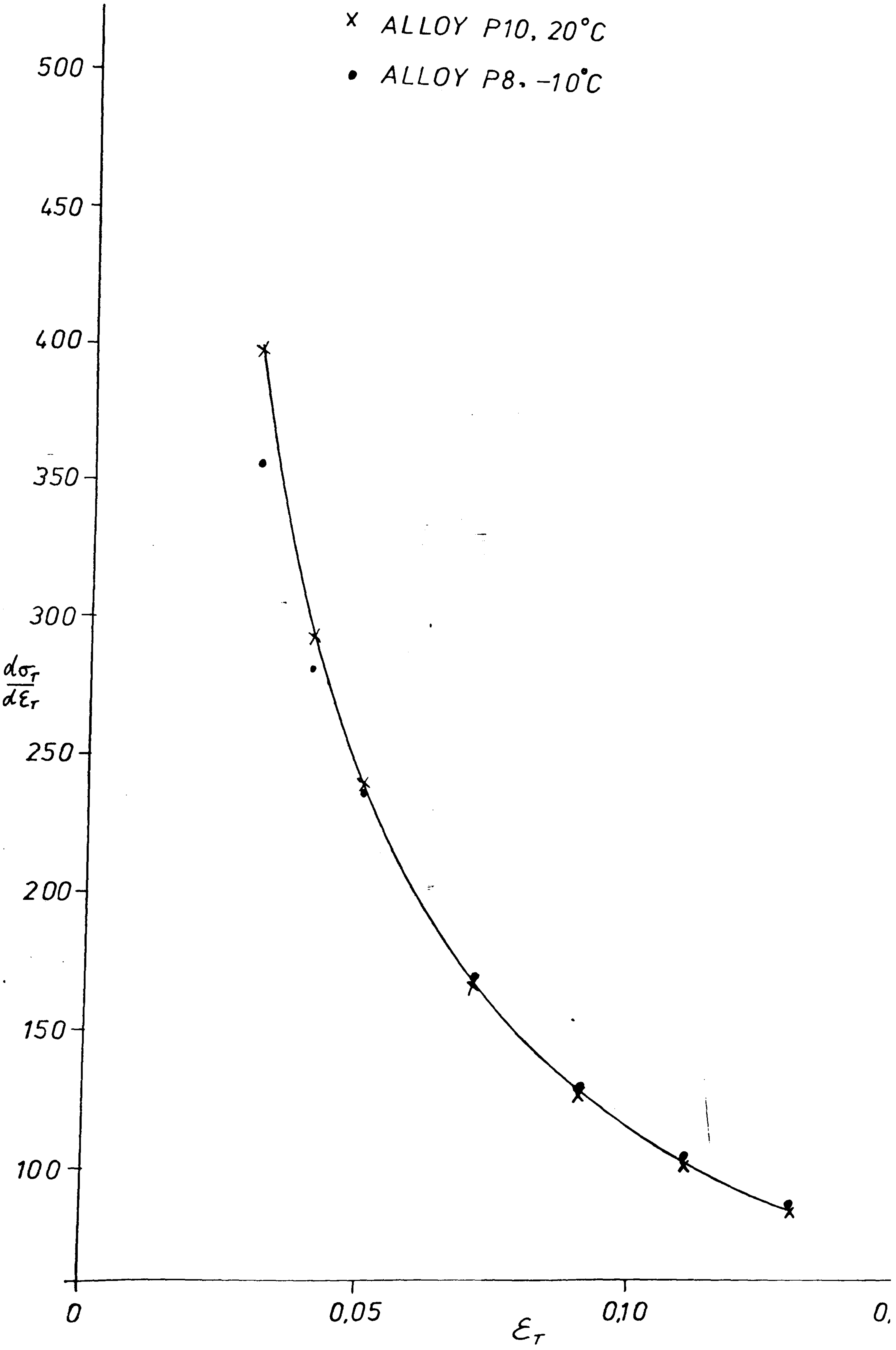
× ALLOY P10, 20°C
● ALLOY P8, -10°C
500
450
400
350
300
250
200
150
100
$\frac{d\sigma_T}{d\varepsilon_T}$
0
0,05
0,10
0,
ε_T

FIGURE 41

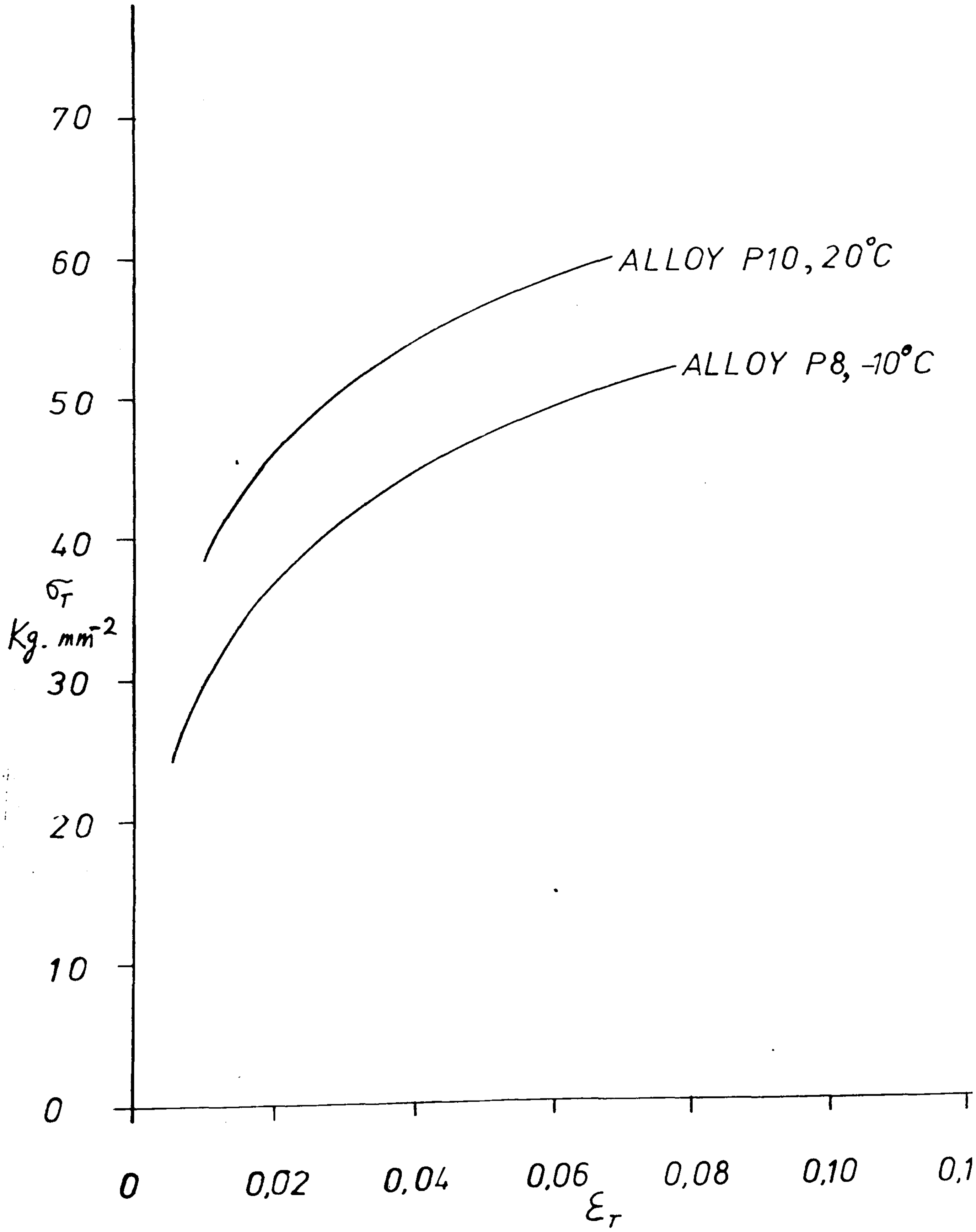
70
60
50
40
30
20
10
0
σ_T
Kg. mm^{-2}
0
0,02
0,04
0,06
0,08
0,10
ε_T
ALLOY P10, 20°C
ALLOY P8, -10°C

FIGURE 42

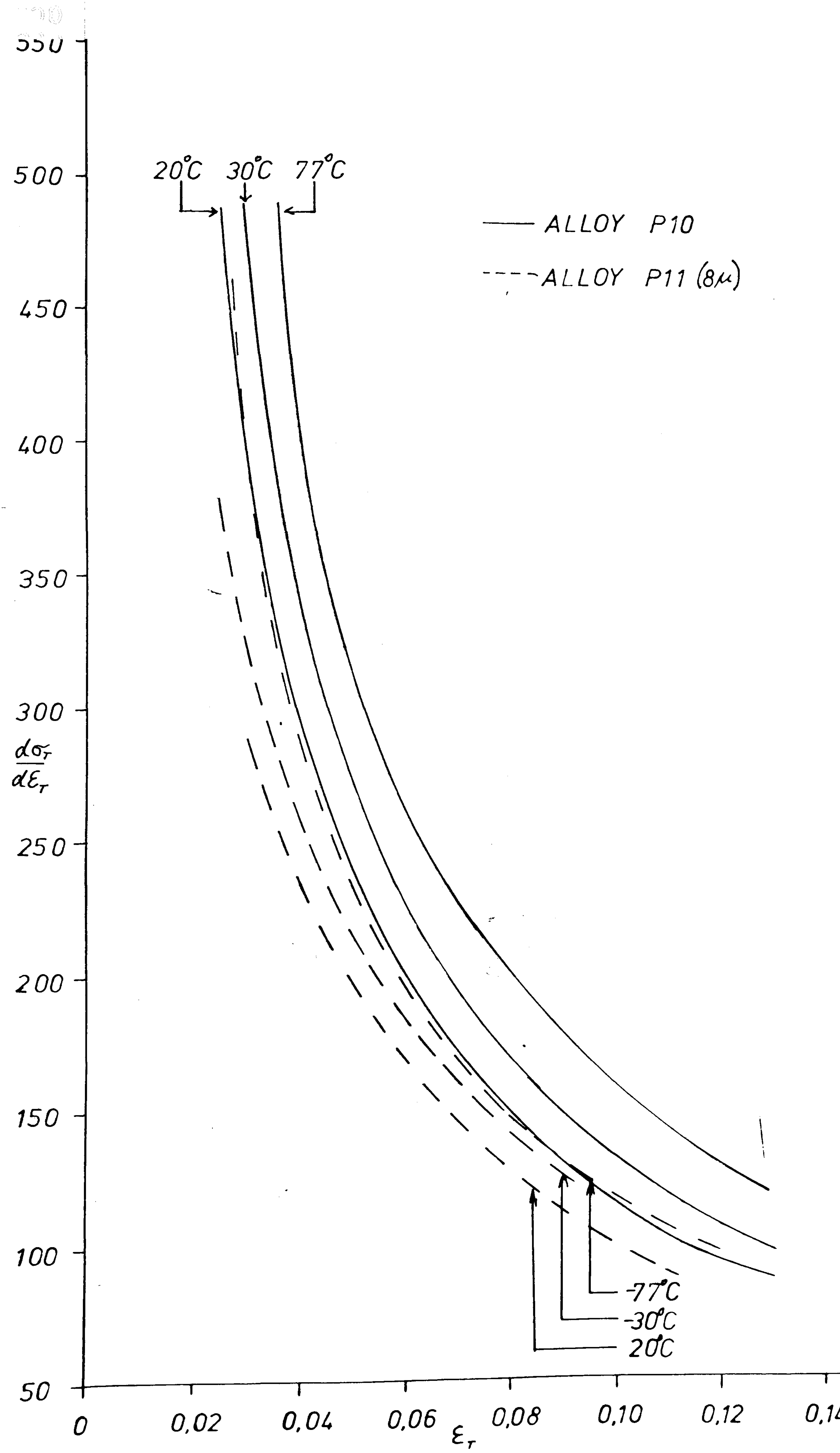

550
500
450
400
350
300
250
200
150
100
50
$\frac{d\sigma_T}{d\varepsilon_T}$
0
0,02
0,04
0,06
0,08
0,10
0,12
0,14
ε_T
20°C
30°C
77°C
ALLOY P10
ALLOY P11 (8μ)
-77°C
-30°C
20°C

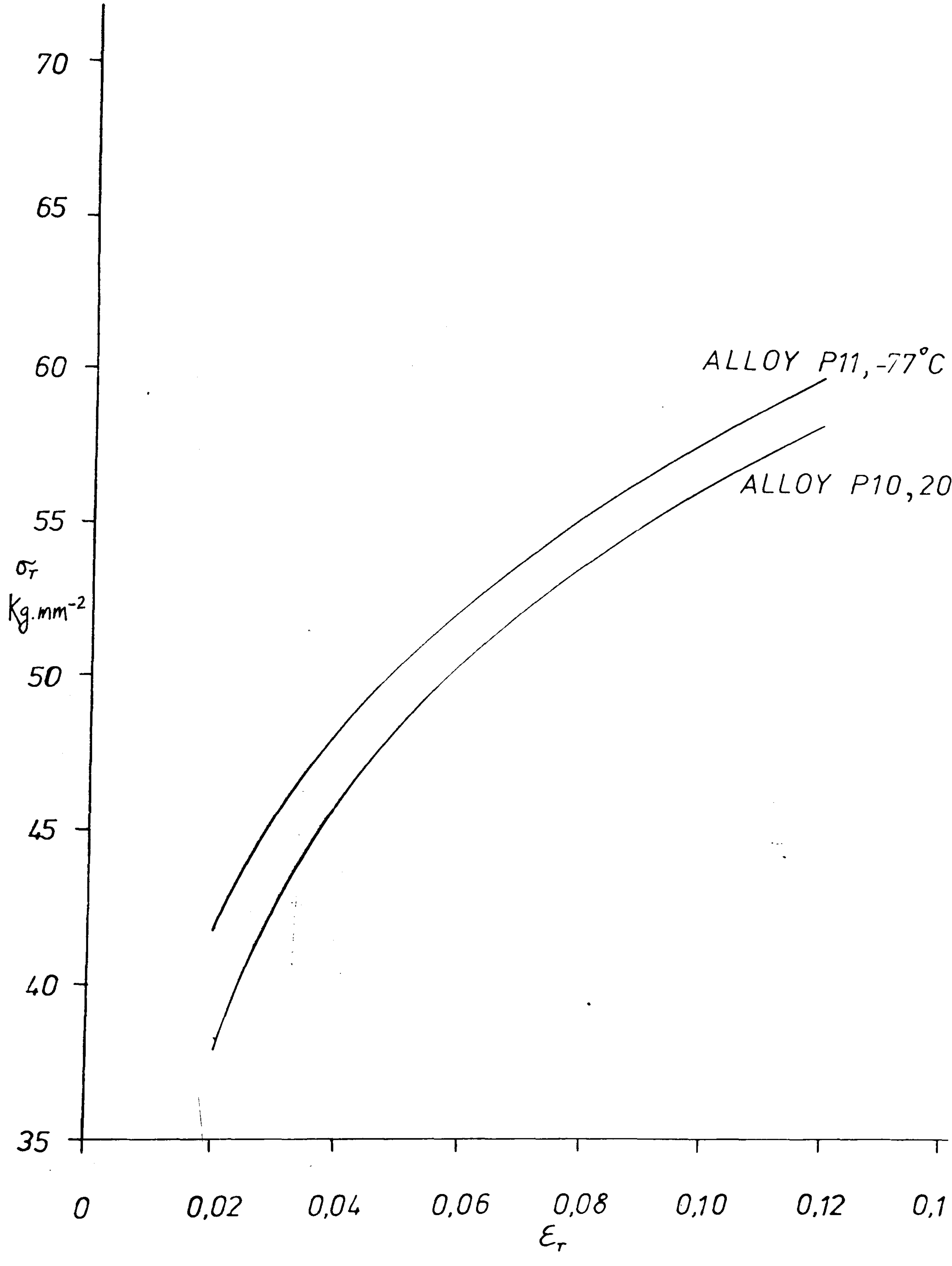
70
65
60
55
50
45
40
35
σ_T
Kg.mm^{-2}
ALLOY P11,-77°C
ALLOY P10,20
0
0,02
0,04
0,06
0,08
0,10
0,12
0,1
ε_T

FIGURE 44.

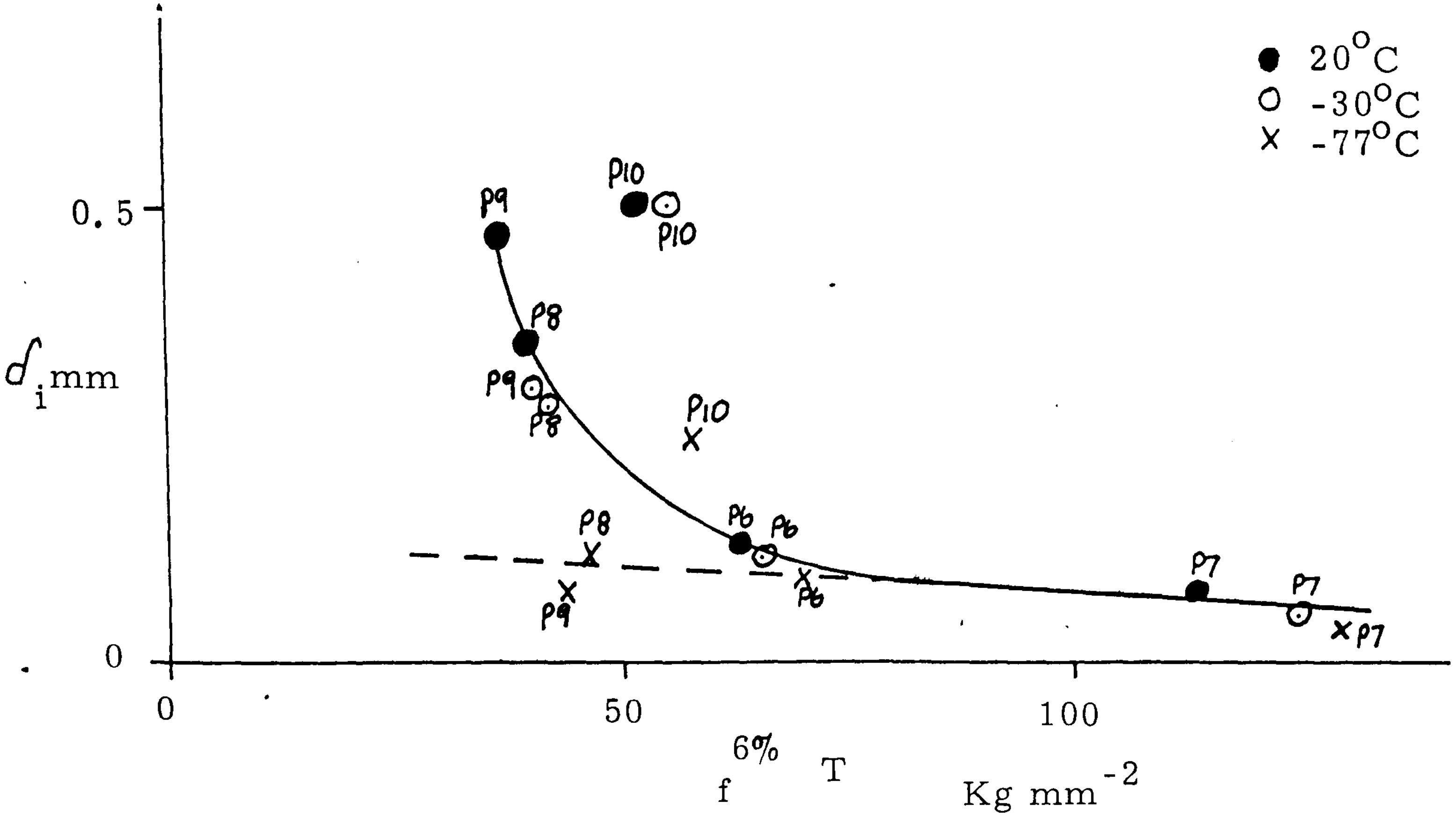

FIGURE 45: VARIATION OF FLOW STRESS ($\sigma_f^{6\%}\varepsilon_T$) WITH CRITICAL C.O.D. (δ_i)

ACKNOWLEDGEMENTS

The author would like to express his gratitude to the Science Research Council for providing financial support, and the Department of Metallurgy of the University of Strathclyde for providing the facilities for this research.

He would also like to thank his supervisor, Dr. R. Kennedy, Professor P. Grieveson and Dr. W. Roberts for their help and encouragement.